Impact of recent climate variability on oceanic CO_2 uptake in a global ocean biogeochemistry model

MASTER THESIS

to obtain the Master of Science degree in
Climate Physics: Meteorology and Physical Oceanography

Faculty of Mathematics and Natural Sciences
Kiel University Christian-Albrechts-Universität

submitted by
Frauke Bunsen
Matriculation Number: 1010626

August 3, 2021

Supervisor:
Dr. Judith Hauck,
Alfred Wegener Institute Helmholtz Centre for Polar and Marine Research

Second assessor:
Prof. Dr. Andreas Oschlies,
GEOMAR Helmholtz Centre for Ocean Research Kiel

Mentor:
Dr. Cara Nissen,
Alfred Wegener Institute Helmholtz Centre for Polar and Marine Research

Abstract

While atmospheric CO_2 concentrations have been increasing during recent decades due to anthropogenic emissions, the ocean has acted as a sink for atmospheric carbon. Essentially, the global air-sea flux of CO_2 showed a trend towards more oceanic uptake as expected from increasing emissions. Yet, the oceanic CO_2 uptake also responded to climate change and fluctuated due to climate variability and variations in the growth rate of atmospheric CO_2. So far, the drivers of the variability in oceanic CO_2 uptake are not conclusively understood.

In this thesis, the global ocean biogeochemistry model FESOM-1.4-REcoM is used to quantify the effects of climate change and of the increasing atmospheric CO_2 concentration on the trend in the oceanic carbon uptake during the period 1958-2019 (62 years). Two approaches are applied: (1) Offline diagnostics based on a linear approximation relating the trends in the sea surface temperature, dissolved inorganic carbon, alkalinity, salinity plus freshwater fluxes, wind velocity and sea-ice concentration to the trend in the CO_2 flux and (2) a model experiment with the historical forcing fields compared to simulations in which certain forcing fields (e.g. winds and the atmospheric forcing fields that control the sea surface temperature) are replaced by a repeated year forcing in order to isolate their effects on the CO_2 flux.

In FESOM-1.4-REcoM, the ocean took up $1.85\,\mathrm{Pg\,C\,yr^{-1}}$ of atmospheric CO_2 on average during the simulated period. The ocean carbon sink increased with a trend of $23.8\,\mathrm{Tg\,C\,yr^{-1}\,per\,yr}$. In a simulation with rising atmospheric CO_2 concentrations but without climate change and variability, the trend in oceanic carbon uptake was 27% higher than that, suggesting that climate variability has substantially reduced the uptake over the simulated period. Of this, a trend towards more outgassing of $2.9\,\mathrm{Tg\,C\,yr^{-1}\,per\,yr}$ was driven by the change and variability in winds, which was particularly relevant in the polar and subpolar regions. Hereby, a comparison between the offline and online approach reveals that the effect of winds was dominated by wind-driven changes in the transport of natural carbon with the circulation. Global warming caused a trend towards more oceanic outgassing of $2.3\,\mathrm{Tg\,C\,yr^{-1}\,per\,yr}$, which mostly originated from the tropical and subtropical zone. The increasing sea surface temperature led to more outgassing due to the reduced solubility of CO_2. The offline estimate for the effect of warming on the trend in the CO_2 flux is much larger, which can be attributed to the neglect of compensating feedbacks. In particular, the simulated effect of global warming reveals that in response to the increasing temperature, the concentration of dissolved inorganic carbon in the mixed layer decreased, which attenuated the thermally-driven outgassing. Changes in all other variables were less important drivers of the trend in the CO_2 flux.

Zusammenfassung

Während die CO_2-Konzentration der Atmosphäre im Verlauf der letzten Jahrzehnte aufgrund von anthropogenen Emissionen anstieg, wirkte der Ozean als eine Senke für Kohlenstoff. Auf den ersten Blick stieg dabei die CO_2-Aufnahme des Ozeans mit zunehmenden Emissionen an. Allerdings reagierte die CO_2-Aufnahme des Ozeans auch auf Klimaveränderungen und -variabilität, sowie auf die Fluktuationen der Anstiegsrate von CO_2 in der Atmosphäre. Bisher sind die Ursachen für die Variabilität der ozeanischen CO_2-Aufnahme noch nicht endgültig verstanden.

In dieser Arbeit verwende ich das globale biogeochemische Ozeanmodell FESOM-1.4-REcoM, um die Auswirkungen des Klimawandels und des Anstiegs von CO_2 in der Atmosphäre auf den Anstieg der ozeanischen CO_2-Aufnahme im Zeitraum 1958-2019 (62 Jahre) zu quantifizieren. Zwei Methoden werden dazu verwendet: (1) Offline-Berechnungen, in denen mithilfe einer linearen Näherung den Trends von Temperatur, gelöstem anorganischem Kohlenstoff, Alkalinität, Salinität & Süßwassergehalt, Windgeschwindigkeit und Meereisdichte ein Trend des CO_2-Austauschs zwischen Atmosphäre und Ozean zugeordnet wird und (2) eine Simulation der historischen CO_2-Aufnahme, der ich weitere Simulationen gegenüber stelle, in denen jeweils ein Teil der atmosphärischen Antriebsfelder (zum Beispiel die Winde oder diejenigen Antriebsfelder, die direkten Einfluß auf die Oberflächentemperatur des Ozeans ausüben) durch sich jährlich wiederholende Antriebsfelder ersetzt wird, um dessen Einfluss auf die CO_2-Aufnahme zu bestimmen.

In FESOM-1.4-REcoM hat der Ozean im betrachteten Zeitraum durchschnittlich $1.85\,\mathrm{Pg\,C\,a^{-1}}$ CO_2 aufgenommen. Die CO_2-Aufnahme ist dabei mit einem Trend von $23.8\,\mathrm{Tg\,C\,a^{-1}}$ pro Jahr angestiegen. In einer Simulation mit ausschließlich einem Anstieg von CO_2 in der Atmosphäre und ohne Klimaveränderungen ist dieser Trend um 27% größer, was bedeutet, dass Klimaveränderungen die CO_2-Aufnahme des Ozeans im betrachteten Zeitraum beträchtlich reduziert haben. Davon ist ein Trend von $2.9\,\mathrm{Tg\,C\,a^{-1}}$ pro Jahr in Richtung weniger CO_2-Aufnahme dem Einfluss der Winde zuzuordnen. Dieser war besonders in polaren und subpolaren Gebieten relevant. Ein Vergleich der Offline-Abschätzung und der Online-Berechnung zeigt dabei, dass dieser Effekt vor allem eine Folge von windangetriebenen Strömungsveränderungen und damit eines veränderten Transports von natürlichem Kohlenstoff im Ozean war. Auch die globale Erwärmung verursachte einen Trend von $2.3\,\mathrm{Tg\,C\,a^{-1}}$ pro Jahr in Richtung weniger ozeanischer CO_2-Aufnahme. Vor allem die tropischen und subtropischen Zonen haben zu diesem Trend beigetragen. Wegen der geringeren Löslichkeit von CO_2 in wärmerem Wasser verursachte die steigende Wassertemperatur ein verstärktes Ausgasen von CO_2 aus dem Ozean. Die Offline-Abschätzung des Temperatur-Effekts ergibt einen wesentlich höheren Wert, weil in ihr kompensierende Feedbackmechanismen nicht berücksichtigt sind. Insbesondere zeigen die Simulationen mit und ohne Erwärmung, dass als Folge der höheren Temperatur auch der Gehalt an gelöstem CO_2 in der Oberflächenschicht abnahm, was zu einer Abmilderung des ursprünglichen Temperatureffekts führte. Veränderungen in allen anderen Variablen hatten einen vergleichsweise geringeren Einfluss auf den Trend des CO_2-Flusses.

Contents

Chapter 1

Introduction

Over the past century, the Earth has experienced a warming climate. Anthropogenic CO_2 emissions are responsible for 80% of the radiative forcing driving the warming since 1750 (IPCC, 2013c). By 2020, the annual emissions of CO_2 have gone up to $11.2\,\mathrm{Pg\,C\,yr^{-1}}$ (Friedlingstein et al., 2020) and in April 2021, the atmospheric CO_2 concentrations have passed 420 ppm for the first time since the beginning of the records in 1958 (NOAA, 2021b). The increased atmospheric CO_2 concentrations have driven an increased flux of CO_2 into the ocean (Wanninkhof et al., 2013) and the ocean has absorbed approximately 25% of the cumulative CO_2 emissions since 1850 (Friedlingstein et al., 2020). However, the fraction of anthropogenic carbon that is removed from the atmosphere by the ocean varies. Observation-based data products show a decadal variability in the atmospheric CO_2 growth rate which is not driven by anthropogenic CO_2 emissions (Le Quéré et al., 2009). For instance, the increase in atmospheric CO_2 concentrations during the 1990s was more than could have been expected from anthropogenic emissions alone, whereas in the 2000s, it was less than could have been expected from the emissions (DeVries et al., 2019). The oceanic carbon sink could be responsible for up to 40% of this decadal variability in the atmospheric CO_2 growth rate (DeVries et al., 2019). Yet, drivers of the variability in oceanic CO_2 uptake are still not conclusively understood (Landschützer et al., 2015; DeVries et al., 2017; McKinley et al., 2020).

The natural and anthropogenic carbon cycle The air-sea carbon flux can be thought of as having a **natural** and an **anthropogenic** component. Only the sum of both is real, but the net CO_2 flux can be understood easier through the notional distinction of the natural and anthropogenic component, which might be even in the opposite direction (Figure 1.1). The sum of both is called **historical** when referring to past times, and **contemporary** or simply the **total** CO_2 flux when referring to the present time. The natural component is the part of the total CO_2 flux that would occur at preindustrial atmospheric CO_2 concentrations. The natural CO_2 flux is zero when globally integrated, apart from a steady outgassing of carbon brought into the ocean by rivers (Hauck et al., 2020). This reflects that the natural carbon reservoirs of atmosphere and ocean are assumed to be in equilibrium at preindustrial conditions. Regionally, however, the natural carbon flux can be either negative or positive and high in magnitude. Natural CO_2 in the ocean increases with depth due to biological processes (Sarmiento and Gruber, 2006). The anthropogenic component is the part of the total CO_2 flux which is caused by the rising atmospheric CO_2 concentrations. Therefore, the anthropogenic CO_2 flux is directed into the ocean almost everywhere. Compared to the natural CO_2 flux, the anthropogenic CO_2 flux is generally smaller in magnitude and regionally more uniform. The signal of anthropogenic carbon decreases with depth because it was recently added at the ocean surface and the transport into the deep ocean by the circulation proceeds slowly. About one third of the anthropogenic carbon storage is found in the upper 200m of the ocean and nearly half is found in the upper 400m (Sabine et al., 2004). The regional variability of the historical CO_2 flux is dominated

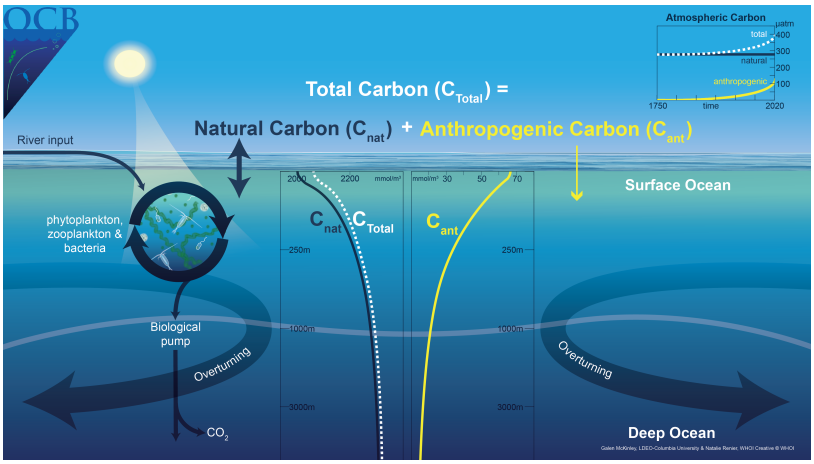

Figure 1.1: The natural and the anthropogenic carbon cycle. Credit: Graphic design by Natalie Renier (Woods Hole Oceanographic Institution) and concept by Galen McKinley (Columbia Univ., Lamont-Doherty Earth Observatory). Accessed on 04.07.2021 at https://galenmckinley.github.io/new%20ocb%20graphic%20on%20ocean%20carbon%20cycle/OCBgraphic/

by the natural CO_2 flux. It is also the natural CO_2 flux that is most affected by variability and trends in climate (Wanninkhof et al., 2013). In contrast, the flux of anthropogenic carbon is mostly affected by the increase of atmospheric CO_2 (Wanninkhof et al., 2013).

Processes that affect the air-sea CO_2 flux Apart from the increase in the atmospheric CO_2 concentration, processes that modify the air-sea flux of CO_2 are the variability in wind velocity, sea-ice, sea surface temperature, dissolved inorganic carbon (DIC), salinity and alkalinity. In a simplified scheme (see Sarmiento and Gruber, 2006, Chap. 3.3), the flux (F_{surf}) of CO_2 at the ocean surface can be calculated from the solubility of CO_2 (α), the gas transfer velocity (k_w) and the difference in partial pressure of CO_2 between the atmosphere and the ocean as:

$$F_{\text{surf}} = \alpha \cdot k_w \left(\text{pCO}_2^{\text{A}} - \text{pCO}_2^{\text{O}} \right) \tag{1.1}$$

The gas exchange coefficient ($\alpha \cdot k_w$) is controlled by the sea surface temperature through the solubility of CO_2 on the one hand. On the other hand, it is controlled by the wind velocity and sea-ice through the factor k_w. The partial pressure pCO_2^{O} is sensitive to changes in DIC, salinity and alkalinity. Consequently, the air-sea flux of CO_2 responds to changes in the latter driven by the ocean circulation or biological production. Additionally, the air-sea flux of CO_2 is sensitive to changes in the ocean's buffer capacity for carbon (Lovenduski et al., 2007). The buffer capacity of the ocean describes the ocean's capacity to take up more carbon than expected from the solubility of CO_2 in water through chemical reactions which reduce the concentration of dissolved CO_2 (Sarmiento and Gruber, 2006, Chap. 8.3).

In a changing climate, some of these processes are competing. In some cases, climate variability has opposing effects on the air-sea flux of natural and anthropogenic carbon. Processes which favor the gas exchange ($\alpha \cdot k_w$) between air and ocean, such as a retreat of sea-ice cover or a roughening of the sea surface by winds, generally lead to more oceanic uptake of anthropogenic carbon. However, depending on the local direction of the natural CO_2 flux, these processes might fortify either outgassing or uptake of natural carbon.

Furthermore, changes in the ocean circulation may provoke competing effects on the flux of natural and anthropogenic carbon. In the case of a strengthening overturning circulation, the removal of anthropogenic carbon from the surface ocean into the deep becomes more effective, leading to an

enhanced uptake of anthropogenic CO_2 on the one hand. On the other hand, increased upwelling of CO_2 rich deep waters in a strengthened overturning can generate more outgassing of natural carbon. Then again, the shorter residence time of waters at the surface in an accelerated overturning counteracts both the uptake of anthropogenic carbon and the outgassing of natural carbon (Wanninkhof et al., 2013).

The warming of seawater and changes in the ocean's buffer capacity both attenuate the increase in the historical rate of carbon uptake. Through the warming, the solubility of CO_2 in the surface ocean decreases and pCO_2^O increases, which reduces the flux of carbon from the atmosphere into the ocean (Le Quéré et al., 2010). The buffer capacity of the ocean decreases as more carbon dissolves in seawater, meaning that the ocean shifts towards less carbon uptake for the same increase in atmospheric CO_2 partial pressure (Fassbender et al., 2017).

The air-sea exchange of CO_2 is largely controlled by the difference of the CO_2 partial pressures between ocean and atmosphere, as the partial pressure of CO_2 at the ocean surface (pCO_2^O) and in the atmosphere (pCO_2^A) seek to be in balance. However, compared to the atmospheric pCO_2 which is rather homogeneously distributed globally, pCO_2^O shows much higher regional variability (Sarmiento and Gruber, 2006, Chap. 8.1; Rödenbeck et al., 2015). This generates a high regional variability in the air-sea CO_2 flux. Furthermore, pCO_2^O is affected by external climate forcing such as volcanic eruptions (McKinley et al., 2020) and internal climate variability. In fact, the oceanic pCO_2^O regionally undergoes temporal changes at frequencies that match those from the major climatic modes (i.e. the Atlantic Multidecadal Oscillation, Pacific Decadal Oscillation, El Niño Southern Oscillation and the Southern Annular Mode). In concert with the climatic modes, Landschützer et al. (2019) found that pCO_2^O varies at frequencies in the order of a decade or longer, while the dominant frequencies are still subject of debate (Rödenbeck et al., 2015). The variability in pCO_2^O generates temporal variability in the regional air-sea CO_2 flux on similarly long time scales. Observational time series mostly do not start earlier than in the 1990's, so that only one or two oscillations of such climate modes are part of the records. Thus, it is unlikely that the effect of internal climate variability on the air-sea CO_2 flux can be distinguished from the impact of anthropogenic climate change in observational data at the moment. Secular trends in the rate of oceanic carbon uptake driven by climate change are expected to emerge within the next decades (McKinley et al., 2016).

The impact of climate change on the ocean carbon sink Overall, climate change is expected to reduce the capacity of the ocean to act as a sink for atmospheric CO_2, producing a feedback that accelerates the accumulation of CO_2 in the atmosphere and enhances climate change (Fung et al., 2005). Le Quéré et al. (2010) found that between 1981-2007, climate variability and trends had offset 63% ($-20\,\mathrm{Tg\,C\,yr^{-1}}$ per year) of the trend in the CO_2 flux towards more oceanic uptake that was expected from the increase of atmospheric CO_2 ($+32\,\mathrm{Tg\,C\,yr^{-1}}$ per year). Thereby, the cumulative oceanic carbon uptake in this period was reduced by 12% according to Le Quéré et al. (2010). The largest climate-induced impact on the trend in CO_2 flux was caused by changes in the wind-driven circulation affecting the natural carbon cycle ($-12\,\mathrm{Tg\,C\,yr^{-1}}$ per year). A further contribution stemmed from an increased oceanic outgassing of CO_2 due to the decreasing solubility of CO_2 in response to a warmer sea surface temperature ($-4\,\mathrm{Tg\,C\,yr^{-1}}$ per year). The estimate of Le Quéré et al. (2010) goes back to a series of model simulations with an Ocean General Circulation Model coupled to a marine biogeochemistry model.

There is considerable regional variability in the trend in the CO_2 flux and its response to climate variability (Le Quéré et al., 2010; Fung et al., 2005; Gruber et al., 2019; DeVries et al., 2017). Le Quéré et al. (2010) state that the impact of climate on the decadal CO_2 flux trend is largest in the equatorial Pacific and in the Southern Ocean, whereas Landschützer et al. (2016) found that most of the decadal climate-induced trend in CO_2 flux stems from the extratropical latitudes in both hemispheres. Multiple regional studies have focused on local climate variability driving the decadal variability in the CO_2 flux, particularly in the Southern Ocean (e.g. Hauck et al., 2013a;

Landschützer et al., 2015; Lovenduski et al., 2007) and in the North Atlantic (e.g. Levèvre et al., 2004; Völker et al., 2002; Macovei et al., 2020). Because there is a considerable spread between different models concerning the regional trends in the CO_2 flux (Hauck et al., 2020) and because the regional trends in the CO_2 flux in model studies are sensitive to the dataset used to force the model (Le Quéré et al., 2010), it is likely that further model studies will have a different outcome compared to the estimate of Le Quéré et al. (2010).

Aim of this thesis The aim of this thesis is to quantify the impact of climate change and the effect of increasing atmospheric CO_2 concentrations on the trend in the oceanic carbon uptake in a global ocean biogeochemistry model. Additionally, the effects of different climate processes on the CO_2 flux will be separated. The model FESOM-REcoM is used to simulate the time period 1958 to 2019, thereby also extending the analysis of Le Quéré et al. (2010) by 36 years. This time period allows the detection of secular trends which are still difficult to derive from observations. Moreover, the model is targeted at quantifying the global effect that is hard to extrapolate from measurements, as observations currently cover only a small area of the regionally variable field of CO_2 fluxes.

Chapter 2

Ocean biogeochemical model and setup

In this thesis, the Finite Element Ocean Model 1.4 (FESOM 1.4) coupled with the Regulated Ecosystem Model 2 (REcoM 2) is used (Wang et al., 2014; Hauck et al., 2013b; Schourup-Kristensen et al., 2014, 2018). FESOM is a global ocean and sea-ice model with a regionally varying resolution between 10-230 km Figure 2.1. The resolution is coarse in the subtropical open ocean between 10 and 40 °N/S and is refined at high latitudes in particular in the northern hemisphere to capture dynamics under a high Coriolis parameter. Near the equator, the resolution is also high to allow for the narrow equatorial current system and equatorial waves. In the upper ocean, the model has a vertical resolution of about 10m. The output is written as monthly fields. FESOM 1.4 is described in detail in Wang et al. (2014). REcoM is a biogeochemical model coupled to FESOM, which simulates the oceanic cycle of carbon, including calciumcarbonate, oxygen and the nutrients nitrogen, silicon and iron. The carbonate chemistry and ocean-air flux are calculated with mocsy 2.0 (Orr and Epitalon, 2015) following the protocol of the Ocean Carbon Model Intercomparison Project (Orr et al., 2017). In REcoM, organic carbon cycles between the model compartments of two phytoplankton and one zooplankton functional types, as well as detritus and dissolved organic carbon. A documentation of REcoM is available online (https://recom.readthedocs.io/, Gürses (2021)) and the model equations are published in the supplements of Hauck et al. (2013a). An evaluation of the surface fields of net primary production, chlorophyll and nutrients in REcoM has been done by Schourup-Kristensen et al. (2014), revealing reasonable agreement with observations. Hauck et al. (2020) did an evaluation of the oceanic carbon uptake in FESOM-REcoM, comparing it to observation-based products,

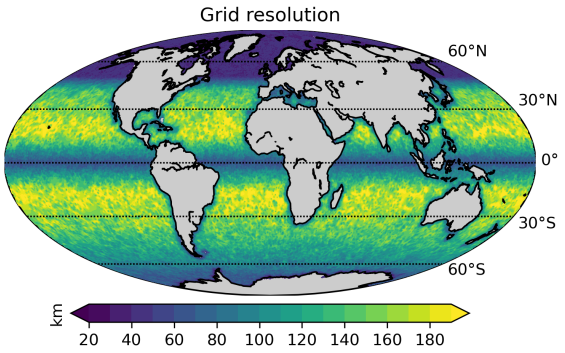

Figure 2.1: The grid resolution of FESOM-REcoM

Table 2.1: Overview of model simulations

		A	B	C	D	E	F
atmospheric CO_2		×	-	×	-	×	×
climate	temperature					-	×
	winds	×	-	-	×	×	-
	other					×	×

×: varying, -: constant

to other global ocean biogeochemical models and to surface ocean pCO_2 observations (Bakker et al., 2016). They state that all models which they compared, including FESOM-REcoM, are well-suited to quantify the global mean oceanic carbon uptake on yearly timescales and also produce results for the trend which correlate well among each other. Accordingly, the global mean oceanic carbon uptake in FESOM-REcoM falls within the range of other models with a positive bias (i.e. a global uptake of natural carbon of $0.19\,\mathrm{Pg\,C\,/yr}$ at climatological forcing) and drift ($2.6\,\mathrm{Tg\,C\,yr^{-2}}$). The previously evaluated model will be used in here to investigate the carbon flux in further simulations.

The simulations are initialized with alkalinity and preindustrial dissolved inorganic carbon from GLODAPv2 (Lauvset et al., 2016) and nutrients from WOA2013 (Garcia et al., 2013). Biomass fields are initialized from low concentrations. The model was spun up from rest from 1850 to 1957, repeating the atmospheric forcing for the year 1961 and using either constant (278 ppm) or globally uniform historical atmospheric CO_2 levels averaged from Mauna Loa and South Pole stations (Friedlingstein et al., 2020). For simplicity, we refer to the annually repeated forcing of the year 1961 as "constant" forcing despite that it contains seasonal and regional variability. The atmospheric forcing for the simulations from 1958-2019 stems from the extended Japanese 55-year Reanalysis (JRA-55) Version 1.4.0 (Tsujino et al., 2018). The atmospheric climate forcing includes 3-hourly winds, air temperature, downward longwave and shortwave radiation, humidity, precipitation and sea level pressure. Climatological river runoff is taken from the CORE data set Large and Yeager (2009).

In this thesis, data from six simulations are used which are summarized in Table 2.1, which allows for a detailed disentanglement of the impact of climate variability and rising atmospheric CO_2 levels on the air-sea CO_2 exchange.

Four of the simulations address the general effect of climate change and variability on the carbon flux and two simulations address the specific effects of wind and temperature. The four main simulations cover all combinations of constant or variable forcing for atmospheric CO_2 concentrations on the one hand, and constant or variable forcing for atmospheric climate on the other hand. In simulations A and C (sim-A, sim-C), atmospheric CO_2 increases as in historical records, whereas in simulations B and D (sim-B, sim-D), atmospheric CO_2 is kept constant at preindustrial concentrations of 278 ppm (Table 2.1). In sim-A and sim-D, climate changes as in historical records, whereas in sim-B and sim-C, climate is kept constant using repeated forcing of the year 1961. These four simulations constitute the FESOM-REcoM contribution to the "Regional Carbon Cycle Assessment and Processes 2" (RECCAP2, Hauck et al. (2021)) project.

In order to separate the effects of winds and temperature, I conducted two additional simulations (sim-E and sim-F). In sim-F, winds are kept constant using repeated year forcing while all other forcings are variable. In sim-E, global warming is removed using a repeated year forcing for air temperature, longwave and shortwave radiation and humidity.

Chapter 3

Methods for the assessment of the model output

The air-sea flux of CO_2 is analyzed with respect to the mean flux, spatial and temporal variability and the multi-decadal trend [1] using the simulations described in Chapter 2. The methods to disentangle the impact of a suite of variables on the trend in the CO_2 flux are described in the following section. These variables are: The increase in atmospheric pCO_2 and the overall effect of climate variability; furthermore, the effect of climate variability is broken down into change and variability in winds, temperature, sea-ice concentration, dissolved inorganic carbon (DIC), alkalinity, salinity and freshwater fluxes, biology and circulation. In order to separate their effects, two approaches are used: One approach is to simulate the effect of these variables in a series of model simulations, in which the forcing for individual variables is held constant (see Chapter 2). A second approach is to approximate the effect of each variable following the offline calculations of Lovenduski et al. (2007) based on a single model simulation. In the following, I provide details on both methods.

3.1 Disentangling the drivers of CO_2 flux trends with a series of model simulations

The impact of some variables affecting the trend in the CO_2 flux are disentangled by doing a series of model simulations (as described in Chapter 2), in which some variables of the forcing are held constant. Thereby, one can separate the following effects: The atmospheric CO_2 concentration ($atmCO_2$), the combined effect of all climate variability (clim), and also winds (winds) and sea surface temperature (temp) separately. Climate, winds and temperature can be thought of as causing separate trends in the natural CO_2 flux (nat) on the one hand and in the anthropogenic CO_2 flux (ant) on the other hand. Additionally, the effect of model drift (drift), i.e. an artificial trend in the natural carbon flux at the notional absence of any climate variability, arises.

The model drift is known from sim-B, in which all forcing fields are held constant:

$$B = [\text{drift}] \tag{3.1}$$

Here, B refers to the trend in the variable of interest, which is the CO_2 flux (F_{surf}), in sim-B. In the following, A, B, C, D, E and F are used to refer to the trend in the CO_2 flux ($\beta(F_{\text{surf}})$) in each of the simulations. Analogously, the equations apply on all timescales, e.g. on the temporal mean CO_2 flux and cumulative CO_2 flux in each of the simulations.

[1] Trends are determined by applying a least square linear fit to annual mean data. The significance of trends is tested for the null hypothesis that the trend is zero, using a Wald Test with a t-distribution of the test statistic. Significance is accepted for p-values ≤ 0.05.

The historical simulation (sim-A), in which all forcing fields change over time and in which the CO_2 flux increases over time is the reference (ref). We here define a **positive** flux to be **directed from the atmosphere into the ocean**. The trend in the CO_2 flux in sim-A can be thought of as the sum of the following components:

$$A = [\text{drift}] + [\text{atm}CO_2] + [\text{clim}, \text{nat}] + [\text{clim}, \text{ant}] \tag{3.2}$$

If a part of the forcing is held constant, the effect of this variable on the trend in the CO_2 flux is absent in the respective simulation. This absence is attributed to the constant part of the forcing. In sim-C, the trend in the CO_2 flux that results from climate variability is absent:

$$C = [\text{drift}] + [\text{atm}CO_2] \tag{3.3}$$

Thus, sim-C is used to calculate the impact of increasing atmospheric CO_2 concentrations on the trend in the CO_2 flux in the absence of climate variability:

$$[\text{atm}CO_2] = C - B \tag{3.4}$$

Furthermore, sim-C is used to calculate the impact of climate variability on the trend in the historical CO_2 flux, i.e. the sum of the natural and anthropogenic component:

$$[\text{clim}, \text{nat}] + [\text{clim}, \text{ant}] = A - C \tag{3.5}$$

Assuming that the drift is the same in all simulations, subtracting the trend in any simulation from another automatically corrects for the model drift.
In sim-D, the climate is variable but the CO_2 flux that results from increasing atmospheric CO_2, i.e. the anthropogenic component, is absent:

$$D = [\text{drift}] + [\text{clim}, \text{nat}] \tag{3.6}$$

Thus, sim-D is used to calculate the impact of climate variability on the trend in the natural CO_2 flux:

$$[\text{clim}, \text{nat}] = D - B \tag{3.7}$$

Consequently (Equations (3.5) and (3.7)), the impact of climate variability on the anthropogenic flux can be separated as:

$$[\text{clim}, \text{ant}] = (A - C) - (D - B) \tag{3.8}$$

Furthermore, the effect of climate variability on the trend in the historical CO_2 flux, which has been calculated from Equation (3.5), is separated into winds, temperature and other climate variability. Here, only the effect on the total CO_2 flux is simulated and the natural and anthropogenic parts are not separated. When winds and temperature vary simultaneously, a nonlinear effect (nonl) arises, so that the sum of the individual effects of constant drivers is not equal to the full effect.

$$[\text{clim}, \text{nat} + \text{ant}] = [\text{temp}] + [\text{winds}] + [\text{other}] + [\text{nonl}] \tag{3.9}$$

For this purpose, the series of simulations is extended with two more simulations, sim-E and sim-F. In sim-F, the variability of winds is absent:

$$F = [\text{drift}] + [\text{atm}CO_2] + [\text{temp}] + [\text{other}] \tag{3.10}$$

Here, we ask: What was the effect of the variability in winds on the historical CO_2 flux (sim-A)? This is calculated by the difference between the historical simulation (sim-A) and a simulation which is set up almost identical, i.e. with all forcing fields varying, but not the winds. Thus, the

answer includes a nonlinear effect which was provoked by the variability of winds interfering with an otherwise variable climate. Therefore, the impact of variability in winds is defined as (A-F):

$$[\text{winds}] + [\text{nonl}] = A - F \tag{3.11}$$

The atmospheric forcing for sim-E is configured to preferably remove the signal of atmospheric warming from the sea surface temperature, while still allowing other climate variables, namely winds, pressure at sea level and freshwater fluxes from rainfall and snowfall to vary with time.

$$E = [\text{drift}] + [\text{atm}CO_2] + [\text{winds}] + [\text{other}] \tag{3.12}$$

Again, we ask: What was the effect of variability in the sea surface temperature on the historical CO_2 flux (sim-A) compared to the same simulation but without anthropogenic warming (sim-E)? Thus, the temperature effect on the trend in the CO_2 flux is defined as (A-E):

$$[\text{temp}] + [\text{nonl}] = A - E \tag{3.13}$$

The forcing variables which are responsible for the global warming of sea surface temperature ($\beta(T)$) are the rising air temperatures (airT), variability in longwave radition due to the greenhouse effect together with variability in shortwave radiation (lw+sw) and the increase of specific humidity (hum) near the water surface, which controls latent heat flux (Deser et al., 2010). Preliminary simulations which I performed showed that the rising air temperatures account for 41% of the warming trend in the global mean sea surface temperature, longwave and shortwave radiation account for 16% and humidity near the water surface for 44%. All of these are set constant in sim-E to remove the warming signal:

$$[\text{airT}] + [\text{lw} + \text{sw}] + [\text{hum}] = \text{constant} \tag{3.14}$$

The remaining variability and any local or global trends in the sea surface temperature in sim-E are due to changes in stratification and ocean circulation as a result of the variability in the other atmospheric variables. As shown in Figure 4.21a, the warming trend of the global mean temperature is removed in sim-E.

Finally, the part of the trend in the historical CO_2 flux caused by the full climate variability that cannot be explained by the sum of the wind and temperature effects is attributed to the other climatic forcing variables and the nonlinear effect (Equations (3.9), (3.11) and (3.13)):

$$[\text{other}] - [\text{nonl}] = (A - C) - (A - E) - (A - F) \tag{3.15}$$

Because the nonlinear effects in Equations (3.9), (3.11) and (3.13) and Equation (3.15) are not necessarily the same, the separation into the effects of the other variables and the nonlinear effect remains unknown. However, we assumed that winds and temperature would account for most of the variability.

3.2 Disentangling the drivers of CO_2 flux trends with an offline calculation

Following Lovenduski et al. (2007), I approximate the direct effects of some variables on the CO_2 flux analytically. These variables are: Wind velocity, sea-ice concentration, DIC, alkalinity, salinity and freshwater fluxes, biology and circulation. The calculations are done using output from sim-D and sim-A. Sim-D, which is forced with pre-industrial atmospheric CO_2 concentrations but historical climate variability, allows us to calculate the impact of climate change and variability on the natural carbon cycle. Strictly speaking, the trend in sim-D additionally contains the model drift.

However, correcting for the drift using a simple subtraction as in Equation (3.7) has caveats (Evans and Argüeso, 2014). Firstly, the assumption that the model drift is the same in sim-D and in all other simulations is not certain. Secondly, the drift-induced variability in the drivers of the trend in the CO_2 flux coupled with climate-induced variability can generate non-additive effects. Further, a subtraction of sim-B from sim-D would make the corrected model output field dynamically inconsistent with its drivers. This is why the calculations in this part are restrained to sim-D without applying a drift correction.

Because ~98% of the surface ocean's historical carbon content is natural carbon (Sarmiento and Gruber, 2002), the impact of climate variability on the natural and the historical carbon cycle is often assumed to be similar. However, this assumption is not without caveats (Lovenduski et al., 2007). That's why additionally, sim-A is used to calculate the impact of most climate variables on the historical air-sea carbon flux. Yet, this can not be done for DIC (see Section 3.2.4).

The analytic approximations are based on the model equation for the CO_2 flux (F_{surf}), which is calculated following the protocol of Orr et al. (2017) as:

$$F_{\text{surf}} = \alpha k_w \cdot \Delta\text{pCO}_2 \tag{3.16}$$

where ΔpCO_2 is the difference of atmospheric and oceanic partial pressures ($\text{pCO}_2^{\text{A}} - \text{pCO}_2^{\text{O}}$); k_w is the gas transfer velocity (piston velocity), which depends on wind speed and sea-ice concentration (Equation (3.18)); and α is the solubility of CO_2 in seawater, which depends on temperature and salinity (Equation (3.26)). Further, the partial pressure of CO_2 in water (pCO_2^{O}) is sensitive to dissolved inorganic carbon (DIC), alkalinity (Alk), temperature and salinity (Sarmiento and Gruber, 2006, Chapter 8.3).

Following Lovenduski et al. (2007), the contribution of each variable X_i to the trend (β) in the CO_2 flux is approximated. Conceptually, the method of Lovenduski et al. (2007) can be used to estimate the impact of changes in the variables on the CO_2 flux on any time scale. Originally, Lovenduski et al. (2007) have used the approach to approximate the difference in the CO_2 flux between a positive phase of the Southern Annular Mode and the mean state. In this thesis, the focus is in on the secular trend between 1958 and 2019. The trend in the CO_2 flux ($\beta(F_{\text{surf}})$) is approximated by calculating the trend in the respective variable $\beta(X_i)$ and the sensitivity of the CO_2 flux to changes in that variable:

$$\beta(F_{\text{surf}}) \approx \sum_i \left[\frac{\partial F_{\text{surf}}}{\partial X_i}\right] \beta(X_i) \tag{3.17}$$

where square brackets denote the [**temporal mean**] averaged over the whole time series at each grid point; $\frac{\partial F_{\text{surf}}}{\partial X_i}$ are sensitivities derived from analytical expressions and calculated with values from the model output at every grid point and for monthly time steps; and $\beta(X_i)$ are the linear trends over the whole time period of the variables in the simulation at each grid point. The approach is limited because linear sensitivities are assigned to each variable even though the original equations are mostly nonlinear. Thus, the linearized equations only hold true for small trends in the variables. Furthermore, another error arises because the sensitivities are averaged over the full time period. The analytical expressions for the sensitivities of the CO_2 flux to each variable will be derived in the following sections.

3.2.1 Wind velocity (U)

In REcoM, the wind speed impacts the CO_2 flux via its impact on the piston velocity k_w (Orr et al., 2017):

$$k_w = (1 - \text{ice})\, a \left(\frac{\text{Sc}}{660}\right)^{-0.5} U^2 \tag{3.18}$$

where **ice** is the area fraction of surface covered by sea-ice in the respective grid cell; a is a constant (6.97×10^{-7}s/m, [2]) and **Sc** is the Schmidt number. The Schmidt number is dimensionless and I calculate it offline from monthly averaged temperature fields using the model equation by Wanninkhof (2014):

$$\mathrm{Sc} = 2116.8 - 136.25 \cdot T + 4.7353 \cdot T^2 - 0.092307 \cdot T^3 + 0.0007555 \cdot T^4 \tag{3.19}$$

with T in °C. As Sarmiento and Gruber (2006) point out, care needs to be taken when trying to deduce the mean piston velocity k_w from the mean wind speed because of its quadratic dependency. This also shows in the data used to force the FESOM-REcoM simulation. High time-mean wind velocities occur mostly in the trade wind zones and over the Southern Ocean. However, the time-mean of squared wind velocities is governed by short-time high-velocity events that take place along the subpolar storm tracks in the Southern Ocean, North Atlantic and North Pacific. The latter pattern also appears in k_w. This is why I relate the trend in the CO_2 flux to the trend in squared wind velocities ($\beta(U^2)$), not to the trend in U itself. Another reason for this is that attributing linear sensitivities as in Equation (3.16) is most accurate for linear relations, and k_w is linearly related to the squared wind velocity. The squared wind velocities are calculated directly from the JRA data product with high temporal resolution (3-hourly), which are used to force the model (Chapter 2).

From Equation (3.17), Equation (3.16) and Equation (3.18), it follows analytically that the approximate trend (β^*) in the CO_2 flux caused by winds can be estimated with:

$$\beta^*(F_{\mathrm{surf}})_{\mathrm{winds}} = \left[\frac{\partial F_{\mathrm{surf}}}{\partial (U^2)}\right] \beta(U^2) \tag{3.20}$$

$$= \left[\frac{\partial F_{\mathrm{surf}}}{\partial k_w} \frac{\partial k_w}{\partial (U^2)}\right] \beta(U^2) \tag{3.21}$$

$$= \left[\alpha \cdot \Delta \mathrm{pCO_2} \cdot (1 - \mathrm{ice}) \cdot a \left(\frac{\mathrm{Sc}}{660}\right)^{-0.5}\right] \beta(U^2) \tag{3.22}$$

Here, β^* denotes the analytical approximation. As we will see later on, the results for $\beta^*(F_{\mathrm{surf}})_{\mathrm{winds}}$ must not be confused with the results for $\beta(F_{\mathrm{surf}})_{\mathrm{winds}}$, which was derived from the difference between members of a series of simulations as described in Section 3.1.

The sensitivity of the CO_2 flux to wind-induced changes in the piston velocity depends on the pCO_2 gradient. Under rising atmospheric CO_2 concentrations, the pCO_2 gradient even changes sign in sim-A compared to sim-D at some locations. This is why the calculations outlined above are applied to both sim-D and sim-A.

3.2.2 Sea-ice concentration (ice)

As sea-ice cover at high latitudes is highly variable throughout the year, it is more useful to work with monthly climatological mean values for this variable instead on annual means. Monthly climatological mean values are denoted by square brackets $[...]^c$ with a c in superscript and trends for each month of the year are denoted by β^c. Monthly climatological mean values are obtained by grouping the data by month of the year and then calculating mean values. Trends for each month of the year are calculated analogously.

As the gas transfer velocity k_w is directly proportional to the ice-free surface area, it follows analytically from Equation (3.17), Equation (3.16) and Equation (3.18) for the contribution of any

[2] in conventional units, $6.97 \times 10^{-7}\,\mathrm{s/m} = 0.251\,\mathrm{cm\,h^{-1}(m\,s^{-1})^{-2}}$

trend in the sea-ice concentration to the trend in the CO_2 flux:

$$\beta^*(F_{\text{surf}})_{\text{ice}} = \left[\left[\frac{\partial F_{\text{surf}}}{\partial(\text{ice})}\right]^c \beta^c(\text{ice})\right] \tag{3.23}$$

$$= \left[\left[\frac{\partial F_{\text{surf}}}{\partial k_w}\frac{\partial k_w}{\partial(\text{ice})}\right]^c \beta^c(\text{ice})\right] \tag{3.24}$$

$$= \left[\left[\alpha \cdot \Delta\text{pCO}_2 \cdot (-1) \cdot a\left(\frac{\text{Sc}}{660}\right)^{-0.5} U^2\right]^c \beta^c(\text{ice})\right] \tag{3.25}$$

Here, grouping data by month of the year is useful because sea-ice concentration and the sensitivity of the CO_2 flux show a high seasonality in comparison to other variables. At times of the year when an area is fully ice covered, the difference between air and ocean partial pressures of CO_2 is often very high in that area, suggesting high CO_2 flux if the ice cover was removed. However, the strong gradient between air and ocean is not kept up at times of the year with decreasing ice over, making the CO_2 flux less sensitive to a decrease in the sea-ice concentration at the time of the year when it happens. This is why monthly climatological values for $\beta^*(F_{\text{surf}})_{\text{ice}}$ are calculated first and averaged afterwards. This reduces the estimate for the CO_2 flux trend $\beta^*(F_{\text{surf}})_{\text{ice}}$ by $\sim 60\%$ compared to when it's derived without grouping the data by month (not shown).

It was also assessed for other variables than sea-ice concentration if monthly climatological means and trends should be used preferably over the annual means. I found that for other variables than sea-ice concentration, the difference is relatively small. I limit the monthly climatological approach to sea-ice concentration for reasons of simplicity given the comparatively high error that stems from assuming linear trends and constant sensitivities over the full time period. Furthermore, (Hauck et al., 2020) found during previous model evaluation that global ocean biogeochemical models including FESOM-REcoM tend to have deficiencies in reproducing the seasonal cycle of CO_2 flux correctly.

3.2.3 Temperature (T)

Because CO_2 dissolves more easily in water with a high solubility, the rate of CO_2 transfer into the ocean scales directly with the solubility. In general, solubility is a function of temperature (T) and salinity (S). For the offline calculations, I use the expression that is also used in REcoM. In REcoM, the solubility (α) is calculated with an equation based on an empirical fit (Orr et al., 2017):

$$\begin{aligned}\alpha = \exp\Bigg(&a_1 + \frac{a_2 \cdot 100}{T_K} + a_3 \ln\Big(\frac{T_K}{100}\Big) + a_4\Big(\frac{T_K}{100}\Big)^2 \\ &+ S\Big(b1 + \frac{b_2 \cdot T_K}{100} + b_3\Big(\frac{T_K}{100}\Big)^2\Big)\Bigg)\end{aligned} \tag{3.26}$$

where T_K is the sea surface temperature in Kelvin; and a_i and b_i are the coefficients for the fit: $a_1 = -160.7333$, $a_2 = 215.4152$, $a_3 = 89.8920$, $a_4 = -1.47759$, $b_1 = 0.029941$, $b_2 = -0.027455$, $b_3 = 0.0053407$ (Orr et al., 2017).

Furthermore, it must be considered that the pCO_2 gradient between ocean and atmosphere varies with pCO_2^O, which in turn is sensitive to changes in temperature as well. This is because CO_2 solubility and dissociation constants of carbonate and bicarbonate are temperature dependent. For this dependency, I use the following approximation by Takahashi et al. (1993):

$$\frac{\partial \text{pCO}_2^O}{\partial T} \approx 0.0423^\circ\text{C}^{-1} \cdot \text{pCO}_2^O \tag{3.27}$$

which describes the temperature dependence of pCO_2^O in a closed system at constant Alk and DIC. In comparison, the temperature sensitivity of the piston velocity k_w is small and therefore neglected here. In fact, an assessment of sim-A shows that the variability of k_w is mostly dominated by winds (and, in few places, sea-ice concentration). I found that the mean temporal correlation of k_w and U^2 for ice-free grid cells is 0.9988.

Consequently, it follows analytically from Equation (3.17) and Equation (3.16) that the trend in the CO_2 flux caused by changes in SST is approximately:

$$\beta^*(F_{\text{surf}})_{\text{temp}} = \left[\frac{\partial F_{\text{surf}}}{\partial T}\right]\beta(T) \tag{3.28}$$

$$= \left[\frac{\partial F_{\text{surf}}}{\partial \alpha}\frac{\partial \alpha}{\partial T} + \frac{\partial F_{\text{surf}}}{\partial (pCO_2^O)}\frac{\partial (pCO_2^O)}{\partial T}\right]\beta(T) \tag{3.29}$$

$$= \left[k_w \cdot \Delta pCO_2 \frac{\partial \alpha}{\partial T} - k_w \alpha \frac{\partial (pCO_2^O)}{\partial T}\right]\beta(T) \tag{3.30}$$

where $\frac{\partial \alpha}{\partial T}$ can be derived from Equation (3.26) and $\frac{\partial (pCO_2^O)}{\partial T}$ is known from Equation (3.27). Throughout the calculations, I found that the term

$$\frac{\partial F_{\text{surf}}}{\partial (pCO_2^O)}\frac{\partial (pCO_2^O)}{\partial T} \tag{3.31}$$

is dominant over the term

$$\frac{\partial F_{\text{surf}}}{\partial \alpha}\frac{\partial \alpha}{\partial T} \tag{3.32}$$

by several magnitudes.

3.2.4 Salinity-normalized DIC (sDIC)

Changes in DIC can occur through multiple processes, namely by biology, circulation, surface fluxes of CO_2 and through freshwater fluxes. Most freshwater that is added at the sea surface has low DIC, so that adding freshwater decreases the ocean's DIC concentration, whereas removing freshwater through evaporation increases the DIC concentration (Sarmiento and Gruber, 2006). These processes are not considered in this section, but separately in Section 3.2.6, where the part of the CO_2 flux trend caused by freshwater fluxes and salinity ($\beta^*(F_{\text{surf}})_{\text{S+FW}}$) is calculated. Here, the interest is in the part of DIC trend which is caused by biology, circulation and surface fluxes. To remove the other part, i.e. the effect of any trend in freshwater fluxes on the trend in DIC, DIC needs to be normalized. I use the sea surface salinity as a tracer for freshwater fluxes and normalize DIC by salinity:

$$\text{sDIC} = \frac{[S]}{S}\text{DIC} \tag{3.33}$$

For the normalization, the mean surface salinity $[S]$ at every location is used, while it would also be possible to use a globally uniform reference salinity for this purpose. This choice was made because setting the temporal variation of S in proportion to the local mean salinity $[S]$ reflects an inversely proportional volume of freshwater, which is temporarily added (or removed) at this location. Here, I assume that the multidecadal trends in sDIC represent a shorter timescale than the establishment of the large-scale interregional salinity gradients. Thus, by using the local mean salinity for the normalization, I avoid outstandingly large values for the trend in sDIC in marginal seas such as the Baltic Sea. One could object that any stable regional salinity gradient can only be maintained by permanent addition or removal of freshwater, which must translate into permanent attenuation or

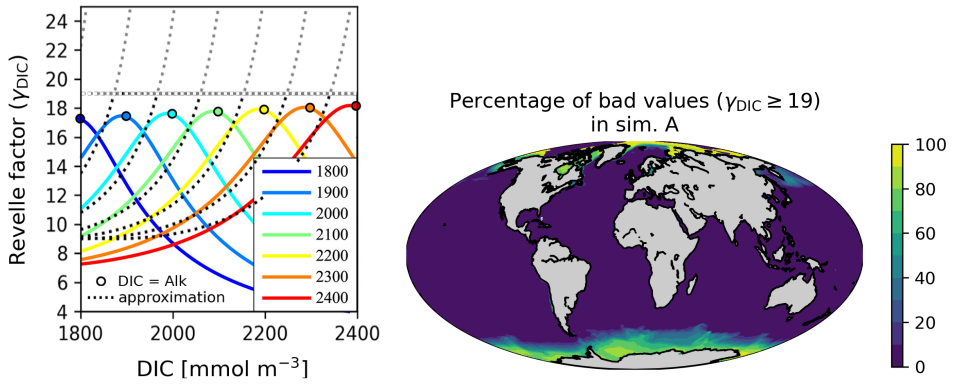

Figure 3.1: (a) The Revelle factor as a function of DIC at fixed alkalinities (noted in the legend) and the approximation (dotted lines, Equation (3.35)) used in here with a cut at $\gamma_{DIC} = 19$; graphic adapted from Fassbender et al. (2017). (b) The percentage of values where Equation (3.35) gives $\gamma_{DIC} > 19$ in simulation A because Alk and DIC are too similar (based on monthly mean values). The pattern is similar in simulation D and almost identical for γ_{Alk}.

magnification of the trend in DIC, which would require a correction in the form of a globally uniform normalization constant. The choice of normalization can thus easily be put into question. However, by testing with a globally uniform normalization constant and with local values, I found that the choice is mostly irrelevant for the trends in sDIC in the open ocean.
The sensitivity of pCO_2^O to changes in DIC is described by the buffer factor for DIC, the Revelle factor γ_{DIC}:

$$\frac{\partial(pCO_2^O)}{\partial(DIC)} = \gamma_{DIC} \cdot \frac{pCO_2^O}{DIC} \tag{3.34}$$

I use the approximation of Sarmiento and Gruber (2006, Eq. 8.3.16):

$$\gamma_{DIC} \approx \frac{3 \cdot Alk \cdot DIC - 2 \cdot DIC^2}{(2 \cdot DIC - Alk)(Alk - DIC)} \tag{3.35}$$

This equation was derived by Sarmiento and Gruber (2006) from the carbonate chemistry, neglecting borate and furthermore using several approximations in order to replace bicarbonate and carbonate ion concentrations with DIC and Alk. Their formulation suits my needs well, as only DIC and alkalinity are available from the model output. A more accurate formulation was derived by Egleston et al. (2010), but it is not expressed as a function of DIC and alkalinity. Egleston et al. (2010) state that the equation used here provides values for γ_{DIC} with errors on the order of 20-30%. However, it is not applicable under conditions where DIC and Alk are similar, because the term (Alk - DIC) appears in the denominator. Egleston et al.'s (2010) expression for γ_{DIC} reaches maximum values at DIC=Alk, which are in the range of $\gamma_{DIC} \approx 19.4$ at DIC = 3.5 mmol C m^{-3}, $\gamma_{DIC} \approx 18.75$ at DIC = 2.25 mmol C m^{-3} and $\gamma_{DIC} \approx 15$ at DIC = 1.5 mmol C m^{-3}. This is why I set $\gamma_{DIC} = 19$ where Equation (3.35) gives values larger than 19 (Figure 3.1a). Typically, DIC is sufficiently smaller than Alk. It is shown in Figure 3.1b where this is not the case. Globally, less than 4% of data points in sim-D (8% in sim-A) are affected by the correction needed for too similar DIC and Alk. Those are at high latitudes either in the Arctic ocean where Alk is low ($\leq$ 2.25 mmol C m^{-3}) or in the Southern Ocean where DIC is high ($\geq$ 2.25 mmol C m^{-3}). In sim-A, more data points are affected than in sim-D, because DIC in the Southern Ocean is higher in sim-A under the influence of rising atmospheric CO_2.

Following Lovenduski et al. (2007), the approximate trend in the CO_2 flux caused by the trend in

sDIC is derived analytically from Equation (3.17), Equation (3.16) and Equation (3.33):

$$\beta^*(F_{\text{surf}})_{\text{sDIC}} = \left[\frac{S}{[S]}\frac{\partial F_{\text{surf}}}{\partial(\text{DIC})}\right]\beta(\text{sDIC}) \tag{3.36}$$

$$= \left[\frac{S}{[S]}\frac{\partial F_{\text{surf}}}{\partial(\text{pCO}_2^{\text{O}})}\frac{\partial(\text{pCO}_2^{\text{O}})}{\partial(\text{DIC})}\right]\beta(\text{sDIC}) \tag{3.37}$$

$$= \left[-\frac{S}{[S]}\alpha k_w \frac{\partial(\text{pCO}_2^{\text{O}})}{\partial(\text{DIC})}\right]\beta(\text{sDIC}) \tag{3.38}$$

where $\frac{\partial(\text{pCO}_2^{\text{O}})}{\partial(\text{DIC})}$ is known from Equation (3.34) and Equation (3.35). From this, it also becomes obvious why sim-A cannot be used to approximate the effect of climate-related variability of sDIC on the CO_2 flux. Firstly, a large part of the variability in sDIC in sim-A is not climate-related, but caused by the increase of atmospheric CO_2. Secondly, a one-way relation between sDIC and ΔpCO_2 is assumed for the calculation, according to which changes in sDIC alter pCO_2^{O} and thus ΔpCO_2 while pCO_2^{A} remains constant. Indeed, pCO_2^{A} is constant in sim-D. However, pCO_2^{A} is far from constant in sim-A. The linear approximation does not capture that in sim-A, pCO_2^{O} largely follows pCO_2^{A} , so that the trend in ΔpCO_2 is much smaller than the sDIC-related trend in pCO_2^{O}.

3.2.5 Salinity-normalized alkalinity (sAlk)

Analogously to DIC, alkalinity is normalized by the temporal mean salinity at each grid point:

$$\text{sAlk} = \frac{[S]}{S}\text{Alk} \tag{3.39}$$

As for DIC, the sensitivity of pCO_2^{O} to changes in alkalinity is described by its buffer factor γ_{Alk}:

$$\frac{\partial(\text{pCO}_2^{\text{O}})}{\partial(\text{Alk})} = \gamma_{\text{Alk}} \cdot \frac{\text{pCO}_2^{\text{O}}}{\text{Alk}} \tag{3.40}$$

The buffer factor for alkalinity is (Sarmiento and Gruber, 2006, Eq. 8.3.17):

$$\gamma_{\text{Alk}} \approx -\frac{\text{Alk}^2}{(2\cdot\text{DIC}-\text{Alk})(\text{Alk}-\text{DIC})} \tag{3.41}$$

In contrast to γ_{DIC}, γ_{Alk} is negative. Thus, the explicit expression for γ_{Alk} by Egleston et al. (2010) reaches minimum values for Alk=DIC ($\gamma_{\text{Alk}} \approx -17.3$ at Alk = 2.25 mmol C m^{-3}). Therefore, I set $\gamma_{\text{Alk}} = -18$ everywhere where Equation (3.41) gives values ≤ -18. The pattern of values where Alk and DIC are too similar is almost identical to the pattern shown in Figure 3.1b for γ_{DIC}.

The trend in the CO_2 flux caused by variations in sAlk is derived analytically from Equation (3.17), Equation (3.16) and Equation (3.39) following Lovenduski et al. (2007):

$$2\beta^*(F_{\text{surf}})_{\text{sAlk}} = \left[\frac{S}{[S]}\frac{\partial F_{\text{surf}}}{\partial(\text{Alk})}\right]\beta(\text{sAlk}) \tag{3.42}$$

$$= \left[\frac{S}{[S]}\frac{\partial F_{\text{surf}}}{\partial(\text{pCO}_2^{\text{O}})}\frac{\partial(\text{pCO}_2^{\text{O}})}{\partial(\text{Alk})}\right]\beta(\text{sAlk}) \tag{3.43}$$

$$= \left[-\frac{S}{[S]}\alpha k_w \frac{\partial(\text{pCO}_2^{\text{O}})}{\partial(\text{Alk})}\right]\beta(\text{sAlk}) \tag{3.44}$$

where $\frac{\partial(\text{pCO}_2^{\text{O}})}{\partial(\text{Alk})}$ is known from Equation (3.40) and Equation (3.41).

3.2.6 Salinity and freshwater fluxes (S+FW)

Salinity affects the CO_2 flux through multiple processes. In the following, the impact of salinity on the trend in the CO_2 flux will be outlined:

Sensitivity of α to salinity: From Equation (3.26) it becomes obvious that the solubility of CO_2 at the ocean surface is more sensitive to temperature than salinity (it changes about 1.3 $\mathrm{mmol\,l^{-1}atm^{-1}}$ per °C and 0.2 $\mathrm{mmol\,l^{-1}atm^{-1}}$ per psu). Nonetheless, as the effect of salinity on solubility might be non-negligible in places with low temperatures and a high variability of salinity, $\frac{\partial \alpha}{\partial S}$ is derived from Equation (3.26).

Sensitivity of $\mathrm{pCO_2^O}$ to salinity: Sarmiento and Gruber (2006) state that at constant alkalinity and DIC, the buffer factor for salinity is $\gamma_S \approx 1$, so that

$$\frac{\partial(\mathrm{pCO_2^O})}{\partial S} \approx \frac{\mathrm{pCO_2^O}}{S} \tag{3.45}$$

Freshwater fluxes: Most variations in salinity in the surface ocean are due to freshwater fluxes. Freshwater contains very little DIC and Alk. Therefore, together with most changes in salinity, DIC and alkalinity are proportionally diluted or concentrated, namely $\Delta\mathrm{DIC} = \Delta S/S \cdot \mathrm{DIC}$ and $\Delta\mathrm{Alk} = \Delta S/S \cdot \mathrm{Alk}$. Sarmiento and Gruber (2006) state that this increases the effect of pure salinity-driven changes in $\mathrm{pCO_2^O}$ by about 60%.

Analogously, a trend in freshwater fluxes traced by salinity is proportionally translated into a trend in DIC and Alk:

$$\beta(\mathrm{DIC})_{\mathrm{FW}} = \beta(S)\left[\frac{\mathrm{DIC}}{S}\right] \qquad \text{and} \qquad \beta(\mathrm{Alk})_{\mathrm{FW}} = \beta(S)\left[\frac{\mathrm{Alk}}{S}\right] \tag{3.46}$$

The effect of $\beta(\mathrm{DIC})_{\mathrm{FW}}$ and $\beta(\mathrm{Alk})_{\mathrm{FW}}$ on $\mathrm{pCO_2^O}$ is calculated with the respective buffer factors for DIC and Alk as described in Section 3.2.4 and Section 3.2.5.

Combined effect Taking together the pure effect of salinity on solubility and on $\mathrm{pCO_2^O}$ and the change of $\mathrm{pCO_2^O}$ induced by freshwater fluxes, the resulting trend in the CO_2 flux is:

$$\beta^*(F_{\mathrm{surf}})_{\mathrm{S+FW}} = \left[\frac{\partial F_{\mathrm{surf}}}{\partial S} + \frac{\partial F_{\mathrm{surf}}}{\partial \mathrm{DIC}} \cdot \frac{\mathrm{DIC}}{S} + \frac{\partial F_{\mathrm{surf}}}{\partial \mathrm{Alk}} \cdot \frac{\mathrm{Alk}}{S}\right]\beta(S) \tag{3.47}$$

where the pure effect of salinity is

$$\frac{\partial F_{\mathrm{surf}}}{\partial S} = k_w \Delta\mathrm{pCO_2}\frac{\partial \alpha}{\partial S} - \alpha k_w \frac{\partial(\mathrm{pCO_2^O})}{\partial S} \tag{3.48}$$

and the freshwater fluxes are

$$\frac{\partial F_{\mathrm{surf}}}{\partial \mathrm{DIC}} \cdot \frac{\mathrm{DIC}}{S} = -\alpha k_w \frac{\partial(\mathrm{pCO_2^O})}{\partial \mathrm{DIC}} \cdot \frac{\mathrm{DIC}}{S} \tag{3.49}$$

and

$$\frac{\partial F_{\mathrm{surf}}}{\partial \mathrm{Alk}} \cdot \frac{\mathrm{Alk}}{S} = -\alpha k_w \frac{\partial(\mathrm{pCO_2^O})}{\partial \mathrm{Alk}} \cdot \frac{\mathrm{Alk}}{S} \tag{3.50}$$

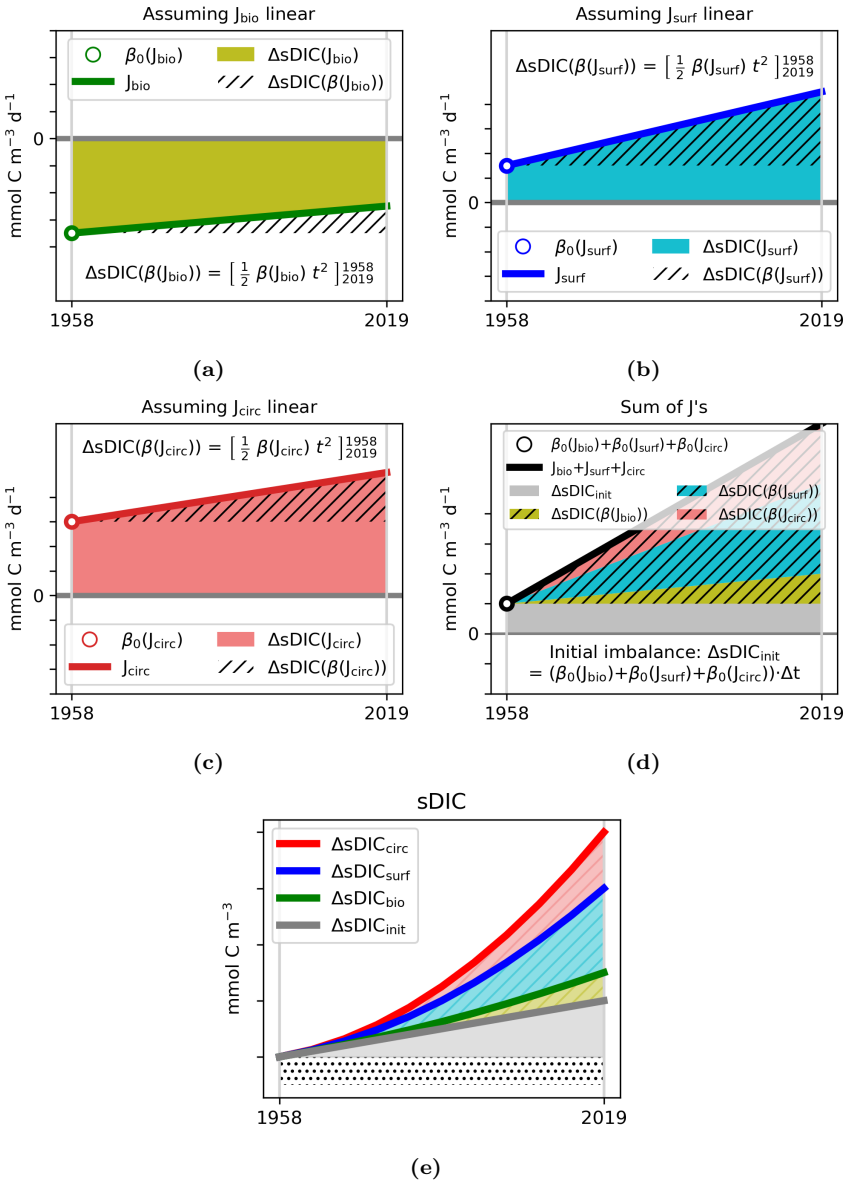

Figure 3.2: (a) A linear model (green line) for the loss rate of mixed layer sDIC due to biological export (J_{bio}) described by Equation (3.52). J_{bio} is always negative, i.e. a flux of sDIC from the mixed layer into the deep. The filled area defined by the J_{bio}-curve represents the change in sDIC due to biological losses. In particular, the change of sDIC due to the trend in the biological loss rate ($\beta(J_{\mathrm{bio}})$) is marked with hatches. The graphic is not to scale. Analogously, (b) and (c) illustrate linear models for J_{surf} and J_{circ} (blue line, red line) and the resulting change in sDIC (filled area defined by the respective curves). (d) The sum of J_{bio}, J_{surf} and J_{circ} (black line). The filled area represents the net change in sDIC. In red/with hatches: change in sDIC due to a trend in J_{bio}; in blue/with hatches: change in sDIC due a trend in J_{surf}; in green/with hatches: change in sDIC due to a trend in J_{bio}; in gray: change in sDIC due to the initial imbalance of $\beta_0(J_{\mathrm{bio}})$, $\beta_0(J_{\mathrm{surf}})$ and $\beta_0(J_{\mathrm{circ}})$ (circles in a, b and c). (e) A cubic model for the change in sDIC described by Equation (3.55). The net change in sDIC arises from the sum of: change in sDIC due to a trend in J_{bio} (red line, Equation (3.59)); change in sDIC due a trend in J_{surf} (blue line); change in sDIC due to a trend in J_{bio} (green line); change in sDIC due to the initial imbalance of $\beta_0(J_{\mathrm{bio}})$, $\beta_0(J_{\mathrm{surf}})$ and $\beta_0(J_{\mathrm{circ}})$ (gray line).

3.2.7 Biology and circulation (J_{bio} and J_{circ})

As described above, part of the trends in the air-sea CO_2 fluxes can be attributed to a trend in sDIC. Furthermore, the sDIC trend itself can be decomposed into contributions from circulation (circ), biology (bio) and fluxes of CO_2 at the air-sea interface (surf). They can be estimated following Lovenduski et al. (2007):

$$\frac{d(\text{sDIC})}{dt} = J_{\text{bio}} + J_{\text{surf}} + J_{\text{circ}} \tag{3.51}$$

where t is time; sDIC is salinity-normalized DIC; J_{bio} is the change of sDIC caused by the export production; J_{surf} is caused by the air-sea flux of CO_2 and J_{circ} is caused by the transport of sDIC with the ocean circulation. The sDIC concentration is assumed to be uniform throughout depth within the mixed layer and for simplicity, surface values of sDIC are used for the calculations. Thereby, J_{bio}, J_{surf} and J_{circ} describe the temporal change of sDIC concentrations at the surface and throughout the mixed layer. Hence, like sDIC, J_{bio}, J_{surf} and J_{circ} have units per volume (of mixed layer water), and per time.

J_{bio} is calculated from monthly mean model output. For this, I use the detritus concentration at the bottom of the mixed layer (MLD), defined by a density-threshold criterion ($0.03\,\text{kg}\,\text{m}^{-3}$). In REcoM, detritus exists in the form of particulate organic carbon and $CaCO_3$. The particles have a vertical sinking velocity; unlike dissolved carbon which only follows the circulation. To get the daily flux of detritus through the base of the mixed layer (F_{bio}) from the detritus concentration, the detritus concentration is multiplied with the sinking velocity at the base of the mixed layer, which is $v_{\text{detritus}} = 0.0288\,\text{d}^{-1} \cdot \text{MLD} + 20\,\text{m}\,\text{d}^{-1}$. The flux of detritus through the base of the mixed layer is then divided by the climatological depth of the mixed layer (i.e. the MLD averaged from 1958-2019 for each month of the year) to obtain J_{bio} in units of $\text{mmol}\,\text{C}\,\text{m}^{-3}\text{d}^{-1}$.

Analogously, J_{surf} is the air-sea flux of CO_2 (F_{surf}) divided by the climatological depth of the mixed layer. To obtain J_{surf} and J_{bio}, I divide by the climatological mixed layer depth rather than the monthly MLD in order to remove the effect of trends in the MLD on J_{surf} and J_{bio}. The change in the sDIC concentration that occurs through the dispersion of detritus losses and surface carbon fluxes over an interannually variable mixed layer depth is thus attributed to the circulation term.

Here, we go beyond the analysis of Lovenduski et al. (2007) by calculating the trend in sDIC due to the surface flux, the export flux and the circulation [$\text{mmol}\,\text{C}\,\text{m}^{-3}\,\text{per yr}$] rather than the trend in the sDIC tendencies [$\text{mmol}\,\text{C}\,\text{m}^{-3}\text{d}^{-1}\,\text{per yr}$]; i.e. we estimate $\beta(\text{sDIC})_{\text{bio}}$, $\beta(\text{sDIC})_{\text{surf}}$ and $\beta(\text{sDIC})_{\text{circ}}$ from $\beta(\text{J}_{\text{bio}})$, $\beta(\text{J}_{\text{surf}})$ and $\beta(\text{J}_{\text{circ}})$. To begin with, I assume that J_{bio}, J_{surf} and J_{circ} can be described well with linear functions (Figure 3.2). To calculate the trends in J_{bio} and J_{surf}, I attribute linear fits to them using a least-square linear regression. The linear fits have the form

$$\text{J}_{\text{bio}} \approx \beta(\text{J}_{\text{bio}}) \cdot t + \beta_0(\text{J}_{\text{bio}}) \tag{3.52}$$

and

$$\text{J}_{\text{surf}} \approx \beta(\text{J}_{\text{surf}}) \cdot t + \beta_0(\text{J}_{\text{surf}}) \tag{3.53}$$

where $\beta_0(...)$ is the y-intercept at the beginning of the time series in 1958 and $\beta(...)$ is the trend or slope (Figures 3.2a and 3.2b). Analogously, a linear equation for J_{circ} exists (Figure 3.2c):

$$\text{J}_{\text{circ}} \approx \beta(\text{J}_{\text{circ}}) \cdot t + \beta_0(\text{J}_{\text{circ}}) \tag{3.54}$$

The coefficients $\beta(\text{J}_{\text{circ}})$ and $\beta_0(\text{J}_{\text{circ}})$ are now to be determined as these cannot be as easily obtained directly from the model output. Because J_{bio}, J_{surf} and J_{circ} and thus the derivative of sDIC $\frac{d}{dt}(\text{sDIC})$ (Equation (3.51)) are described with linear equations, their respective integrals are cubic equations (Figure 3.2e). Thus, a cubic equation for sDIC is introduced. The equation for sDIC has the form

$$\text{sDIC} \approx \lambda_2(\text{sDIC}) \cdot t^2 + \lambda_1(\text{sDIC}) \cdot t + \lambda_0(\text{sDIC}) \tag{3.55}$$

The coefficients $\lambda_2(\text{sDIC})$, $\lambda_1(\text{sDIC})$ and $\lambda_0(\text{sDIC})$ are calculated by applying a 2nd order polynomial least square fit to sDIC. From Equation (3.51), it follows that the time-derivative of Equation (3.55) is equal to the sum of Equation (3.52), Equation (3.53) and Equation (3.54):

$$\begin{aligned} 2 \cdot \lambda_2(\text{sDIC}) \cdot t + \lambda_1(\text{sDIC}) = \quad & (\beta(\text{J}_{\text{bio}}) + \beta(\text{J}_{\text{surf}}) + \beta(\text{J}_{\text{circ}})) \cdot t \\ & + (\beta_0(\text{J}_{\text{bio}}) + \beta_0(\text{J}_{\text{surf}}) + \beta_0(\text{J}_{\text{circ}})) \end{aligned} \tag{3.56}$$

From this, the coefficients $\beta(\text{J}_{\text{circ}})$ and $\beta_0(\text{J}_{\text{circ}})$ can be calculated as the residual:

$$\beta(\text{J}_{\text{circ}}) = 2 \cdot \lambda_2(\text{sDIC}) - \big(\beta(\text{J}_{\text{bio}}) + \beta(\text{J}_{\text{surf}})\big) \tag{3.57}$$

$$\beta_0(\text{J}_{\text{circ}}) = \lambda_1(\text{sDIC}) - \big(\beta_0(\text{J}_{\text{bio}}) + \beta_0(\text{J}_{\text{surf}})\big) \tag{3.58}$$

The parts of the trend in sDIC caused by $\beta(\text{J}_{\text{bio}})$, $\beta(\text{J}_{\text{surf}})$ and $\beta(\text{J}_{\text{circ}})$ can be quantified by applying linear fits to the cubic terms of the integrals of Equation (3.52), Equation (3.53) and Equation (3.54), which are (Figure 3.2e):

$$\Delta\text{sDIC}_{\text{bio}} \approx 0.5 \cdot \beta(\text{J}_{\text{bio}}) \cdot t^2; \qquad \Delta\text{sDIC}_{\text{surf}} \approx 0.5 \cdot \beta(\text{J}_{\text{surf}}) \cdot t^2; \qquad \Delta\text{sDIC}_{\text{circ}} \approx 0.5 \cdot \beta(\text{J}_{\text{circ}}) \cdot t^2 \tag{3.59}$$

Another part of the trend in sDIC arises because the sum of $\beta_0(\text{J}_{\text{bio}}) + \beta_0(\text{J}_{\text{surf}}) + \beta_0(\text{J}_{\text{circ}}) = \lambda_1(\text{sDIC})$ is not necessarily zero (Figures 3.2d and 3.2e). In this thesis, this is referred to as the "initial imbalance", because in the linear model, it arises from the imbalance of J_{bio}, J_{surf} and J_{circ} at the beginning of the time series. The trend in sDIC due to the initial imbalance is quantified as (Figure 3.2e):

$$\beta(\text{sDIC})_{\text{init}} = \beta_0(\text{J}_{\text{bio}}) + \beta_0(\text{J}_{\text{surf}}) + \beta_0(\text{J}_{\text{circ}}) = \lambda_1(\text{sDIC}) \tag{3.60}$$

Note that because deriving the integral is not a linear operation, my results depend on the order of the calculations. In here, I applied a linear fit to J_{bio} and J_{surf} in the beginning and derived the trend in J_{circ} from that. Consequently, the net trend in sDIC is always equal to the sum of its components, i.e. the sum of $\beta(\text{sDIC})_{\text{bio}}$, $\beta(\text{sDIC})_{\text{surf}}$, $\beta(\text{sDIC})_{\text{circ}}$ and $\beta(\text{sDIC})_{\text{init}}$. Alternatively, it is possible to obtain monthly or annual values of J_{circ} by finite differencing of sDIC (Equation (3.51)) and afterwards derive the trend in J_{circ} from that. According to the latter, the net trend in sDIC might be different from the sum of its components. The discrepancy between both methods gets larger the more J_{bio}, J_{surf} and J_{circ} deviate from the linear approximation owing to interannual and decadal variability.

3.3 Regional analysis

For regional analyses, I divide the ocean area into six regions with sub-regions (Figure 3.3a), based on the biomes defined by Fay and McKinley (2014). In their definition, Fay and McKinley (2014) aimed to capture large-scale biogeochemical functions of the open ocean with the minimum possible number of regions. Their biomes have been defined based on four criteria in observational data: Sea surface temperature, climatological maximum mixed layer depth, spring or summer chlorophyll-a concentration and sea-ice concentration. Geographically, the biomes roughly resemble global latitudinal bands (Figure 3.3a).

I divide the ocean into 28 sub-regions based on the Fay and McKinley (2014) biomes and further taking into account the hemisphere (N/S) and ocean basin (Atlantic, Pacific, Indian). In a first assessment, I calculated the mean and trend in the CO_2 flux for each of the 28 sub-regions, in order to identify regions with similar characteristics. For sim-A, the means and trends are shown in Figure 3.3b. The sub-regions were then grouped, resulting in 6 regions plus the "other" in total, namely: The ice biome (ICE), the North Atlantic subpolar seasonally stratified biome (SPSS), the Southern Ocean SPSS, the subtropical seasonally stratified biome without the South Pacific sector (STSS w/o SP), the subtropical permanently stratified biome (STPS), the equatorial biome (EQU)

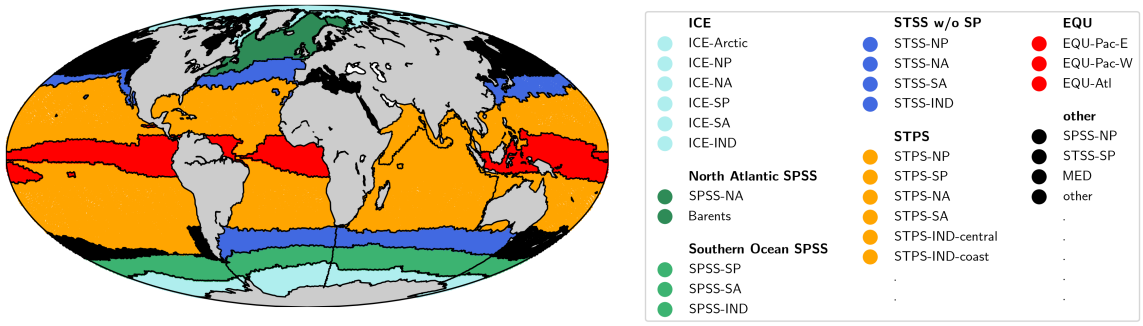

(a) Regions with sub-regions.

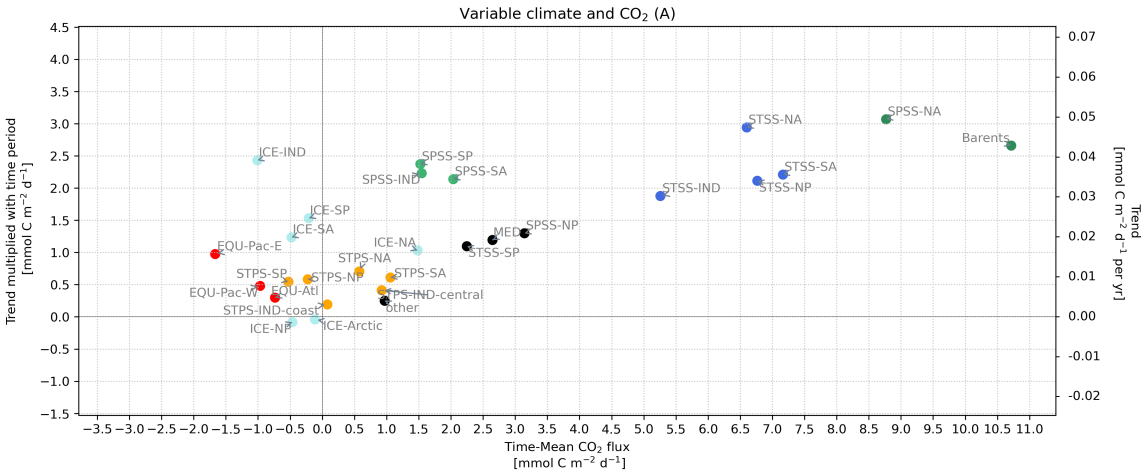

(b) Mean and trend of CO_2 flux for all sub-regions in sim-A. Axis scaling is chosen so that the x-axis (mean value) and left y-axis (change over the time period 1958-2019) are proportional (1:1).

Figure 3.3

and other. These regions will be analyzed in this thesis and are described in more detail in the following.

The regions (sorted from high latitudes to low latitudes) with their sub-regions are:

The ice biome (ICE) The ice biome is characterized by cool, polar waters that have a sea-ice concentration of at least 50% during some part of the year (Fay and McKinley, 2014). The following sub-regions are grouped together:

- ICE-Arctic
- ICE-NP (North Pacific)
- ICE-NA (North Atlantic)
- ICE-SP (Pacific sector of the Southern Ocean)
- ICE-SA (Atlantic sector of the Southern Ocean)
- ICE-IND (Indian Ocean sector of the Southern Ocean)

The sub-regions grouped together in ICE tend to be regions of outgassing, which is strongly weakened under rising atmospheric CO_2 concentrations. However, the spread within the ice biome is large.

The North Atlantic subpolar seasonally stratified biome (North Atlantic SPSS) The SPSS is characterized by high chlorophyll concentrations. In the subpolar zone, where the SPSS regions are located, positive wind stress curl causes divergent surface flow. The divergence leads to upwelling from below, which brings nutrients to the surface that allow for high chlorophyll concentrations (Fay and McKinley, 2014). In our simulations, the North Atlantic SPSS, including the Barents Sea, has very high CO_2 flux density (more than $8.5\,\mathrm{mmol\,C\,m^{-2}d^{-1}}$ in sim-A). It is much smaller than all other biomes and has only two sub-regions, which are:

- SPSS-NA
- SPSS-Barents

The Southern Ocean SPSS In the Southern Ocean SPSS, the mean CO_2 flux is lower than in the North Atlantic SPSS (less than $2.5\,\mathrm{mmol\,C\,m^{-2}d^{-1}}$ in sim-A). As we will see later, another difference of the Southern Ocean and North Atlantic SPSS is that in the Southern Ocean SPSS, climate variability causes negative trends in the CO_2 flux, whereas the North Atlantic SPSS is one of the few areas worldwide where climate variability causes positive trends (Figure S22c). In the Southern Ocean SPSS, the following sub-regions are grouped together:

- SPSS-SP
- SPSS-SA
- SPSS-IND

The subtropical seasonally stratified biome without South Pacific sector (STSS w/o SP) The STSS is an area of downwelling driven by negative wind stress curl in the subtropics. Due to deep winter mixed layers, nutrient supply at the surface is sufficient for intermediate chlorophyll concentrations (Fay and McKinley, 2014) and high CO_2 fluxes (between 5-7.5 $\mathrm{mmol\,C/m^2}$ /d in sim-A). I exclude the South Pacific sector as the CO_2 flux is lower there (Figure 3.3b). The following sub-regions are grouped together:

- STSS-NP
- SPSS-NA
- SPSS-SA
- SPSS-IND

The subtropical permanently stratified biome (STPS) In the STPS, downwelling due to negative wind stress curl occurs together with year-round stratification and shallow mixed layers. This leads to low chlorophyll concentrations (Fay and McKinley, 2014). In our simulations, the STPS are regions of weak CO_2 fluxes, of which some are positive and some negative. Under rising atmospheric CO_2 concentrations, they turn with time into regions with positive fluxes. Area-wise, the STPS is the largest of the biomes, spanning about half the world ocean's area, whereas all other biomes include around 1/8 of the global ocean area each (excluding the comparatively tiny North Atlantic SPSS). The following sub-regions are grouped together:

- STPS-NP (North Pacific)
- STPS-SP (South Pacific)
- STPS-NA (North Atlantic)
- STPS-SA (South Atlantic)
- STPS-IND-central (majority of Indian Ocean)
- STPS-IND-coast (fragmented areas of Indian Ocean including Arabian Sea, Bay of Bengal, Timor Sea and Great Australian Bight)

The equatorial biome (EQU) The EQU is defined by warm temperatures and moderate chlorophyll concentrations due to equatorial upwelling. There are latitudinal variations as easterlies blow across the EQU region. In the Pacific, warm waters pool in the western half of the basin. In the Indian Ocean, the equatorial region is grouped with the STPS region due to seasonally varying circulation patterns associated with the monsoon (Fay and McKinley, 2014). The EQU is characterized by outgassing of CO_2. The following sub-regions are grouped together:

- EQU-Pac-E (East Pacific)
- EQU-Pac-W (West Pacific)
- EQU-Atl

Other Of the rest of the ocean area, the largest part is the SPSS-NP followed by the STSS-SP. The other part are marginal seas, such as the Mediterranean, Baltic Sea, Hudsonbay and Red Sea. These regions are included in the global analysis, but not discussed in the regional analysis in this thesis. The sub-regions are:

- SPSS-NP (North Pacific)
- STSS-SP (South Pacific)
- MED (Mediterranean)
- other

Chapter 4

Results

4.1 Global overview of mean and trends in the CO_2 flux

4.1.1 Mean CO_2 flux and regional variability

The globally integrated temporal mean CO_2 flux is an uptake $1.85\,\mathrm{PgC\,yr^{-1}}$ in the historical simulation (sim-A), which is equivalent to a mean flux density per surface area of $1.17\,\mathrm{mmol\,C\,m^{-2}\,d^{-1}}$. While the global ocean acts as a mean sink, the temporal mean CO2 flux density shows high regional variability. The regional variability is similar in all simulations (Figure 4.1a, Figure S1 and Figure S2). This is because firstly, the climate-induced changes are mostly small in comparison to regional differences in the temporal mean CO_2 flux densities. Thus, the temporal mean is similar in the simulations with and without climate variability. Secondly, the regional variability of the CO_2 flux density is governed by natural carbon and the impact of anthropogenic carbon on the regional variability is minor. Thus, the similarity is preserved in the simulations with and without anthropogenic carbon. In order to avoid redundancies, only the regional variability of the CO_2 flux density in the historical simulation is described in the next paragraph and where necessary, differences to the other simulations are pointed out.

Overall, the CO_2 flux density increases with latitude (Figure 4.1a). It is small in magnitude in the tropics and subtropics, i.e. in the EQU and STPS biomes. The low values in the tropics and subtropics result from a combination of small pCO_2 gradients and slow gas transfer velocities. Firstly, the low pCO_2 gradients are probably related to the low biological export in the STPS (Figure S15a), a stable stratification and long residence time of water at the surface. Secondly, the gas transfer coefficients ($\alpha \cdot k_w$) are small because of small mean squared wind velocities (less than $60\,(\mathrm{m/s})^2$) and temperature-related low solubility of CO_2. The exception to this is the South Pacific STPS, where the strongest outgassing of CO_2 per surface area on the globe is found. This is caused by upwelling off the Chilean and Peruvian coast. More outgassing in relation to upwelling systems is seen in the North Pacific off the North American West Coast and in the South Atlantic at the Benguela upwelling system. The STPS is basin-wise either a source (Pacific) or a sink (Atlantic, Indian) for atmospheric CO_2.

The STSS biome, which is located approximately between 40-55° in both hemispheres, contains regions of high CO_2 flux density directed into the ocean (Figure 4.1a). Towards higher latitudes, temperatures decrease and the mean squared wind velocities increase, allowing for fast air-sea gas transfer in the STSS biome. In addition, seasonal mixing allows for a high biological productivity and thus biological export of surface carbon below the mixed layer, which is partly balanced by the uptake of atmospheric carbon at the air-sea interface or by lateral and vertical interior ocean carbon transport. The STSS biome also contains regions of mode water formation in both hemispheres (Hanawa and D.Talley, 2001). The subduction of mode waters in the subtropics is an efficient

pathway for anthropogenic carbon into the ocean's interior (Gruber et al., 2019), of which some is upwelled in the tropics within a few decades (DeVries et al., 2017). In the Northern hemisphere, the STSS biomes are additionally affected by western boundary currents. Western boundary currents transport warm subtropical waters with low DIC concentrations poleward. While the waters cool, they take up carbon from the atmosphere (Völker et al., 2002). Western boundary currents are also associated with the formation of mode waters, thereby leading to the subduction of more CO_2 (Fassbender et al., 2017). The STSS biome accounts for more than a third of the globally integrated CO_2 flux directed into the ocean (Figure 4.2a).

Further poleward in the SPSS biome, the CO_2 flux density shows an interhemispheric contrast (Figure 4.1a). The historical CO_2 flux density is only 1.5-2.0 $\mathrm{mmol\,C\,m^{-2}d^{-1}}$ in the Southern Ocean SPSS in sim-A and even close to zero in sim-B (Figure S2a). On the one hand, the Southern Ocean SPSS is an area of relatively high export production in comparison to the subtropics, so that CO_2 is removed from the surface through biology. On the other hand, the Southern Ocean SPSS is characterized by wind-driven upwelling in the Antarctic zone, which brings DIC rich waters to the surface (Lovenduski et al., 2007). Apparently, these two processes largely compensate in the control simulation. In sim-A, the increase of anthropogenic carbon compensates for the upwelling and the Southern Ocean SPSS has become a considerable sink for CO_2 during the considered time period (10% of the globally integrated CO_2 flux into the ocean, Figure 4.2a). In contrast to the rather low CO_2 flux densities in the Southern Ocean SPSS, the North Atlantic SPSS features the highest mean CO_2 flux density on the globe ($8.8\,\mathrm{mmol\,C\,m^{-2}d^{-1}}$). The mean biological export of sDIC (J_{bio}) is about twice in the North Atlantic SPSS compared to the Southern Ocean SPSS (Figure 4.14b). Furthermore, the North Atlantic circulation is impacted by the North Atlantic Current, which brings in subtropical waters that get undersaturated as they cool (Völker et al., 2002). Additonally, deep water formation in the North Atlantic transports carbon away from the surface layers, thereby facilitating more oceanic CO_2 uptake at the air-sea interface (Sabine et al., 2004).

In the ICE biomes, the CO_2 flux density is small in both hemispheres (Figure 4.1a). Here, the squared wind velocities are smaller than in the mid-latitudes and sea-ice cover prevents air-sea exchange at least during parts of the year. In the North Atlantic ICE region, which is geographically influenced by the North Atlantic SPSS, the CO_2 flux is directed into the ocean. All other ICE regions are areas of outgassing (Figure 4.2a).

Differences between the simulations Even though there are only small differences in the regional variability of the CO_2 flux densities between all simulations, these differences give rise to key differences between the simulations regarding the regionally and globally integrated CO_2 flux (Table 4.1). The globally integrated CO_2 flux is higher, i.e. more uptake, in the simulations with anthropogenic carbon (*A*, *C*, *E*, *F*: 1.85-1.95 $\mathrm{Pg\,C\,yr^{-1}}$, Table 4.1) compared to the simulations with constant atmospheric CO_2 (*B*, *D*: 0.23-0.32 $\mathrm{Pg\,C\,yr^{-1}}$). Moreover, the globally integrated CO_2 flux is slightly reduced by 0.03-0.10 $\mathrm{Pg\,C\,yr^{-1}}$ in the simulations with climate variability compared to the simulations without climate variability, i.e. in sim-A, sim-E and sim-F in comparison to sim-C and further sim-D in comparison to sim-B (Table 4.1).

In the control simulation (sim-B), the globally integrated CO_2 flux is a small CO_2 uptake of the ocean. In contrast, the real pre-industrial ocean had an outgassing flux estimated between -0.45 ± 0.18 $\mathrm{PgC\,yr^{-1}}$ (Jacobson et al., 2007) and -0.78 ± 0.41 $\mathrm{PgC\,yr^{-1}}$ (Resplandy et al., 2018) due to carbon transported into the ocean by rivers. However, in this set-up of FESOM-REcoM, the riverine carbon flux is not included. Thus, the globally integrated CO_2 flux should ideally be zero in the control simulation. Reasons for the difference to zero can be simplifications of the carbon cycle and biases in atmospheric forcing, modelled circulation and biological productivity. Apart from this bias, the regional fluxes mostly cancel out in the global integral in sim-B (Figure 4.2a).

Overall, all regions have a smaller or more negative integrated CO_2 flux in sim-B than in sim-A. In sim-B, the most important contribution to the integrated outgassing of carbon comes from the STPS and in particular from the South Pacific STPS, which is dominated by the Peruvian and

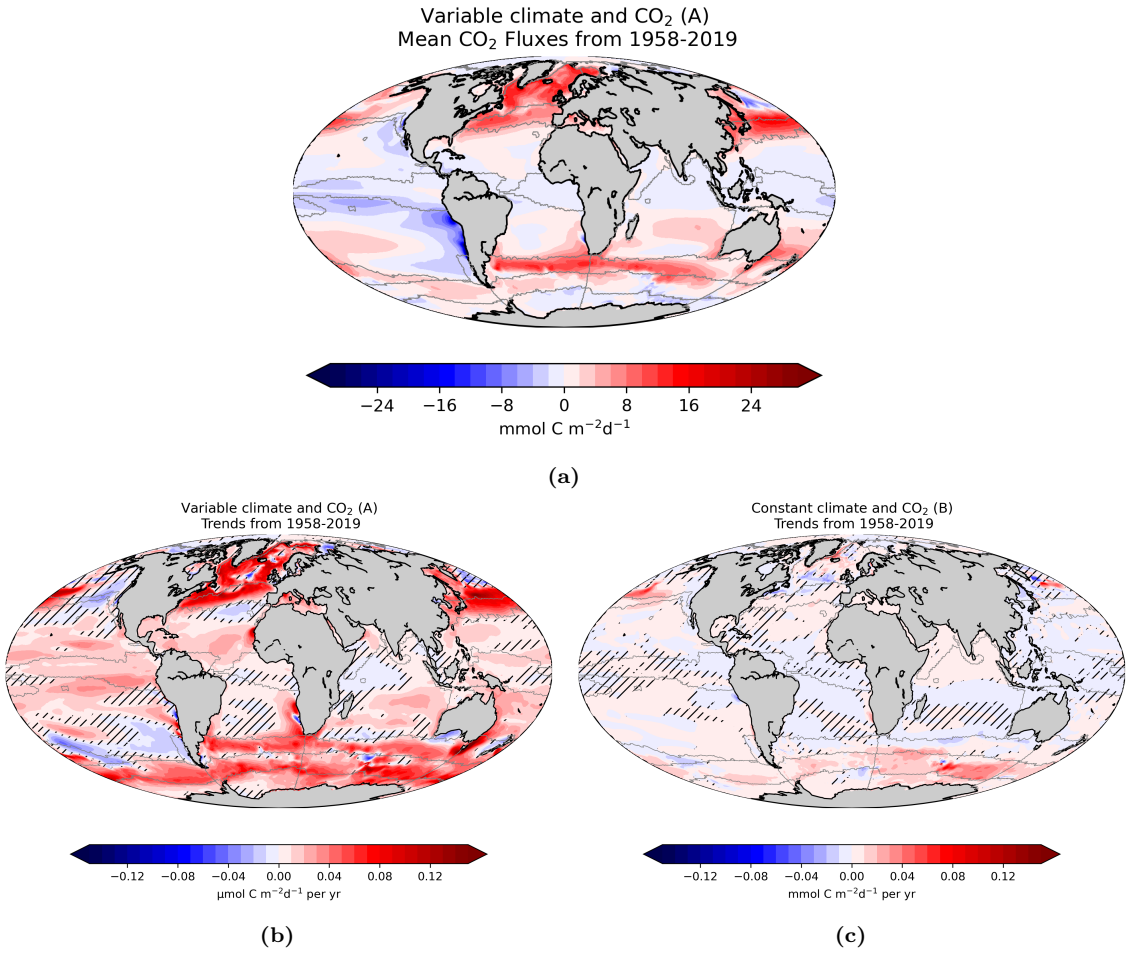

Figure 4.1: (a) Mean CO_2 flux density in sim-A, (b) trend in CO_2 flux in sim-A and trend in CO_2 flux in sim-B. Positive indicates a flux into the ocean. Hatched areas indicate low significance of trends (p-values greater than 0.05.)

Chilean coastal upwelling system. In contrast, in sim-A, the STPS is in the process of shifting from a source to a sink of carbon. The EQU biome makes an important contribution to the global outgassing in sim-B as well as in sim-A despite the low CO_2 flux densities there. The ICE biomes also make important contributions to the outgassing in sim-B, whereas the ICE biome is unimportant in sim-A. In sim-B, the STSS accounts for almost half of the global CO_2 flux directed into the ocean and it is equally important in sim-A. In sim-B, the North Atlantic SPSS is responsible for 21% of the global carbon uptake despite its small size, whereas the integrated flux in the Southern Ocean SPSS is tiny. In sim-A, the North Atlantic SPSS is almost equally important as in sim-B (18%). Furthermore, the Southern Ocean SPSS has turned into a considerable carbon sink as well in sim-A (10%).

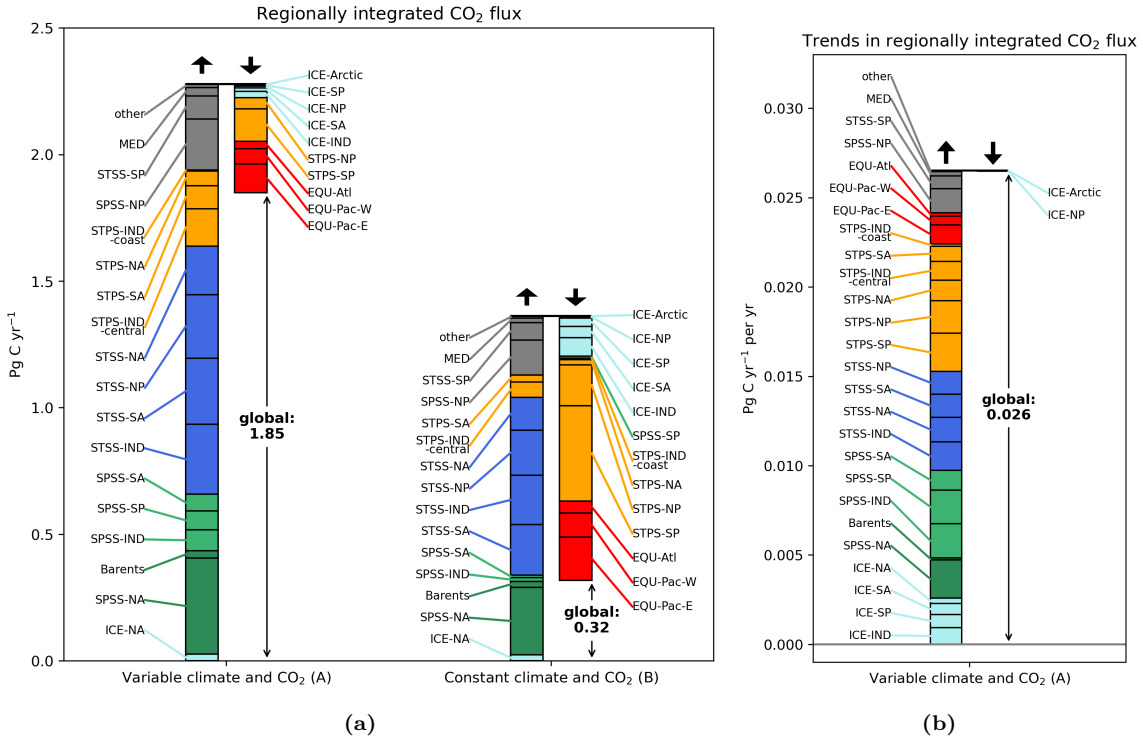

Figure 4.2: Regionally integrated CO_2 flux (a) and trends (b). Positive denotes a flux into the ocean. As some canceling out of positive and negative fluxes happens already on the scale of regional integration, the results shown here depend on the choice of regions.

Table 4.1: Globally integrated CO_2 flux in $\mathrm{Pg\,C\,yr^{-1}}$ and global mean CO_2 flux density in $\mathrm{mmol\,C\,m^{-2}\,d^{-1}}$.

	sim-A	sim-B	sim-C	sim-D	sim-E	sim-F
Globally integrated CO_2 flux	1.85	0.32	1.95	0.23	1.88	1.94
Global mean CO_2 flux density	1.17	0.20	1.23	0.14	1.99	1.22

4.1.2 Temporal variability of the globally integrated CO_2 flux

In the simulation with constant forcing (sim-B), the globally integrated CO_2 flux is stable with a small positive drift of $2.6\,\mathrm{Tg\,C\,yr^{-1}}$ per yr (Figure 4.3, Table 4.2). In the simulation with a variable climate at constant atmospheric CO_2 (sim-D), the CO_2 flux shows climate-induced interannual and decadal variability and a climate-induced secular negative trend, i.e. towards more outgassing, of $-4.3\,\mathrm{Tg\,C\,yr^{-1}}$ per yr. In contrast, the simulation with a steady climate and increasing atmospheric CO_2 concentration (sim-C) features a strong positive trend of $33.0\,\mathrm{Tg\,C\,yr^{-1}}$ per yr, meaning an increase in the sink over time. Moreover, the interannual variability is reduced in this simulation compared to the simulations with a variable climate. In the historical simulation (sim-A), the trend and variability of the CO_2 flux comes from the sum of the drift from sim-B, the climate-induced interannual variability and the climate-induced negative trend in the natural CO_2 flux from sim-D and the positive trend caused by the rise in atmospheric CO_2 concentrations from sim-C. The residual, i.e. the impact of climate on the trend in the anthropogenic CO_2 flux, is small (2%, Table 4.2). This results in a positive trend of $26.5\,\mathrm{Tg\,C\,yr^{-1}}$ per yr in sim-A. As expected, the CO_2 flux in the simulations sim-E and sim-F, in which the temperature and respectively the wind component of the climate variability are missing, lies mostly between the CO_2 flux of sim-C and

Table 4.2: Trend in the globally integrated CO_2 flux in $Tg\,C\,yr^{-1}$ per yr and global mean CO_2 flux density in $\mu mol\,C\,m^{-2}\,d^{-1}$ per yr.

Trend in:	sim-A	sim-B	sim-C	sim-D	sim-E	sim-F
Globally integrated CO_2 flux	26.5	2.7	33.0	-4.5	28.8	29.4
Global mean CO_2 flux density	16.7	1.7	20.8	-2.8	18.2	18.6

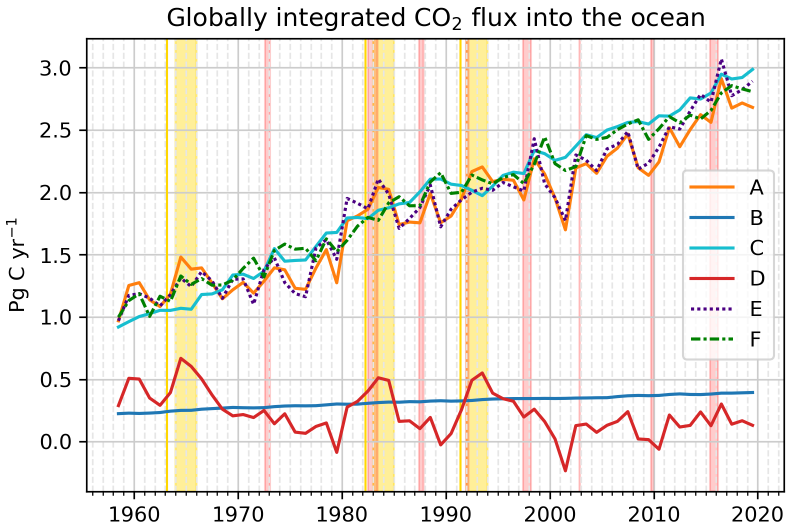

Figure 4.3: Timeseries of globally integrated CO_2 flux in all simulations. The red vertical coloring indicates the timing of strong El-Niño events (ONI 1.5) calculated from sim-A. The yellow vertical lines indicate the timing of volcanic eruptions. Furthermore, first and second year following volcanic eruptions are marked with yellow color.

sim-A which have either no or the full climate variability. The interannual variability of the CO_2 flux in sim-F, in which the variability of winds is missing, is small compared to the simulation with full climate (sim-A), whereas the interannual variability of the CO_2 flux in sim-E, in which the variability of the temperature is missing, is mostly similar to sim-A.

4.1.3 Trends in the historical simulation (sim-A)

The trends in the CO_2 flux in the historical simulation (sim-A) are mostly positive, i.e. towards more oceanic uptake of carbon (Figure 4.1b) with a global mean $16.7\,\mu mol\,C\,m^{-2}\,d^{-1}$ per yr. There are only few and small areas with significant negative trends. On the large scale, there is a correlation between the mean CO_2 flux density and the trend (Figure 3.3b; additionally compare Figure 4.1a with Figure 4.1b). This is valid for the North Atlantic SPSS, which features the highest CO_2 flux densities into the ocean and the largest trends ($\sim$0.05 $mmol\,C\,m^{-2}\,d^{-1}$ per yr), the STSS which has medium to high CO_2 flux densities and medium to high trends (0.03-0.04 $mmol\,C\,m^{-2}\,d^{-1}$ per yr), and the STPS, which has small positive, negative or transitioning CO_2 flux densities and small positive trends ($\sim$0.01 $mmol\,C\,m^{-2}\,d^{-1}$ per yr). Interestingly, the Southern Ocean SPSS and ICE biome deviate in this respect. In the Southern Ocean SPSS, the trends are high ($\sim$0.03 $mmol\,C\,m^{-2}\,d^{-1}$ per yr, i.e. comparable to the trends in the STSS), whereas the mean CO_2 flux is small. These high trends in the Southern Ocean SPSS are visible as a zonal band of high trends in the CO_2 flux density between 50-70 °S which has no counterpart in the mean CO_2 flux. The band extends also in the ICE biome. Accordingly, also the Southern Ocean ICE regions feature high trends. Given the small mean flux in the Southern Ocean ICE biome, the trend is relatively high compared to the mean flux, e.g.

the ICE-SP transitions from a flux density of around $-1.0\,\mathrm{mmol\,C\,m^{-2}\,d^{-1}}$ at the beginning of the timeseries to about $0.5\,\mathrm{mmol\,C\,m^{-2}\,d^{-1}}$ at the end of the time series. In contrast, the trends in the Northern hemisphere ICE biome are mostly very small apart from the transition zone to the North Atlantic SPSS. The trends in the equatorial biome are similar to those in the subtropics, meaning that the EQU biome has not shifted from CO_2 source to a CO_2 sink yet. Locally, some particularly strong trends are found at coastal spots, such as around Tasmania and at the South Australian coast and at the North West African coast. In the Benguela and Chilean upwelling system, positive and negative trends occur locally nearby, indicating a shift of the circulation.

4.2 Results from offline calculations

4.2.1 Climate-induced trends in the natural CO_2 flux (sim-D)

In order to separate the direct effects of different climate variables on the trend in the natural CO_2 flux, the results from the offline calculations outlined in Section 3.2 based on the simulation with variable climate at constant atmospheric CO_2 (sim-D) are presented in the following sections (Section 4.2.2-Section 4.2.8). In sim-D, the trend in globally integrated air-sea flux is negative, that means towards less carbon uptake, with a mean of $-2.8\,\mu mol\,C\,m^{-2}d^{-1}$ per yr. The trend is regionally heterogeneous (Figure 4.4). Regional trends in the CO_2 flux density are significant in 48% of the global ocean area. 60% of the regionally integrated negative trend in the CO_2 flux stem from the STPS biome mainly due to its size. Areas inside the STPS biome with significant negative trends in the CO_2 flux density are found in the Eastern South Pacific, in the North West Indian Ocean and in the South Atlantic. Besides the STPS biome, the EQU biome, the Indian Ocean sector of the Southern Ocean STSS and the Atlantic sector of the Antarctic ICE biome contribute about equally to the regionally integrated negative trend. Only a small portion of the world's ocean area features significant positive trends in the climate-induced CO_2 flux density. Most important is the transition zone of the North Atlantic STSS and the North Atlantic ICE biome, where almost half of the globally integrated positive trends arise.

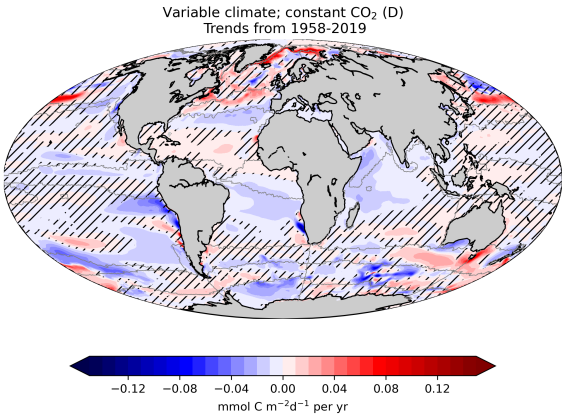

Figure 4.4: Trend in the CO_2 flux in sim-D. Positive indicates a trend towards more flux into the ocean or less outgassing. Hatched areas indicate low significance (p-values greater than 0.05).

4.2.2 Overview of all separable parameters affecting the trend in the global CO_2 flux

The climate-induced trend in the CO_2 flux has components generated by changes in temperature, sAlk, sDIC, winds and salinity plus freshwater fluxes. Globally, the dominant effect is that of the warming sea surface temperatures, which generate an outgassing trend of $-14.9\,Tg\,C\,yr^{-1}$ per yr (Figure 4.5). The temperature effect alone is about 3.5 times larger than the net trend in the CO_2 flux. However, most of the temperature effect is offset by the effects of sAlk ($+8.3\,Tg\,C\,yr^{-1}$ per yr) and sDIC ($+3.6\,Tg\,C\,yr^{-1}$ per yr). The effect of a trend in winds is comparatively small ($+1.0\,Tg\,C\,yr^{-1}$ per yr). The smallest effects are those of changes in salinity plus freshwater fluxes and sea-ice concentration. In this offline calculation, the sum of all the contributions by the different climate parameters explains ~60% of the net trend in the CO_2 flux in sim-D due to the simplifying assumptions that were made. Ideally, it should explain 100% of the trend. While the misfit is small on the global scale (orange arrow in Figure 4.5), it is sometimes much larger regionally.

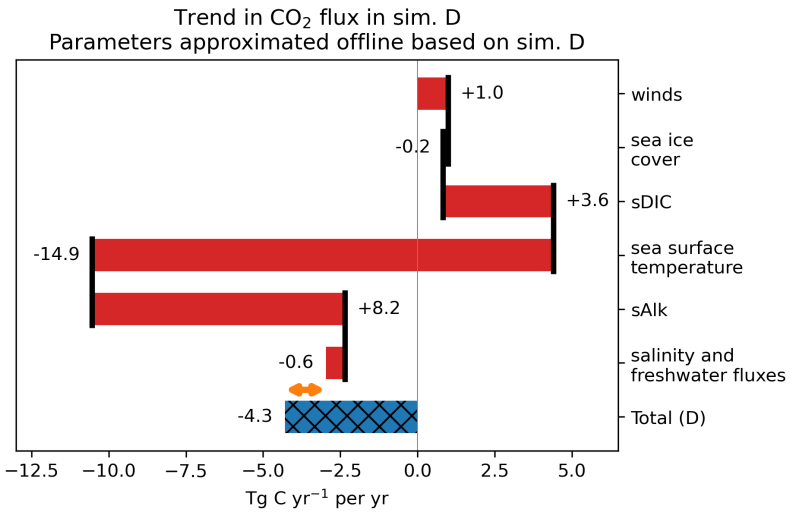

Figure 4.5: The contributions of different climate variables to the trend in the globally integrated CO_2 flux, as they were calculated using the offline approach outlined in Section 3.2 based on the climate-only simulation (sim-D), are shown as red bars. They should ideally sum up to the total trend in the CO_2 flux in sim-D (blue-hashed bar at the bottom). The misfit is indicated by the orange double arrow.

The temperature effect is negative, i.e. causing less CO_2 uptake, in almost all biomes (Figure 4.6a). The magnitude of the regionally integrated trends generated by the temperature effect overall corresponds to the size of the biomes. Thus, the STPS accounts for the largest part. The exceptions to this are the SPSS regions: The northern hemisphere SPSS regions contribute disproportionally much to the global integral relative to their small size. In contrast, the Southern Ocean SPSS is the only biome which experiences a positive, yet small, temperature effect (see Section 4.2.3).

The effect of alkalinity on the global CO_2 flux trend is dominated by the Southern Ocean SPSS (Figure 4.6b). The effect of alkalinity in the Southern Ocean SPSS is to generate a positive trend in the integrated CO_2 flux which is even twice as large as the global net trend in the CO_2 flux. However, the effect of alkalinity in the Southern Ocean SPSS cancels with the opposite effect of sDIC in the same region. This can be understood as a result of processes which alter both alkalinity and sDIC. These processes can either be changes in circulation or changes in biology. Firstly, changes in circulation can alter how much sDIC and alkalinity are upwelled to the surface. Secondly, primary production at the surface reduces sDIC through photosynthesis. Simultaneously, it reduces alkalinity firstly through the consumption of nutrients [1] and additionally the formation of calcium carbonate by some phytoplankton groups [2] (Sarmiento and Gruber, 2006). Nutrients, organic carbon and calcium carbonate are remineralized while they sink to the bottom as biological particles, leading to an increase of nutrients, sDIC and alkalinity with depth. The effect of sDIC and alkalinity on pCO_2^O and thus the CO_2 flux is opposite in sign: pCO_2^O is increases with sDIC and decreases with alkalinity. The effect of sDIC on pCO_2^O is usually dominant (Sarmiento and Gruber, 2006). As shown in (Figure 4.6b), in almost all biomes, the effect of alkalinity on the trend in the CO_2 flux coincides with a reverse effect of sDIC without a fixed ratio, but usually with a larger effect of sDIC. Surprisingly, the impact of sDIC on the globally integrated CO_2 flux is smaller than that of alkalinity. This is a consequence of the regional distribution: The effect of alkalinity on the trend in the globally integrated CO_2 flux is dominated by a positive contribution from the Southern Ocean SPSS ($+9.5\,\mathrm{Tg\,C\,yr^{-1}\,per\,yr}$) which coincides with an about equally strong reverse effect of sDIC. In

[1] nutrient consumption: the alkaline nitrate NO_3^- is consumed (Sarmiento and Gruber, 2006)

[2] formation of calcium carbonate: the alkaline carbonate CO_3^{2-} is bound through the reaction: $Ca^{2+} + CO_3^{2-} \longrightarrow CaCO_3$ (Sarmiento and Gruber, 2006)

contrast, the effect of sDIC has also important contributions from the northern hemisphere SPSS, the STPS in both hemispheres and parts of the STSS biome which generate a positive trend in the global CO_2 flux of $+14.7\,\mathrm{Tg\,C\,yr^{-1}}$ per yr, but only have comparatively weaker counterparts in alkalinity (less than $-6\,\mathrm{Tg\,C\,yr^{-1}}$ per yr in magnitude). In summary, the effect of sDIC on the trend in the CO_2 flux is regionally often stronger and reverses the effect of alkalinity. However, because of regional canceling out, the impact of sDIC on the trend in the globally integrated CO_2 flux is weaker than the impact of alkalinity. Globally, both parameters generate a trend towards more uptake of CO_2.

Finally, the least important drivers of the trend in the CO_2 flux are winds, salinity plus freshwater fluxes and sea-ice concentration (Figure 4.6c). The effect of winds is towards more uptake of CO_2 and stems from biomes widely scattered on the globe. The effect of salinity and freshwater fluxes on the trend in the CO_2 flux is towards more outgassing and mostly present in the ICE biome and adjacent regions. As expected, the effect of sea-ice concentration is also limited to this area.

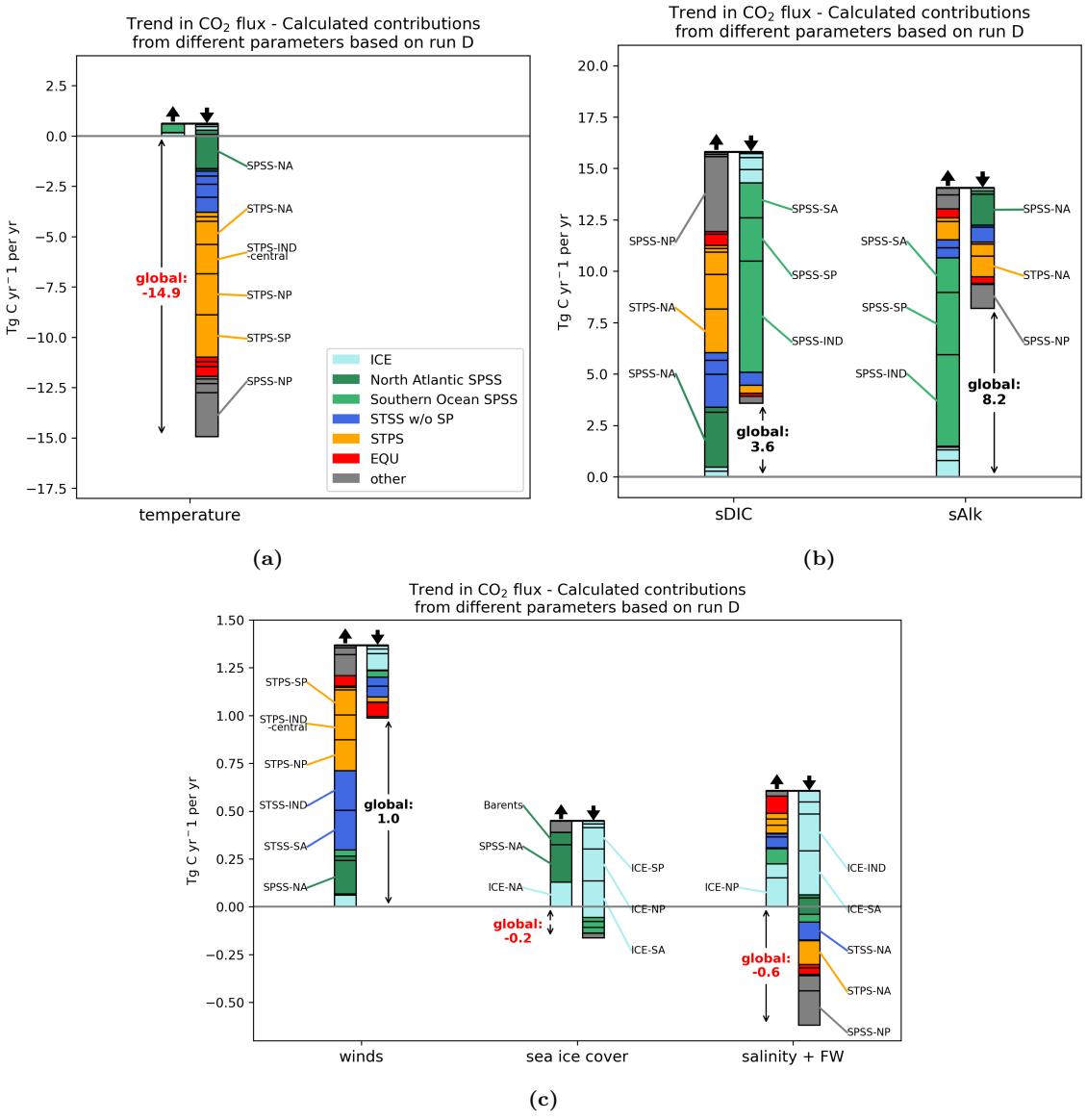

Figure 4.6: Contributions by region to the spatially integrated trend in the CO_2 flux in sim-D caused (a) by temperature, (b) by sDIC and by sAlk and (c) by winds, by sea-ice concentration and by salinity and freshwater fluxes (FW). Positive denotes a trend towards more flux directed into the ocean or less outgassing. Note the differences in y-axis scaling.

4.2.3 Temperature

The trend in the global mean sea surface temperature is a warming of 7.1×10^{-2} °C per decade caused by anthropogenic climate change. This warming is found in most regions and is mostly significant (Figure 4.7b) and only small regions show significant cooling, namely in the North Atlantic Subpolar Gyre and in the Southern Ocean SPSS. While the cooling is attributed to changes in the circulation related to freshening in the former region (Rahmstorf et al., 2015), the cooling in the latter is attributed to the advection of cold air from Antarctica, wind-driven changes in the circulation or sea-ice (Haumann et al., 2020). The highest positive temperature trends occur at high latitudes in the northern hemisphere. Due to the general warming, the temperature-related trends in the CO_2 flux density are negative almost everywhere, i.e. towards less carbon uptake or more outgassing (Figure 4.7c) with a global mean trend of $-9.3\,\mu\text{mol}\,\text{C}\,\text{m}^{-2}\text{d}^{-1}$ per yr. This is because the solubility of CO_2 in seawater decreases during warming, so that pCO_2^O increases (Equation (3.27)) and with that ΔpCO_2 becomes more negative. The impact of changing temperatures on the CO_2 flux density is largest in the subpolar regions. Firstly and most importantly, this might be because in the subpolar regions, any temperature-driven change of ΔpCO_2 is translated into big changes of the CO_2 flux (Equation (3.30)) because the mean gas transfer coefficient ($\alpha \cdot k_w$, Figure S5) is highest there due to the high mean wind velocities and cold mean temperatures. Secondly, the solubility (α) is a nonlinear function of temperature and $\frac{\partial \alpha}{\partial T}$ has the highest absolute values at cold temperatures (Equation (3.26)), so that the reduction of the gas transfer coefficient ($\alpha \cdot k_w$) caused by increasing temperatures is greater where the mean temperature is low, which is at high latitudes. However, the temperature-driven reduction of the gas transfer coefficient has only a very small impact on the trend in the CO_2 flux (five magnitudes smaller than the impact of the temperature-driven increase of pCO_2^O). The third effect, which is that the sensitivity of pCO_2^O to temperature is larger at higher pCO_2^O (Equation (3.27)), i.e. in the tropical East Pacific and the EQU biome, would favor another regional pattern and does not have a visible impact.

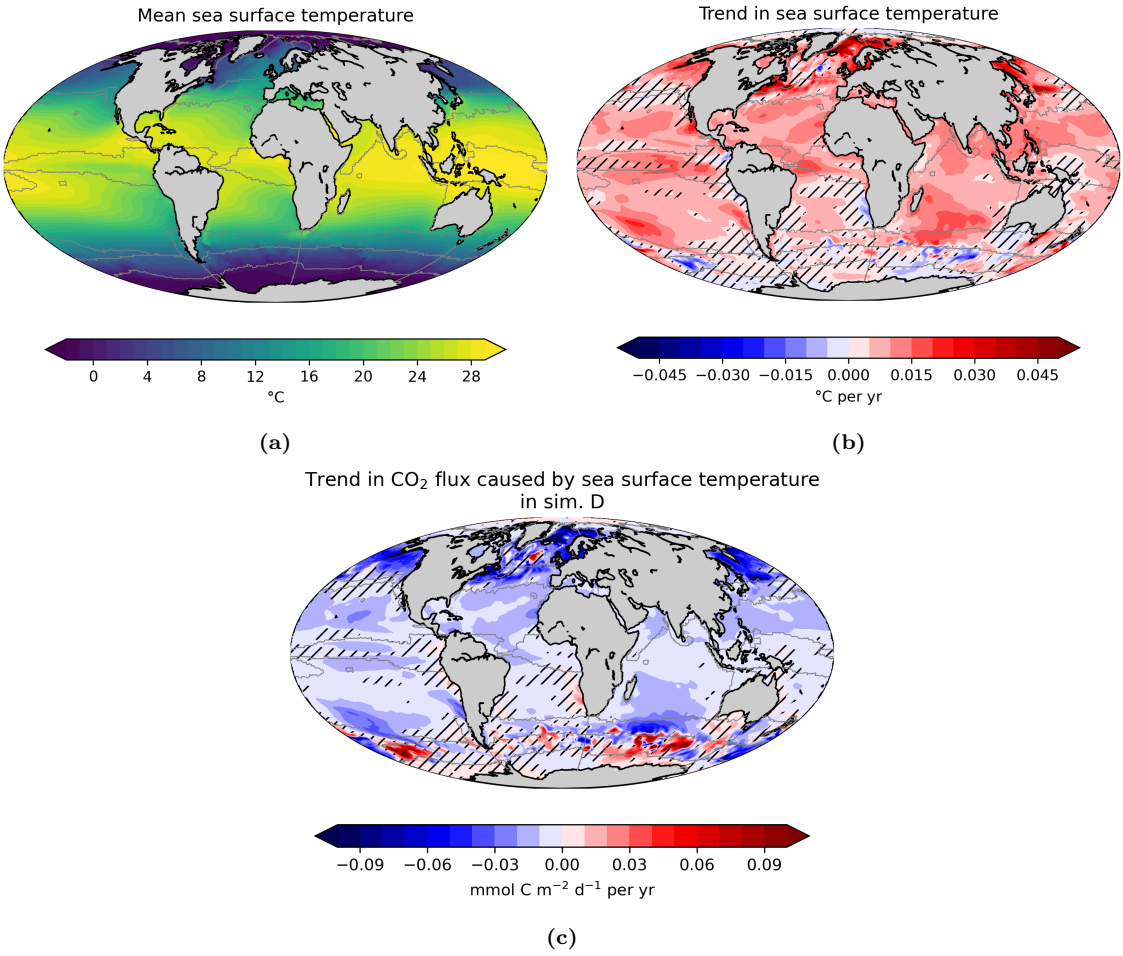

Figure 4.7: (a) Mean and (b) trend in the sea surface temperature and (c) the trend in the CO_2 flux density that is expected from the trend in sea surface temperature, where positive denotes a trend towards more uptake. Hatched areas indicate low significance (p-values greater than 0.05).

4.2.4 Winds

The squared wind velocity is an indicator for storminess. It is largest in the subpolar westerly wind zones (Figure 4.8a). The trends in the squared wind velocities show a distinct regional pattern with areas of positive and negative trends and areas without significant trends (Figure 4.8b). Stronger winds generally increase the gas transfer velocitity (k_w), so that depending on the local pCO_2 gradient, the effect on the CO_2 flux can either be positive or negative (Equation (3.22)). The global mean effect of changing winds is positive, i.e. towards more CO_2 flux into the ocean ($0.6\,\mu mol\,C\,m^{-2}d^{-1}$ per yr, Figure 4.5).

The most striking feature in the wind product used to force the model simulation are the increasing velocities of westerly winds over the Southern Ocean SPSS (Figure 4.8b), a phenomenon that is caused by Antarctic stratospheric ozone depletion and greenhouse gases (Thompson et al., 2011; IPCC, 2013a,b). However, the natural ΔpCO_2 is mostly small in the Southern Ocean SPSS so that the effect on the CO_2 flux density (Equation (3.22)) is mostly small there (Figure 4.8c). The pCO_2 gradients are greater in the adjacent STSS and ICE regions, so that the increasing Westerlies lead to more CO_2 uptake in the Southern Ocean STSS and, in contrast, more outgassing in the southern

hemisphere ICE regions.

The trend in squared winds comes in regional patches. These regions are often, but not always corresponding to zonal bands. Starting from the south, there is the above-mentioned zonal strengthening of Westerlies between 40-60 °S. Secondly, in parts of the subtropics in the southern hemisphere, the squared winds increase (e.g. South East Atlantic and South East Pacific). Thirdly, in parts of the subtropics in the northern hemisphere, the squared winds decrease. Finally, in the northern high latitudes, the squared winds show rather positive, but insignificant trends. Concerning the trend in the CO_2 flux density, there is a tendency that wind-related trends in the CO_2 flux density occur rather near the coast than in the open ocean, with the highest impact related to upwelling systems (e.g. positive and negative trends off the west coast of South America and around the African Cape). However, there are also regions with high wind-induced trends in the CO_2 flux in the open ocean (e.g. in the South Atlantic STSS). Some changes occur rather at the edges of the biomes that are used here (e.g. North Brazil current), possibly related to fronts.

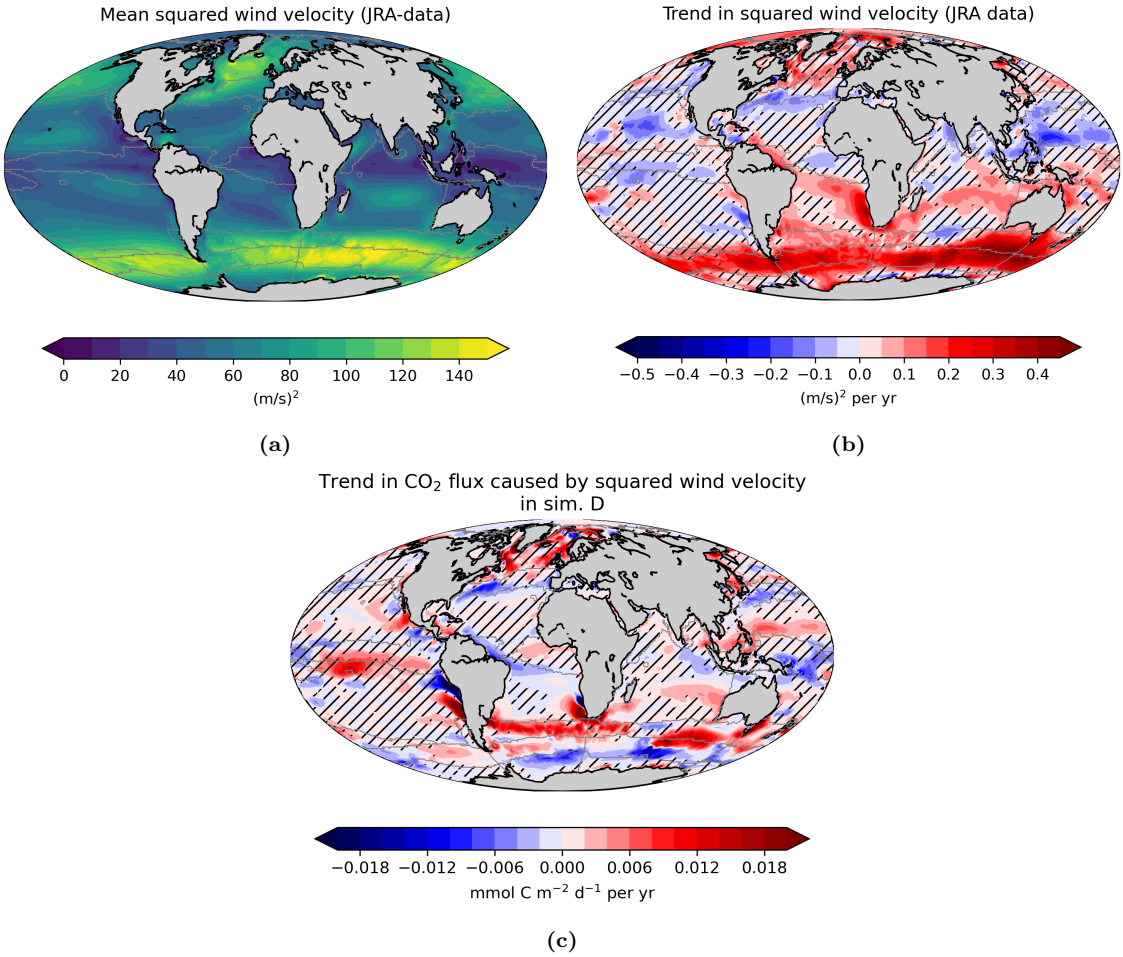

Figure 4.8: (a) Mean and (b) trend in the squared wind velocity and (c) the trend in the CO_2 flux density that is expected from the trend in squared wind velocity, where positive denotes a trend towards more uptake. Hatched areas indicate low significance (p-values greater than 0.05). The wind data used to force the model simulation stems from the JRA-55 reanalysis dataset (JMA, 2021).

4.2.5 Sea-ice concentration

Arctic

The extent of the Arctic sea-ice has decreased (Figure 4.9b). Thus, negative trends in sea-ice concentration up to -1% of the grid cell area per year occur at the Arctic sea-ice edge. Where the ICE biome transitions into the North Atlantic and North Pacific SPSS, which are biologically productive regions (Figure S14a) with a high air-sea gradient of CO_2 partial pressures, the retreating ice cover leads to more uptake of CO_2 because a larger ocean surface area is exposed to the atmosphere (Figure 4.9c). Sea-ice cover in the SPSS occurs only during the months of greatest ice extent, i.e. around March, so that the ice-related change in the CO_2 flux in the SPSS regions is limited to these months. In contrast, the trends inside the ICE biome occur during the months of furthest ice retreat, i.e. around October (seasonality not shown). Along the Arctic coast off Russia and Alaska, the reduction of sea-ice concentration leads to more outgassing. Here, the model simulation produces extremely high pCO_2^O below the sea ice, which might not be realistic. While the effect of trends in the sea-ice concentration on the trend in the CO_2 flux density can locally be high (more than $0.1\,\mathrm{mmol\,C\,m^{-2}d^{-1}}$ per year, i.e. of the same magnitude as the temperature effect), its effect on the global trend in the CO_2 flux density is small ($-0.1\,\mathrm{\mu mol\,C\,m^{-2}d^{-1}}$ per year, Figure 4.6).

Antarctic

Overall, the sea-ice concentration in the Antarctic is declining (Figure 4.9e). But in contrast to the Arctic, there is a small increase in the modelled sea-ice concentration in the Antarctic in a few places near the coast, namely in the Ross Sea and along the coast of East Antarctica. Trends in sea-ice concentration are negative along the edge of maximum Antarctic sea-ice extent and in a broad region in the Atlantic sector of the Southern Ocean ICE biome, but the decrease of sea-ice concentration here, which is up to -0.5% of the grid cell area per year, is not as pronounced as in the Arctic. The Antarctic ICE biome is a region of weak outgassing, so that with the reduction of sea-ice concentration, the outgassing increases (Figure 4.9f). Overall, the ice-related trends in the CO_2 flux density in the Antarctic (up to $0.05\,\mathrm{mmol\,C\,m^{-2}d^{-1}}$ per yr) are smaller than in the Arctic.

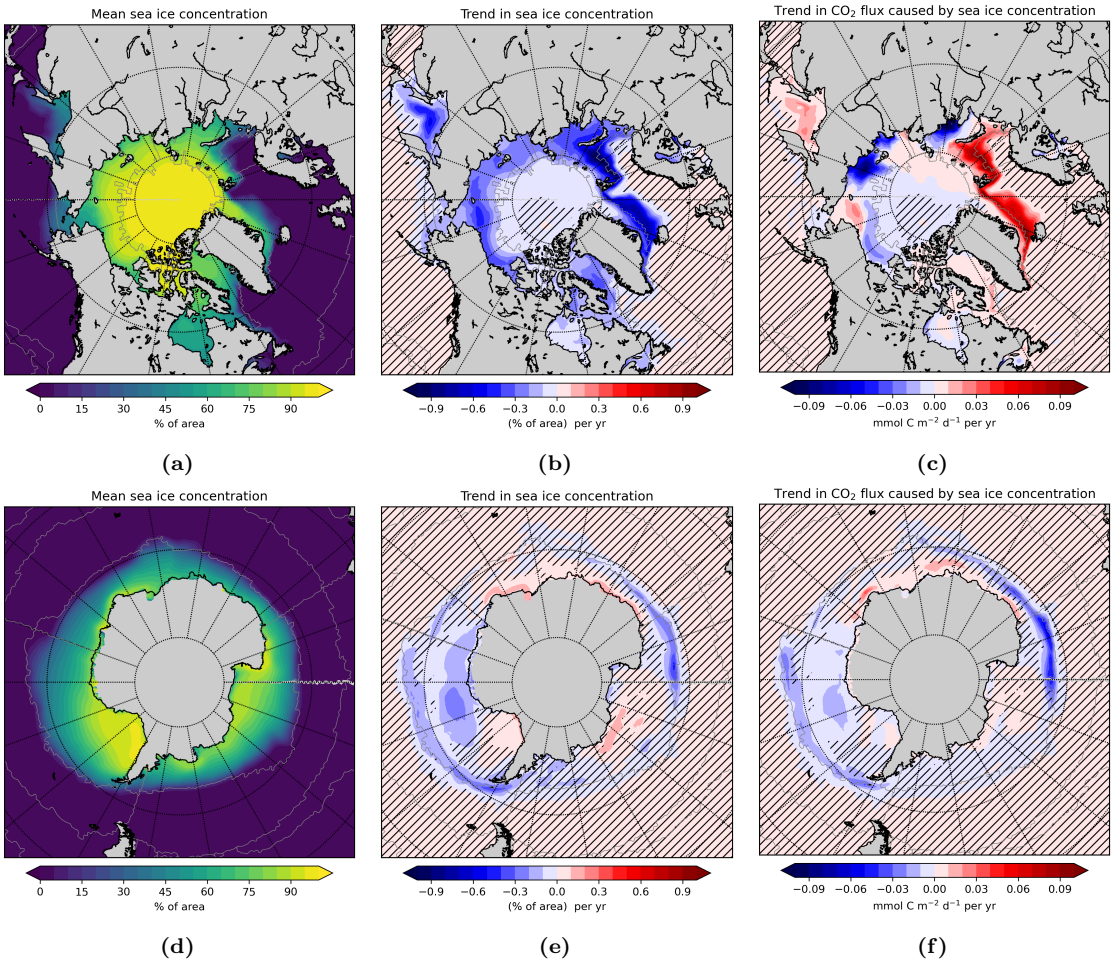

Figure 4.9: (a) Mean and (b) trend in the sea-ice concentration and (c) the trend in the CO_2 flux density that is expected from the trend in sea-ice concentration, where positive denotes a trend towards more uptake. Hatched areas indicate low significance (p-values greater than 0.05).

4.2.6 Salinity and freshwater fluxes

The salinity of the surface ocean is to large extent determined by freshwater fluxes (Sarmiento and Gruber, 2006). As it is shown in Figure 4.10b, 47% of the ocean's area features significant trends in salinity despite a weak surface salinity restoring in the model and climatological river runoff forcing. The trends are organized in regional patches without a clear global pattern. In general, freshening leads to positive trends in the CO_2 flux, i.e. trends towards more CO_2 uptake or less outgassing, and salinification causes negative trends, i.e. trends towards less CO_2 uptake or more outgassing. This is firstly because the removal of freshwater increases DIC and thus pCO_2^O; secondly, pCO_2^O increases with salinity; and thirdly and in contrast to the others, the removal of freshwater increases alkalinity and thus reduces pCO_2^O, but this effect is weaker (Sarmiento and Gruber, 2006).

Because the buffer factor for DIC (γ_{DIC}) is largest at high latitudes, freshwater related changes in DIC have the largest impact there. The mean salinity in the ICE biome in both hemispheres is low (Figure 4.10a), but significant trends in salinity are found there, possibly related to changes in sea-ice formation and transport. Consequently, the strongest salinity-related trends in the CO_2 flux occur at the ice edge (Figure 4.10c). However, it is regionally different whether this leads to a positive or

negative change in the CO_2 flux depending on the local prevalence of freshening or salinification.

Regarding the northern hemisphere, the trends in salinity are particularly strong (up to $\pm 1.5 \times 10^{-2}$ psu per year). However, there is no large-scale coherent salinity-related trend in the CO_2 flux. In the ICE biome, there are strong positive as well as negative trends in the CO_2 flux related to freshening and salinification, but with plenty of sub-biome-scale differences. Further away from the pole in the subpolar zone, negative trends in the CO_2 flux occur in association with salinification of the North Atlantic Current and North Pacific Current.

In the southern hemisphere, the ICE biome mostly experiences a relatively weak salinification. This leads to a negative trend in the CO_2 flux (i.e. more outgassing) and this area accounts for about 40% of the globally integrated negative trends in the CO_2 flux related to changes in salinity (see Figure 4.6c.) Further away from the pole in the subpolar zone, there are some positive trends in the CO_2 flux density related to freshening.

Trends in salinity in the tropics and subtropics have little impact on the CO_2 flux density. As for all parameters that act on pCO_2^O - which are the temperature, salinity and freshwater fluxes, alkalinity and DIC -, the potential effect on the CO_2 flux is limited by the mean gas transfer coefficient ($\alpha \cdot k_w$), which is small in the tropics and subtropics. A large area of coherent freshening is found in the tropical Indo-Pacific, possibly related to changes in the monsoon. In the tropical and subtropical Atlantic, some areas (off the West African coast and North Brazil coast) experience salinification, whereas a freshening occurs close to the Gulf of Guinea. When biome-wise integration is applied (Figure 4.6), the effect of these trends in salinity on the trend in the integrated CO_2 flux mostly cancels out.

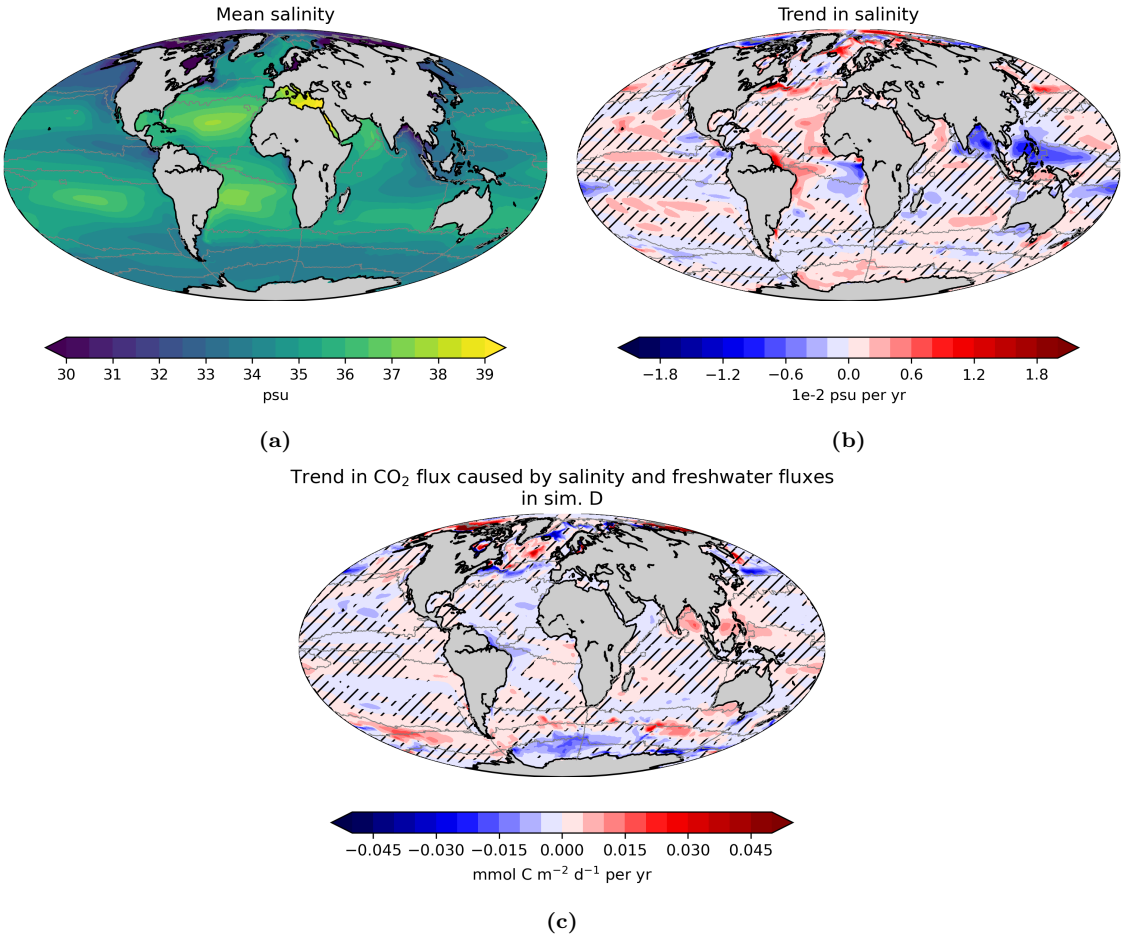

Figure 4.10: (a) Mean and (b) trend in the salinity and (c) the trend in the CO_2 flux density that is expected from the trend in salinity and fresh-water fluxes, where positive denotes a trend towards more uptake. Hatched areas indicate low significance (p-values greater than 0.05).

4.2.7 Salinity-normalized alkalinity

The geographical distribution of the mean alkalinity remains the same after salinity-normalization (Figure 4.11a). This is because in this thesis, sAlk is obtained by normalization with the local mean salinity at every location (not by a globally uniform value). Normalization by the local mean salinity is done in order to remove the effect of *temporal* variability in freshwater fluxes on the alkalinity, but it does not remove the effect of the *regional* variability in freshwater fluxes. Since the surface ocean alkalinity is mostly determined by freshwater fluxes (Sarmiento and Gruber, 2006), the regional distribution of alkalinity resembles that of the salinity (compare Figure 4.11a and Figure 4.10a). The exception to this is the Southern Ocean, where sAlk is high and salinity is low.

In contrast to that, trends in sAlk have almost the same geographical distribution as the trends in salinity, but with an opposite sign (compare Figure 4.11b and Figure 4.10b). On the one hand, this could indicate that along with changes in salinity, changes in other processes occur that alter sAlk. Among them, the model employs a restoring for alkalinity analogously to salinity. On the other hand and which I find more plausible, the effect of salinity-normalization possibly weighs too heavy on the trend in sAlk. Without salinity-normalization, a positive trend in salinity should generate a proportional positive trend in alkalinity due to the effect of freshwater. The aim of

salinity-normalization is conceptually that this freshwater-induced trend is removed in sAlk. But the results show that instead of just removing the trend, an apparently spurious opposite-signed trend in sAlk arises. This can happen if a trend in the salinity is not due to changes in freshwater fluxes, but due to other processes such as changes in circulation. In this case, the salinity is not a correct tracer of changes in freshwater fluxes.

However, there is one striking area where the trends in sAlk are apparently real, i.e. where they occur independently from the trends in salinity, namely in the Southern Ocean SPSS. Here, the trends in the CO_2 flux density related to changes of alkalinity are more coherent than in other parts of the ocean (Figure 4.11c) and are locally up to $0.2\,\mathrm{mmol\,C\,m^{-2}d^{-1}}$ per yr high. This might be related to enhanced upwelling of sAlk-rich waters in the Southern Ocean as a consequence of strengthening westerly winds in the last decades. The trends in the Southern Ocean SPSS amount to a trend in the regionally integrated CO_2 flux towards more uptake of $9.1\,\mathrm{Tg\,C\,yr^{-1}}$ per yr, which means that they have a globally important impact (Figure 4.6b).

The alkalinity-related trends in the CO_2 flux density in other areas of the world cancel largely out in the global mean ($5.1\,\mu\mathrm{mol\,C\,m^{-2}d^{-1}}$ per yr). Locally, some particularly strong negative alkalinity-related trends in the CO_2 flux density occur in the northern hemisphere subpolar areas, but as they are regionally anti-correlated with trends in the salinity, they appear to be mostly spurious effects of the salinity-normalization.

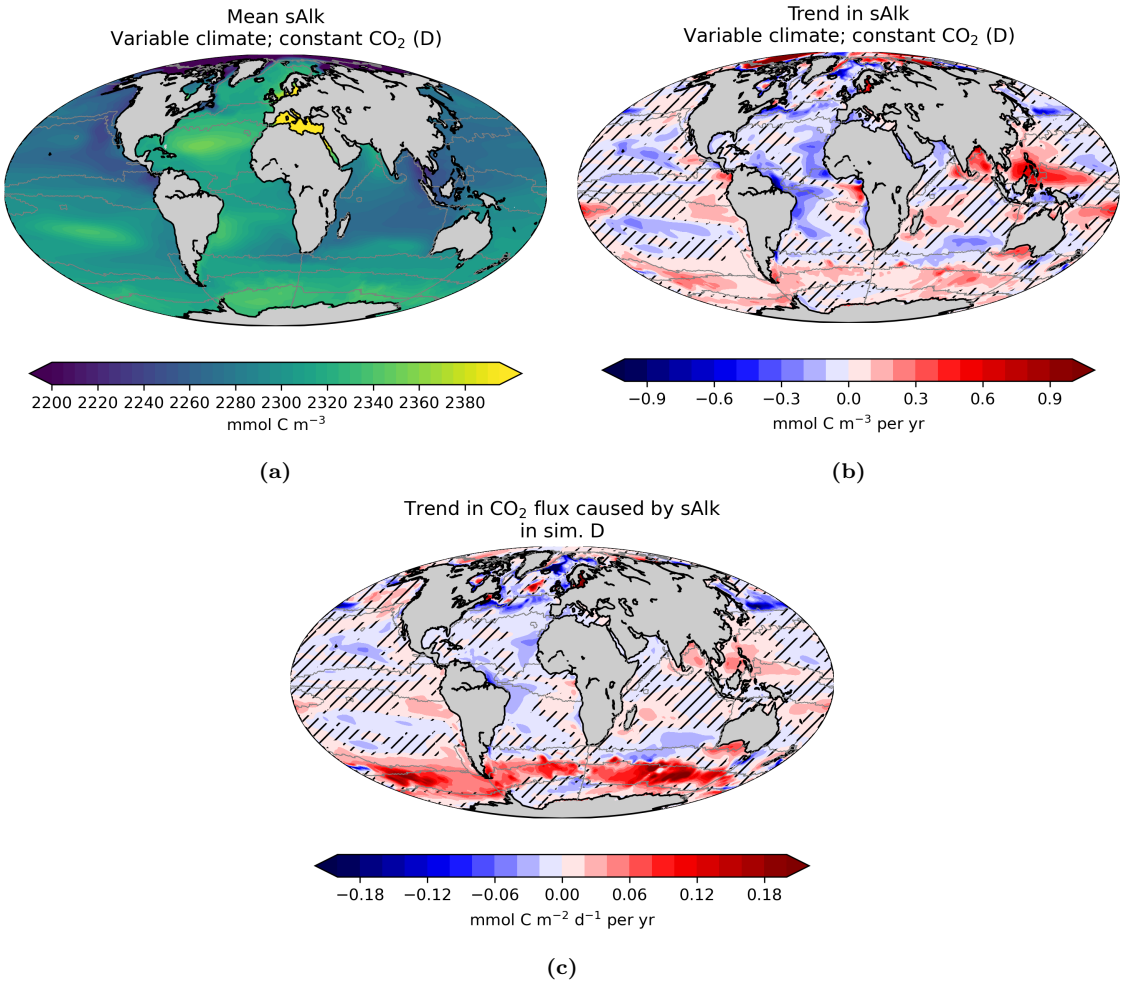

Figure 4.11: (a) Mean and (b) trend in sAlk and (c) the trend in the CO_2 flux density that is expected from the trend in sAlk, where positive denotes a trend towards more uptake. Hatched areas indicate low significance (p-values greater than 0.05).

4.2.8 sDIC

The mean sDIC concentration is largest in cold waters and in upwelling systems (Figure 4.12a). In the same manner as for sAlk (see Section 4.2.7), the trends in sDIC appear to be widely spurious effects of the salinity-normalization (Figure 4.12b compare to Figure 4.10b). However, in the southern hemisphere SPSS and ICE biomes, positive trends in sDIC emerge independently of trends in the salinity. Here, the trends in sDIC lead to more outgassing of $-10.6\,\mathrm{Tg\,C\,yr^{-1}}$ per yr. The increasing sDIC concentrations in the Southern Ocean SPSS are a consequence of enhanced upwelling driven by the strengthening of westerly winds (Hauck et al., 2013b). Furthermore, trends in sDIC that occur independently from the trends in salinity are found in the North Atlantic STPS and Western North Pacific STPS biomes, but there, they only generate a comparatively weak trend in the CO_2 flux density towards more carbon uptake per surface area (Figure 4.12c).

The sDIC-induced trends in the regional CO_2 flux density correlate with those that are induced by sAlk, but with an opposite sign (correlation coefficient of r=-0.89, compare Figure 4.12c and Figure 4.11c). For most of the global ocean, sDIC-induced trends in the CO_2 flux density are between equal and 1.5 times stronger in magnitude than the sAlk-induced trends (Figure 4.13). In particular where changes in sDIC drive positive trends in the CO_2 flux density, i.e towards more oceanic uptake, the effect of sDIC is for the most part between equal and 2 times stronger than the opposite sAlk-induced trends (Figure 4.13). This includes the northern hemisphere SPSS and the North Atlantic STSS, where sDIC-induced trends towards more oceanic uptake surpass $+0.2\,\mathrm{mmol\,C\,m^{-2}d^{-1}}$ per yr in some places (Figure 4.12c). Furthermore, this includes large areas with weak positive sDIC-driven trends up to approximately $+0.1\,\mathrm{mmol\,C\,m^{-2}d^{-1}}$ in the tropical and subtropical Atlantic and the Pacific STPS biome (Figure 4.12c). However, there are also regions where the correlation does not hold. In some parts of the Southern Ocean SPSS, changes in sDIC drive negative trends in the CO_2 flux of up to $-0.1\,\mathrm{mmol\,C\,m^{-2}d^{-1}}$ per yr, while the reverse impact of sAlk is stronger in magnitude than that (Figure 4.13). In other parts of the Southern Ocean SPSS, positive sDIC-driven trends in the CO_2 flux of up to $0.1\,\mathrm{mmol\,C\,m^{-2}d^{-1}}$ per yr even co-occur with positive sAlk-driven trends.

In summary, the sDIC-induced trends in the CO_2 flux are regionally often stronger than the sAlk-induced trends and anti-correlated with them. However, the differences in regional distribution result in more global canceling out of sDIC-related trends than of sAlk-related trends (Figure 4.6b). Consequently, the impact of changes in sDIC on the global trend in the CO_2 flux ($2.2\,\mathrm{\mu mol\,C\,m^{-2}d^{-1}}$ per yr) is smaller than the impact of changes in sAlk (Figure 4.6). On the global scale, both parameters drive a trend towards more oceanic CO_2 uptake. For a more reliable quantification of the sDIC- and sAlk-induced trends in the CO_2 flux and to understand if and how they are associated with each other, a more reliable method to separate the impact of the freshwater fluxes on both parameters is required. The method used here apparently leads to spurious trends in sDIC and sAlk.

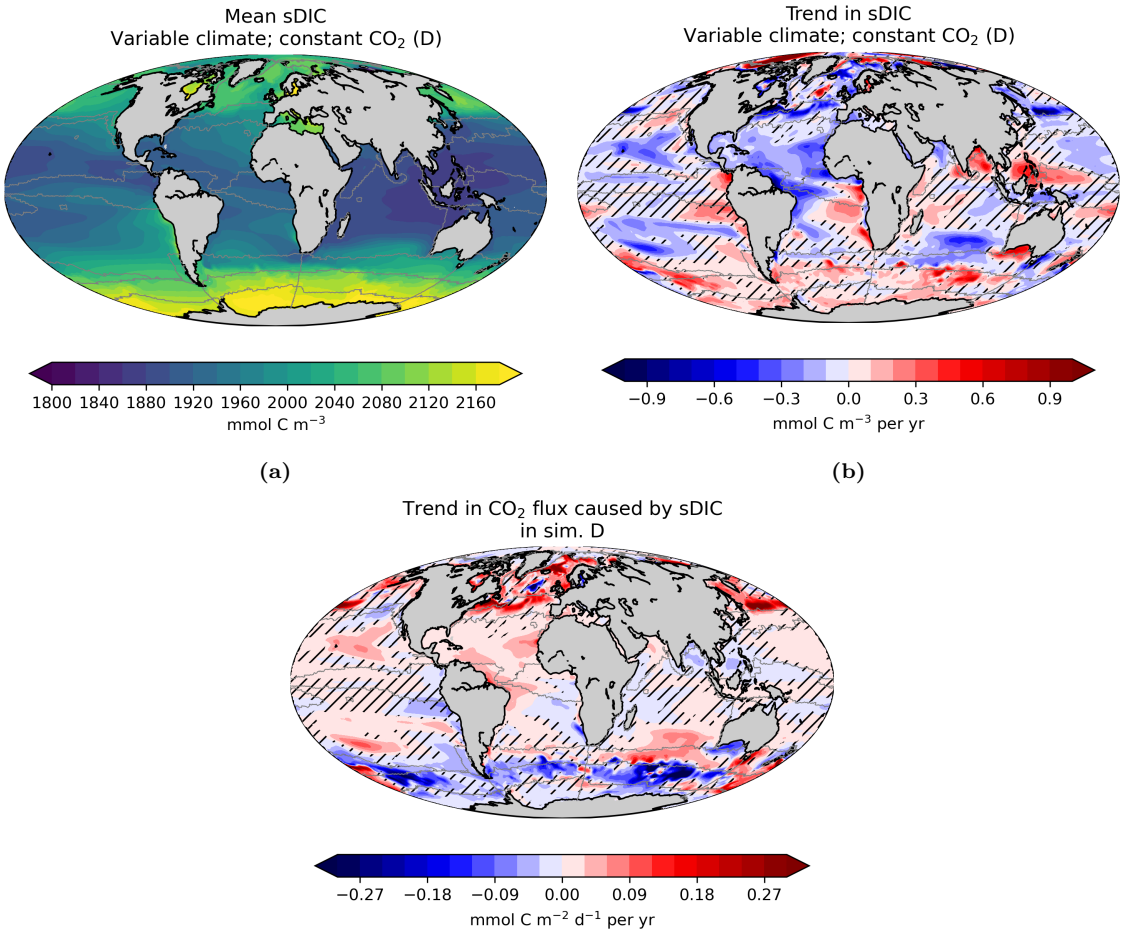

Figure 4.12: (a) Mean and (b) trend in sDIC and (c) the trend in the CO_2 flux density that is expected from the trend in sDIC, where positive denotes a trend towards more uptake. Hatched areas indicate low significance (p-values greater than 0.05).

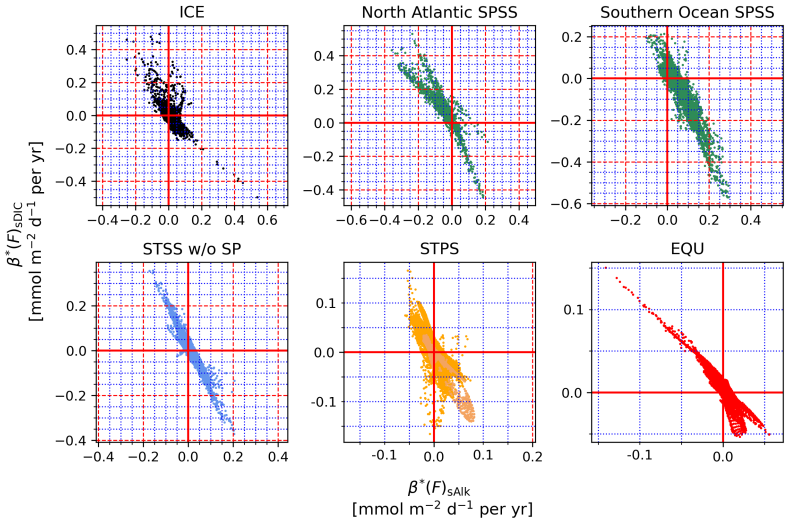

Figure 4.13: Trends in the CO_2 flux density induced by trends in sDIC (y-axis) versus those induced by sAlk (x-axis). Each dot represents an area of ~8×10^6 km^2.

4.2.9 Climate-induced trends in the historical and anthropogenic carbon flux

So far, only the results for the natural carbon cycle simulated in sim-D were shown. For all of the parameters discussed so far apart from sDIC, the impact on the historical CO_2 flux is also known (Table 4.3). For this, sim-A, which reproduces the historical carbon cycle, is assessed. The effects of climate on the anthropogenic flux are derived as the difference between the effects on the historical and the natural CO_2 flux. The effects of temperature and alkalinity on the trend in the globally integrated flux of natural and anthropogenic CO_2 are coherent, with a greater effect on the flux of natural CO_2. This is plausible because the natural pCO_2^O is larger than the anthropogenic pCO_2^O. Because the sensitivity of pCO_2^O to changes in temperature and alkalinity is proportional to the ambient pCO_2^O (Equations (3.27) and (3.40)), changes in temperature and alkalinity have a larger impact on the natural CO_2 flux. In the historical simulation, in which pCO_2^O is about $\frac{1}{6}$ higher than in the simulation with exclusively natural CO_2, the effect of temperature and alkalinity on the trend in CO_2 flux is therefore enhanced.

The effect of winds is similar for the natural and the anthropogenic component of the global mean CO_2 flux (Table 4.3), but this is regionally not uniform (not shown here). Consequentially, the effect of winds on the trend in the historical global CO_2 flux is about doubled compared to the effect on the natural global CO_2 flux. The effect of decreasing sea-ice concentration is towards more outgassing of natural carbon and towards more uptake of anthropogenic carbon, which partly cancels out and results in a small positive net effect in the historical simulation. Surprisingly, the effect of variable salinity and freshwater fluxes is larger on the anthropogenic CO_2 flux than on the natural one. This difference is mainly a result of processes in the Southern Ocean, where salinity and freshwater fluxes cause large negative trends in the natural and in the anthropogenic CO_2 flux, i.e. less uptake of natural and anthropogenic carbon, along an irregular zonal band in the ICE and SPSS biome (natural CO_2 flux shown in Figure 4.10c and historical CO_2 flux shown in Figure S6). The effect of salinification in the Antarctic biomes on the anthropogenic CO_2 flux is possibly enhanced because γ_{DIC}, which is one of the factors determining the sensitivity of pCO_2^O to freshwater fluxes, is higher in sim-A as a consequence of the anthropogenic CO_2 uptake.

Table 4.3: Estimates (in $\mathrm{Tg\,C\,yr^{-1}}$ per year) for the trend in globally integrated natural, anthropogenic and historical CO_2 flux caused by different climate variables. The climate-induced trend in sDIC in sim-A is unknown because it is unclear how much of the variability of sDIC in sim-A is climate-induced and how much stems from the atmospheric CO_2 variability. Note that sim-A and sim-D include a model drift, whereas the difference of both, i.e. the anthropogenic component, does not.

	net	winds	sea-ice	temperature	sAlk	salinity + FW	sDIC
Historical (sim-A)	**(-3.8)**[3]	2.1	0.02	-18.7	11.7	-5.3	
Natural (sim-D)	**-4.5**	1.0	-0.16	-14.9	8.2	-0.6	3.6
Anthropogenic	**(0.7)**[4]	1.1	0.18	-3.8	3.5	-4.7	

4.2.10 Attributing the trend in sDIC concentrations to changes in biology and circulation

4.2.10.1 Mean effect of biology and ocean circulation on surface sDIC concentrations

Changes in sDIC can be a result of the variability in air-sea carbon exchange, biology or circulation. Here, it is assumed that the sDIC concentration is uniform and remains at surface values throughout the mixed layer (see Section 3.2.7). The regional distribution of the mean change rates of sDIC (J_{surf}, J_{bio} and J_{circ}) due to the air-sea CO_2 flux, export production and ocean circulation is very similar in all simulations (Figure 4.14 for sim-A and Figures S7 to S9 for the other simulations). To avoid redundancies, only the mean state in the historical simulation (sim-A) is described in the next paragraphs and differences to sim-D are pointed out where necessary.

Both regionally and globally averaged, J_{surf}, J_{bio} and J_{circ} are nearly balancing each other, implying only little change in the sDIC concentration over the simulated period Figure 4.14. Yet, the individual components (J_{surf}, J_{bio} and J_{circ}) are high, implying a high turnover rate of sDIC. Assuming typical values for sim-A, i.e. a sDIC concentration of $2000\,\mathrm{mmol\,C\,m^{-3}}$ and change rates of $J_{circ} = -J_{bio} = 75\,\mu\mathrm{mol\,C\,m^{-3}d^{-1}}$ and $J_{surf} = 0$ for simplicity, it takes about 70 years for the mixed layer sDIC to be renewed. In upwelling systems with a shallow mixed layer, typical values are as high as $J_{circ} = -J_{bio} = 500\,\mu\mathrm{mol\,C\,m^{-3}d^{-1}}$, so that the timescale for a renewal of mixed layer sDIC is only one decade. In contrast, it would take 3 millennia to add the same amount of carbon, i.e. $2000\,\mathrm{mmol\,C\,m^{-3}}$ of additional sDIC at the rate of the historical trend, which is $0.75\,\mathrm{mmol\,C\,m^{-3}}$ per yr. This demonstrates that despite high carbon fluxes driven by the circulation, biology and air-sea gas exchange, the changes in the sDIC concentration are relatively small.

The tendency of sDIC due to the air-sea CO_2 flux (J_{surf}) globally averages to $0.5\,\mu\mathrm{mol\,C\,m^{-3}d^{-1}}$, which is much less than the global averages of J_{bio} and J_{circ}. Locally however, J_{surf} has large positive and negative values (Figure 4.14a). The geographic pattern of J_{surf} is similar to the air-sea CO_2 flux (F_{surf}) per surface area (compare to Figure 4.1a), but values are larger in magnitude where the mixed layer is shallow (e.g. in the EQU biome) and smaller in magnitude where the mixed layer is deep (e.g. in the STSS and SPSS biomes). This is because carbon which is added or removed at the air-sea interface is dispersed over the mixed layer depth and affects the sDIC concentration in inverse proportion to the MLD. Because regions with a shallow mixed layer such as the EQU biome tend to be regions of outgassing and regions with deep mixed layers such as the STSS and SPSS biomes tend to be regions of CO_2 uptake, the global mean J_{surf} is more negative compared to what might be expected from the global mean air-sea CO_2 flux. The small positive value of the globally averaged J_{surf} in sim-A is a consequence of the anthropogenic surface flux of CO_2, which is generally directed into the ocean. In contrast, the global mean J_{surf} is negative in sim-D ($-18.4\,\mu\mathrm{mol\,C\,m^{-3}d^{-1}}$), which is firstly the effect of mixed layer thickness and secondly reflecting the impact of climate change in sim-D, in which the uptake of natural CO_2 (bias in sim-B) is reduced.

[3]Calculated as: $A - C + B$; Equation (3.5) plus an "artificial" drift (B) for consistency with the rest of the row
[4]Calculated as: $A - C - D + B$; Equation (3.8)

The tendency of sDIC due to the sinking of particulate organic carbon through the base of the mixed layer (J_{bio}) is negative everywhere and globally averages to $-73\,\mu mol\,C\,m^{-3}d^{-1}$, i.e. it constitutes a sink of mixed layer sDIC (Figure 4.14b). In the EQU and STPS biome, J_{bio} is small. The exception to this is the East Pacific EQU biome, which has a fairly high biological productivity. In the simulations used here, the East Pacific EQU region features the highest mean value for net primary production of all biomes, which means that it is overestimated relative to other regions by the model (compared to satellite chlorophyll observations from NASA (2021)). Together with a shallow mixed layer, the resulting J_{bio} in the East Pacific EQU biome is large ($0.3\,mmol\,C\,m^{-3}d^{-1}$). Besides that, J_{bio} is elevated in coastal upwelling systems, which combine high biological productivity with shallow mixed layers. Furthermore, J_{bio} is high in all biomes where mixing is deep enough to sustain high biological productivity and where the sinking particles acquire high sinking velocities at the base of the mixed layer, which are the North Atlantic SPSS ($0.2\,mmol\,C\,m^{-3}d^{-1}$), the Southern Ocean SPSS ($0.05\,mmol\,C\,m^{-3}d^{-1}$), the STSS ($0.1\,mmol\,C\,m^{-3}d^{-1}$) and the ICE biome ($0.1\,mmol\,C\,m^{-3}d^{-1}$).

Tendencies in sDIC due to the circulation (J_{circ}) are mostly positive, i.e. J_{circ} constitutes a source of sDIC to the mixed layer, because on the one hand, DIC-depleted surface waters are transported downward and on the other hand, upwelling brings DIC-rich deep water waters to the surface. Globally, J_{circ} averages to $75\,\mu mol\,C\,m^{-3}d^{-1}$, of which $92\,\mu mol\,C\,m^{-3}d^{-1}$ are due to the upwelling of natural sDIC (sim-D) and $-17\,\mu mol\,C\,m^{-3}d^{-1}$ due to the downward transport of anthropogenic sDIC (sim-A minus sim-D). While there is a difference in the global average of J_{circ} between simulations due to the transport of anthropogenic carbon, the geographical distribution of J_{circ} is similar in all simulations, meaning that the geographical distribution is dominated by the transport of natural carbon. The geographical distribution of J_{circ} resembles J_{bio}, but with a reversed, thus positive, sign. The most prominent feature is in the EQU East Pacific region, where equatorial upwelling provides a strong supply of sDIC to the surface. Enhanced J_{circ} due to equatorial upwelling is also found in the EQU biomes in the West Pacific and Atlantic. Moreover, J_{circ} is locally high in coastal upwelling systems and elevated in the North Pacific SPSS and in the southern hemisphere ICE biome due to wind-driven upwelling. Regions where J_{circ} is negative are few and J_{circ} is generally low in magnitude in these places. They are found in the subtropical gyres of the Indian Ocean, North Pacific and South Pacific due to wind-driven downwelling in the gyres.

The geographical resemblance in J_{bio} and J_{circ} suggests a link between these two factors. Firstly, with the upwelling of DIC-rich waters, nutrients are transported to the surface, thus favoring a higher biological productivity. Moreover, a possible explanation is that some of the particulate organic carbon which has sunken below mixed layer depth (J_{bio}) is entrained into the mixed layer again during its deepening, which is then attributed to J_{circ}. The East Pacific EQU biome, which has highly negative J_{bio} and highly positive J_{circ}, is also the region with the highest interannual variability of CO_2 flux density (not shown). This suggests that despite compensation of J_{bio} and J_{circ} in the longterm mean, they do not always compensate on the interannual scale.

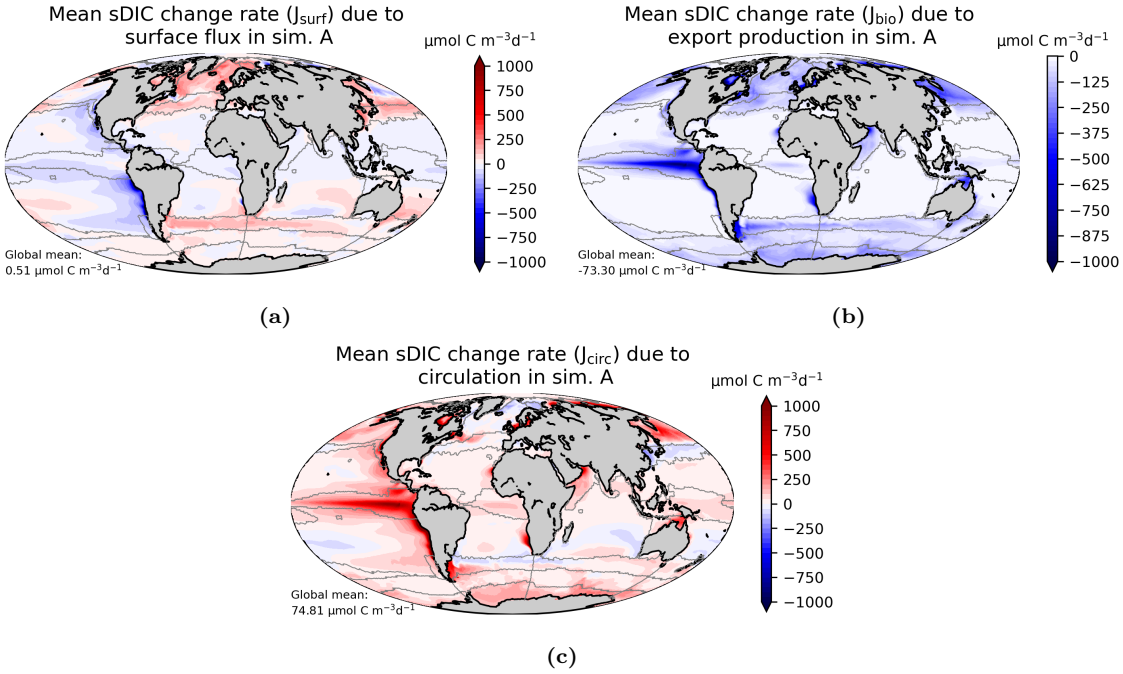

Figure 4.14: Regional distribution of carbon fluxes per volume of mixed surface water in sim-A. A positive flux corresponds to an increase in sDIC concentrations, i.e. positive is either due to the supply of sDIC from below with circulation or due to uptake of atmospheric CO_2. The regional distribution is very similar in sim-B, sim-C and sim-D (Figure S8, Figure S9, Figure S7).

4.2.10.2 Attributing the global trend in sDIC concentrations to changes in biology and circulation

In the historical simulation (sim-A), the drift-corrected trend in global mean mixed layer sDIC concentration is positive, i.e. towards an increasing sDIC concentration ($0.76\,\mathrm{mmol\,C\,m^{-3}\,per\,yr}$, Table 4.4, [5]). This is an effect of a trend in J_{surf} towards more uptake at the air-sea interface ($2.58\,\mathrm{mmol\,C\,m^{-3}\,per\,yr}$) and of an initial imbalance ($0.52\,\mathrm{mmol\,C\,m^{-3}\,per\,yr}$), which are opposed by a trend in J_{circ} towards enhanced downward transport of sDIC ($-2.65\,\mathrm{mmol\,C\,m^{-3}\,per\,yr}$). In comparison, the biological term is smaller ($\beta(\mathrm{sDIC})_{bio} = 0.32\,\mathrm{mmol\,C\,m^{-3}\,per\,yr}$). The effect of the trend in J_{surf} on the trend in sDIC ($\beta(\mathrm{sDIC})_{surf}$) is controlled by the trend in the air-sea flux, which is driven by the increasing atmospheric CO_2 concentrations and impacted by climate change. The effect of the increasing atmospheric CO_2 concentration is dominant. Thus, J_{surf} generates anthropogenic growth of the mixed layer sDIC, which is then transported into the deep ocean with the ocean circulation, as seen in the negative value of $\beta(\mathrm{sDIC})_{circ}$. This trend towards a higher transport of anthropogenic carbon to depth offsets almost 80% of the increase in the mixed layer sDIC concentration due to the trends in J_{surf} and J_{bio}. About 15% ([6]) of the increase in the mixed layer sDIC concentrations over the period 1958-2019 is due to the initial imbalance, implying that the anthropogenic perturbation has already been present at the beginning of the simulated time series.

[5] Numbers in the text of Section 4.2.10.2 are given with drift-correction, i.e. with the respective trend from sim-B subtracted; original numbers without drift-correction are shown in Table 4.4.

[6]
$$0.15 = \frac{\beta(\mathrm{sDIC})_{init}}{\beta(\mathrm{sDIC})_{surf} + \beta(\mathrm{sDIC})_{bio} + \beta(\mathrm{sDIC})_{init}} = \frac{0.52}{2.58 + 0.32 + 0.52}$$

Table 4.4: Trend in the global mean mixed layer sDIC (in mmol C m^{-3} per yr) separated into contributions due to the trend in the air-sea CO_2 exchange (J_{surf}), biological fluxes (J_{bio}) and circulation (J_{circ}). On the left: original value. On the right in brackets: with drift correction by subtracting sim-B.

	sim-A		sim-B	sim-C		sim-D	
Global mean trend in sDIC	0.75	(0.76)	-0.01	0.77	(0.78)	-0.03	(-0.02)
Trend in sDIC expected from ...							
... $\beta(J_{surf})$	2.98	(2.58)	0.40	4.00	(0.76)	-0.99	(-1.39)
... $\beta(J_{bio})$	0.08	(0.32)	-0.24	-0.24	(0.00)	0.08	(0.32)
... $\beta(J_{circ})$	-2.80	(-2.65)	-0.15	-3.81	(-3.66)	0.82	(0.97)
Expected from the init. imbalance	0.49	(0.52)	-0.03	0.41	(0.44)	0.06	(0.09)

In contrast, in the simulation with constant atmospheric CO_2 concentrations but with a changing climate (sim-D), the trend in global mean mixed layer sDIC concentration is slightly negative (-0.02 mmol C m^{-3} per yr, Table 4.4). This can be understood as an adjustment to the reduced solubility of CO_2 caused by the increasing temperatures over the simulation period (see Section 4.2.3). Meanwhile, changes in the circulation generate a positive trend in sDIC (0.97 mmol C m^{-3} per yr), i.e. towards more upwelling of natural carbon. Together with positive trends in J_{bio} and the initial imbalance, these factors would give rise to a positive trend in mixed layer sDIC concentrations, if it wasn't for the almost perfect compensation by a trend towards more outgassing of natural carbon at the air-sea interface ($\beta(\text{sDIC})_{surf}$: -1.39 mmol C m^{-3} per yr).

Changes in the transport of sDIC with the circulation (J_{circ}) can generally be generated by two processes, of which one is the increasing supply of anthropogenic carbon at the surface and the other is the variability of the circulation and mixed layer depth due to climate variability. In sim-C, the circulation is invariant and the only effect on the transport of sDIC stems from the increasing supply of anthropogenic CO_2 at the surface (4.00 mmol C m^{-3} per yr, Table 4.4). The anthropogenic carbon is then transported downward, which leads to a reduction of the trend in mixed layer sDIC by -3.66 mmol C m^{-3} per yr. In contrast, in sim-D, which does not include anthropogenic carbon, changes in the circulation only lead to changes in sDIC concentrations via the natural carbon cycle, and in this experiment, the effect of the trend in J_{circ} is to increase the mixed layer sDIC concentration as natural carbon is increasingly upwelled (0.97 mmol C m^{-3} per yr). Consequently, the trend in mixed layer sDIC caused by J_{circ} in the historical simulation, sim-A (-2.65 mmol C m^{-3} per yr), is the sum of the last two terms, i.e. the increasing content of anthropogenic sDIC in waters which are transported downward and the enhanced upwelling of waters rich in natural carbon. The part that cannot be explained by the sum is comparatively small (0.04 mmol C m^{-3} per yr), which means that the effect of climate-induced changes in circulation on the transport of anthropogenic carbon is comparatively small.

Overall, the trend in J_{bio} is the least important driver of the trend in the mixed layer sDIC concentration compared to changes in J_{surf} and J_{circ}, with the contribution of $\beta(\text{sDIC})_{bio}$ being one order of magnitude smaller, Table 4.4). In this context, it should be noted that the choice of atmospheric CO_2 forcing has no influence on J_{bio} because in the model, biology is insensitive to the availability of anthropogenic carbon, ocean acidification or any other related processes. In sim-A and sim-D, the impact of climate variability is to reduce J_{bio} in magnitude, i.e. less organic carbon is exported from the mixed layer to depth, which leads to a positive trend in mixed layer sDIC concentration (yet a relatively small one).

4.2.10.3 Attributing regional trends in sDIC concentration to changes in biology and circulation

Constant atmospheric CO_2 and variable climate (Sim-D) In sim-D, the trends in the sDIC concentration result from the impact of climate change on the natural carbon fluxes (Figures 4.15a, 4.15c, 4.15e and 4.15g). In contrast, the anthropogenic component is absent (sim-C, Figures 4.15b, 4.15d, 4.15f and 4.15h). The net trend in sDIC in sim-D is small (Figure 4.15a) compared to the contributions induced by the trends in J_{surf} (Figure 4.15c), J_{bio} (Figure 4.15e) and J_{circ} (Figure 4.15g). The regional pattern of the net trend in sDIC is described in Section 4.2.8.

In sim-D, the regional variability of J_{bio}-related trends in sDIC concentration is high (Figure 4.15e). Locally, the maximum J_{bio}-related trends in sDIC concentration surpass $\pm 300\,\mathrm{mmol\,C\,m^{-3}\,per\,yr}$, whereas the global mean is just $0.08\,\mathrm{mmol\,C\,m^{-3}\,per\,yr}$ (0.32 after drift-correction, Table 4.4). As a consequence of the high regional variability, the interannual variability and the quadratic terms described in Section 3.2.7, a possible error in the global mean trend is $0.29\,\mathrm{mmol\,C\,m^{-3}\,per\,yr}$ just due to the order of averaging and calculating the trend [7]. Another uncertainty is generated through the model drift (Figure S10c). Positive J_{bio}-related trends in the sDIC concentration, i.e. trends towards a higher sDIC concentration in the mixed layer resulting from reduced organic export, are found in the EQU biomes in the East Pacific and Atlantic. Furthermore, positive J_{bio}-related trends in the sDIC concentration occur in the North Atlantic, even though a part of the trend in the North-Atlantic seems to be caused be the model drift (Figure S11f). One likely cause for the reduced organic export is a trend towards less deep mixed layers in the North Atlantic SPSS and also in parts of the North Atlantic STSS and STPS (Figure S19b), which shows a regional correspondence with the changes in J_{bio} and could be responsible for lower sinking velocities of organic particles, which are calculated as a function of depth in FESOM-REcoM. In contrast, negative J_{bio}-related trends in sDIC concentration, i.e. trends towards a reduced sDIC concentration because of enhanced organic export, are found in the southern hemisphere ICE biome, the Southern Ocean SPSS biome and parts of the Southern Ocean STSS south of Australia. They are accompanied by a trend towards deeper mixed layers and higher primary productivity (Figure S14b).

The regional variability of J_{circ}-related trends in sDIC concentration is even higher than that of J_{bio}-related trends (Figure 4.15g). The effect of J_{circ}-related trends is to compensate for almost all of the J_{bio}-related trends in sDIC concentrations. Possibly, this is an artifact of calculating the J_{circ}-related trends as the residual, with all other terms being smaller in many regions (compare e.g. $\beta(\mathrm{sDIC})_{surf}$ in Figure 4.15c and the net trend in sDIC β(sDIC) in Figure 4.15a). Even though there is possibly an artifact, parts of the J_{circ}-related trends in sDIC can be explained through changes in the ocean circulation. Negative J_{circ}-related trends in the sDIC concentration, i.e. trends towards a reduced mixed layer sDIC concentration because of changes in the transport of sDIC, occur along the equator in the East Pacific and Atlantic. In fact, here, vertical velocities at 100m show a trend towards less upwelling directly at the equator and more upwelling off the Equator (Figure S13b). Moreover, J_{circ}-related trends in sDIC concentrations are negative near the North Atlantic Current and North Pacific current. A signal of this appears in the net trend in mixed layers sDIC (Figure 4.15a). There are no significant trends in vertical velocity there, but a trend towards deeper mixed layers. Besides, this could be an effect of changes in the horizontal transport of sDIC with surface ocean currents, which has not been assessed here. In the northern hemisphere subpolar biomes, the J_{circ}-related trends in sDIC concentration are regionally heterogeneous and strongly affected by applying or not applying the model drift-correction (compare to Figure S11h). The structures of the North Atlantic Subpolar Gyre and the maximum sea-ice extent are visible, but associated with locally positive as well as locally negative trends. In the STPS biome, the J_{circ}-related trends in sDIC concentration are spatially heterogeneous, implying that trends in sDIC related to the ocean circulation depend on local conditions. In the Southern Ocean, namely in the Southern

[7] If $\beta(\mathrm{sDIC})_{bio}$ is calculated at every grid cell, it globally averages to $-0.21\,\mathrm{mmol\,C\,m^{-3}\,per\,yr}$. If the global mean $\beta(\mathrm{sDIC})_{bio}$ is derived from the timeseries of the global mean J_{bio} , it is $0.08\,\mathrm{mmol\,C\,m^{-3}\,per\,yr}$

Ocean ICE biome, Southern Ocean SPSS biome and parts of the STSS biome, the J_{circ}-related trends in sDIC concentration are positive, i.e. towards an increased mixed layer sDIC concentration. Here, the signal of $\beta(\text{sDIC})_{circ}$ is visible in the net trend in mixed layer sDIC (Figure 4.15a). On the one hand, there is a wind-driven enforcement of upwelling in the Southern Ocean ICE and SPSS biomes seen in the vertical velocities at 100m (Figure S13b), which brings natural sDIC to the surface (Lovenduski et al., 2007; Hauck et al., 2013b). On the other hand, there is an increase in downwelling in the Southern Ocean STSS. The trend in the vertical velocities is only statistically significant in the Indian Ocean sector (Figure S13b). Additionally, the mixed layer is deepening in the Southern Ocean SPSS and parts of the ICE and STSS biomes (Figure S19b).

Overall, where J_{bio} and J_{circ} do not already fully compensate each other (such as the compensation in equatorial regions and some areas of coastal upwelling), J_{surf} acts to compensate for any change in sDIC levels induced by changes in circulation and biology (Figure 4.15c). The remaining regional variability where J_{bio} and J_{circ} do not compensate, e.g. in the STPS and in the subpolar regions of the Northern hemisphere, stems mostly from J_{circ}. Here, the J_{surf}-related trends in sDIC concentration resemble the J_{circ}-related trends in terms of their spatial distribution, but with the opposite sign. Consequently, most of the trends in the air-sea CO_2 flux that arise from changes in the sDIC concentration are due to changes in circulation and not biology. Contrariwise, it can also be argued that most of the trends in the transport of sDIC go back to changes in the air-sea flux that arise from other processes, such as warming-related outgassing. The role of J_{circ} is then to stabilize the mixed layer sDIC concentration by replacing surface waters with unmodified waters. While it is sometimes unclear if the trend in J_{circ} is a consequence of changes in J_{surf} or the other way around, it is clear that the role of changes in biology is comparatively less important. The exception to this is the Southern Ocean, where a considerable part of the J_{surf}-related trends in sDIC relates to trends in J_{bio}, but a part of these changes stem from the model drift (compare Figure S11f). This leads to a spatially heterogeneous pattern of trends in J_{surf} in the Southern Ocean. In places in the Southern Ocean where changes in J_{circ} are dominant over J_{bio}, e.g. in the Atlantic sector of the ICE biome, negative J_{surf}-related trends arise, i.e. trends towards more outgassing. However, in places where changes in J_{bio} are dominant, e.g. in the SPSS region south of South America, positive J_{surf}-related trends arise, i.e. trends towards more uptake.

Increasing atmospheric CO_2 and constant climate (sim-C) In sim-C, sDIC concentrations increase everywhere on the globe (Figure 4.15b). The trend in sDIC is somewhat stronger in regions with a lower buffer factor, i.e. in the tropics and subtropics (Figure S4a). Nevertheless, the trend in sDIC is regionally much more uniform and overall weaker than what is expected from the trend in J_{surf} (Figure 4.15d).

The trend in sDIC concentrations caused by a trend in J_{surf} is positive almost everywhere, but shows substantial regional variability (Figure 4.15d). Since the increase of atmospheric CO_2 is regionally uniform at about 1.5µatm per yr, this variability must stem from regional variability in oceanic variables. The trend in sDIC related to J_{surf} is enhanced where the gas transfer coefficient is high, i.e. in the westerly wind zone and to lesser extent in the trade wind regions. Furthermore, J_{surf} is high in all regions with high net primary production (Figure S14a). These are the equatorial East Pacific and the equatorial Atlantic, the upwelling systems off the coast of Chile and Peru, Mauritania, Namibia, Australia and in the Arabian Sea, the STSS biome in both hemispheres and the North Atlantic SPSS. Furthermore, the values are high in the Southern Ocean ICE biome, which features high mean J_{bio} (Figure 4.14) despite the comparatively low primary production in that region (Figure S14a). Despite the enhanced sDIC concentration in the surface water, the J_{bio} remains invariant (Figure 4.15f) as biological activity is insensitive to the sDIC concentrations in the version of REcoM used here. The role of biology is thus not the fixation and export of anthropogenic CO_2. Rather, its role is to produce naturally undersaturated surface waters which have the capacity to take up anthropogenic carbon under rising atmospheric CO_2 concentrations. The largest part of the additional anthropogenic carbon is then removed from the mixed layer by the

circulation (J_{circ}, Figure 4.15h), which reduces the increase rate of mixed layer sDIC concentrations (Figure 4.15b). Furthermore, the impact of the circulation is to distribute the anthropogenic carbon horizontally, thereby making the net trend in mixed layer sDIC globally more uniform compared to $\beta(\text{sDIC})_{surf}$ (compare Figure 4.15b and Figure 4.15d).

Increasing atmospheric CO_2 and variable climate (sim-A) Sim-A includes the effect of increasing atmospheric CO_2 and the effect of changes in circulation and biology on the natural carbon cycle, which were described above. Any trend in sDIC in sim-A that cannot be explained as the sum of the respective trend in sim-C and sim-D must either be attributed to the impact of climate change on the anthropogenic carbon cycle (Equation (3.8)) or be an effect of the model drift, which is included as one summand in each of sim-A, sim-C and sim-D (Equations (3.2) and (3.6)). Consequently, the regional patterns in the net trend in sDIC and in its components from J_{surf}, J_{bio} and J_{circ} in sim-A are mostly the sum of the respective trends in sim-C and sim-D.

The net trend in mixed layer sDIC concentration in sim-A is positive almost everywhere as a consequence of increasing atmospheric CO_2 concentrations (Figure 4.16a). As in sim-C (Figure 4.15b), the generally positive trend in sDIC is somewhat weaker in the Southern Ocean and around the EQU biomes in the Atlantic and Pacific. The regional variability generated by climate change that is known from sim-D (Figure 4.15a) is superimposed, which makes the trend in sim-A spatially more heterogeneous than in sim-C.

The J_{bio}-related trends in sDIC are the same in sim-A as in sim-D (Figure 4.16c, Figure 4.15e). Sim-D is described above.

The trends in the sDIC concentration due to trends in J_{surf} are mostly positive, i.e. towards enhanced sDIC concentrations generated by increasing air-sea flux into the ocean (Figure 4.16b). Most of the positive trends $\beta(\text{sDIC})_{surf}$ are found in the tropics and at high latitudes, whereas the trends in the subtropics are often weak and sometimes negative. The positive trends in sim-A correspond to sim-C (Figure 4.15f). In fact, all of the regions with strongly positive trends in sim-C, e.g. in the Southern Ocean, in the Equatorial Pacific and in the subpolar North Atlantic, are also found in sim-A. In contrast, in the STPS, where only few strongly positive J_{surf}-related trends in sDIC are found in sim-C, sim-A even reveals regions with negative J_{surf}-related trends that correspond to the same regions in sim-D with negative trends (Figure 4.16c).

Concerning the trends in sDIC related to J_{circ} in sim-A, the sum of the trends from sim-C and sim-D results in a spatially heterogeneous pattern with more negative than positive values, i.e. an overall reduction of the mixed layer sDIC due to the transport with the circulation (Figure 4.16d). The trends are stronger in the high latitudes of the northern hemisphere and in the East Pacific and Atlantic EQU biomes; and they are weaker in the STPS and in the Southern Ocean. In the Southern Ocean, where the trends are negative in sim-C and positive in sim-D, the resulting trends are partly positive and partly negative in sim-A: in the ICE biome, climate-induced upwelling dominates, whereas downward transport of anthropogenic carbon dominates in the SPSS and STSS. In the STPS biome, the trends in sim-A are relatively weak and regionally heterogeneous with a similar regional distribution as in sim-D, but with a negative tendency like in sim-C. In the EQU biomes in the East Pacific and Atlantic, the J_{circ}-related trends in sDIC are negative in sim-D and sim-C. Thus, they add up to the strongly negative trends seen in sim-A. In the high latitude northern hemisphere, both strongly positive and negative trends occur in sim-A. They result from a combination of strong, but spatially heterogeneous trends in that region in sim-D and negative trends with variable magnitude in that region in sim-C.

In summary, the trend in sDIC in the historical simulation is mostly positive due to the increasing atmospheric CO_2 concentrations. On the one hand, the oceanic circulation acts to globally homogenize and attenuate the increase in anthropogenic mixed layer sDIC concentrations by removing the anthropogenic carbon from the ocean surface. Thereby, climate-induced variability of the circulation has a comparatively small impact on the transport of anthropogenic sDIC with the circulation. In contrast, climate-induced trends in the transport of natural carbon with the circulation generate re-

gional variability and mostly lead to trends towards a higher mixed layer sDIC concentration related to enhanced upwelling. Which of the two processes - i.e. the downward transport of increasingly more anthropogenic sDIC or the enhanced upwelling of natural sDIC - is dominant depends on regional conditions. Globally, the downward transport of anthropogenic carbon is dominant. The role of changes in biology is comparatively small.

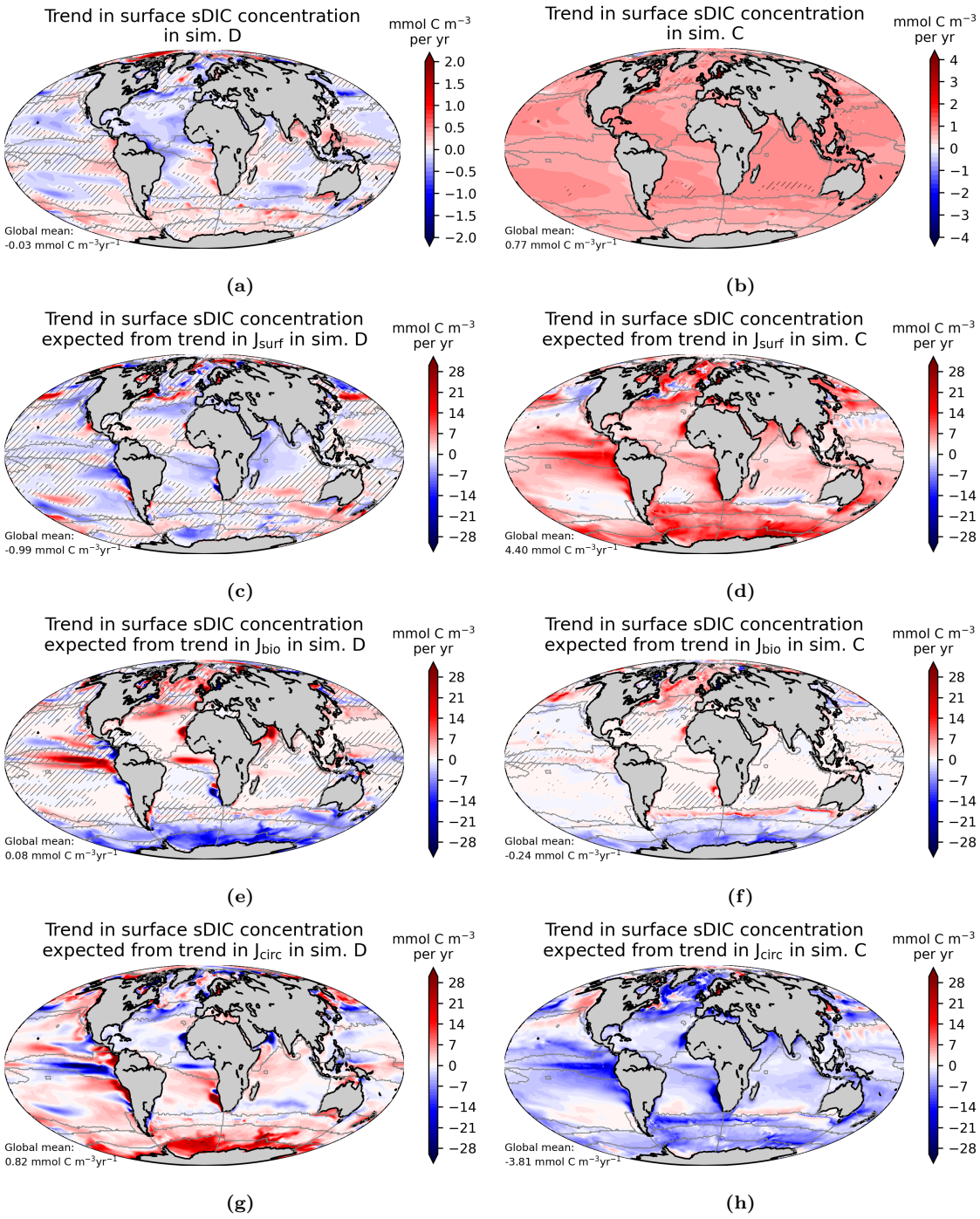

Figure 4.15: (a,b) Trend in sDIC concentration in sim-C and sim-D. (c-h) The components of the trend in sDIC concentration due to the trends in (c,d) J_{surf}, (e,f) J_{bio} and (g,h) J_{circ}. Positive values correspond to an increase in sDIC. Hatched areas mark low significance. In panels g and h, there is no information on the significance. The global mean is calculated as the trend in the global mean timeseries, not as the mean of the regional trends.

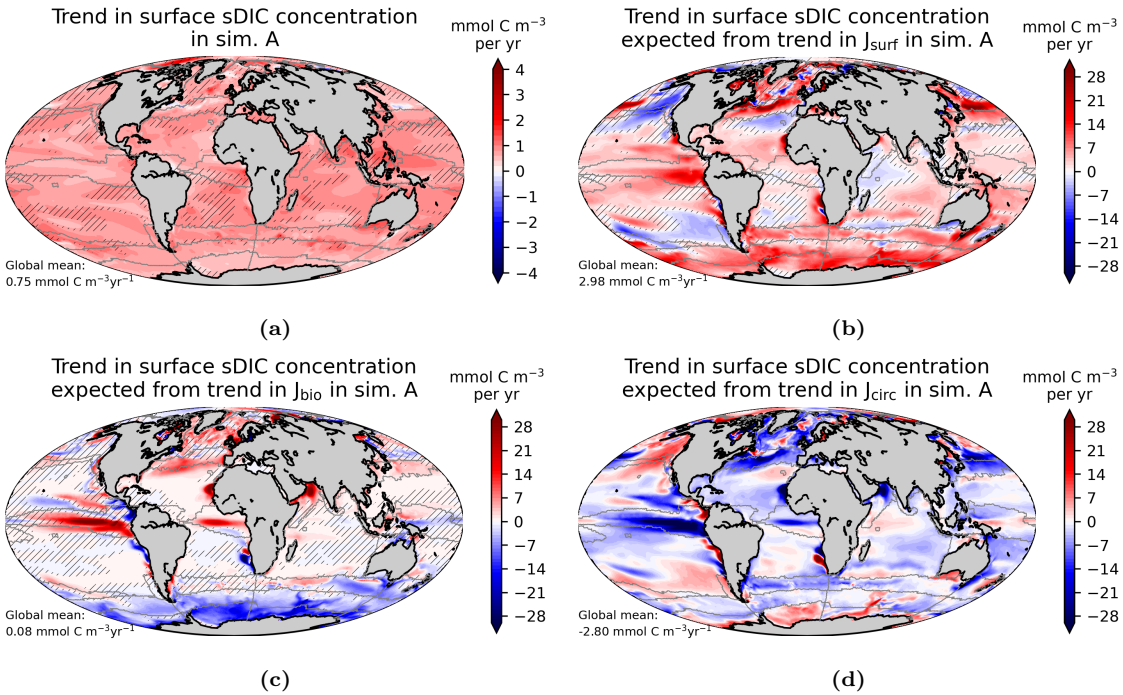

Figure 4.16: (a) Trend in sDIC concentration in sim-A. (b,c,d) The trends in sDIC concentration which are expected from the trends in (b) J_{surf}, (c) J_{bio} and (d) J_{circ}. Positive values correspond to an increase in sDIC. Hatched areas mark low significance. In panel d, there is no information on the significance. The global mean is calculated as the trend in the global mean timeseries, not as the mean of the regional trends.

4.3 Results from doing a series of simulations

4.3.1 Overview of all separable factors affecting the trend in the global CO_2 flux

The trend in the globally integrated CO_2 flux in the historical simulation (sim-A) arises from a combination of processes that were separated by a series of simulations as described in Section 3.1. The most prominent effect is that of rising atmospheric CO_2 concentrations, which generates an increase in the ocean's CO_2 uptake rate by 30.4 $\mathrm{Tg\,C\,yr^{-1}}$ per yr, which is equivalent to 112% of the net trend in sim-A (Figure 4.17). While 10% of the trend in sim-A can be attributed to the model drift, climate change and variability reduce the trend by -6.5 $\mathrm{Tg\,C\,yr^{-1}}$ per yr (-24%).

Climate change and variability mostly caused an outgassing of natural CO_2 ($-0.09\,\mathrm{Pg\,C\,yr^{-1}}$ with a trend of $-7.2\,\mathrm{Tg\,C\,yr^{-1}}$ per yr, Table 4.5). The impact of climate on the uptake of anthropogenic carbon was much smaller. On the one hand, climate change and variability attenuated the uptake of anthropogenic carbon by $-0.01\,\mathrm{Pg\,C\,yr^{-1}}$ on average, as it would be expected e.g. from global warming and the reduced solubility of natural and anthropogenic CO_2 at the sea surface. Simultaneously, climate change and variability also induced a trend in the flux of anthropogenic carbon towards more uptake ($0.6\,\mathrm{Tg\,C\,yr^{-1}}$ per yr). This is what would be expected from an accelerating overturning circulation, in which the removal of anthropogenic carbon from the surface ocean into the depth is accelerating. Yet, my estimate of the impact of climate variability on the uptake of anthropogenic CO_2 is uncertain because the value is so small, with the model drift and bias being more than 3 times larger.

Each of the climate forcings separated here - winds, sea surface temperature and other climate forcings together with the nonlinear effect - accounts for an important part of the effect of climate variability on the trend in the historical air-sea CO_2 flux (Figure 4.17, red bars). Amongst all climate forcings, winds have the largest control on the trend in the CO_2 flux, being responsible for 45% of the climate effect on the trend in the CO_2 flux. The effects of sea surface temperature amounts to 34% and the others together with the nonlinear effect are smaller in comparison (21%). The others summarize the effect of change and variability in freshwater fluxes, sea level pressure and the nonlinearity that is generated due to the combination of variability in the individual climate forcings.

From 1958 to 2020, the ocean in the historical simulation (sim-A) cumulatively took up 93.5 PgC more than in the control simulation (sim-B, Table 4.6). Without any of the climate variability (sim-C), the ocean would even have taken up 6.3% (5.9 PgC) more than that. Without the variability of winds (sim-F), it would have been 5.7% (5.4 PgC) more and without the variability of temperature (sim-E), it would have been 1.9% (1.8 PgC) more. This means that surprisingly, the impact of the other climate change and variability together with the nonlinear effect is to increase the cumulative CO_2 uptake over the simulated time period by 1.3 PgC, while simultaneously decreasing the trend in the CO_2 flux over the same period ($-1.3\,\mathrm{Tg\,C\,yr^{-1}}$ per yr, Figure 4.17).

The climate-driven trend of the globally integrated CO_2 flux has contributions from all biomes (Figure 4.18). The largest part (58% of the negative climate-driven trend in the regionally integrated CO_2 flux) stems from the STPS biome because it spans the largest area and here, both winds and temperatures cause a trend towards more outgassing. Furthermore, the Southern Ocean SPSS region alone accounts for another 22% of the negative climate-driven trend mainly due to the impact of winds there. The remaining 20% of the negative climate-driven trend in the regionally integrated CO_2 flux origin from the EQU, STSS and ICE biomes. About 16% of the regionally integrated negative trends are offset by positive trends, of which half stem from the North Atlantic SPSS and the adjacent ICE biome.

Both wind-driven and temperature-driven trends in the CO_2 flux are mostly negative, i.e. towards more outgassing, with the winds ($-2.9\,\mathrm{Tg\,C\,yr^{-1}}$ per yr) contributing more than the temperature ($-2.3\,\mathrm{Tg\,C\,yr^{-1}}$ per yr, Figure 4.18). The wind-driven negative trends in the integrated CO_2 flux

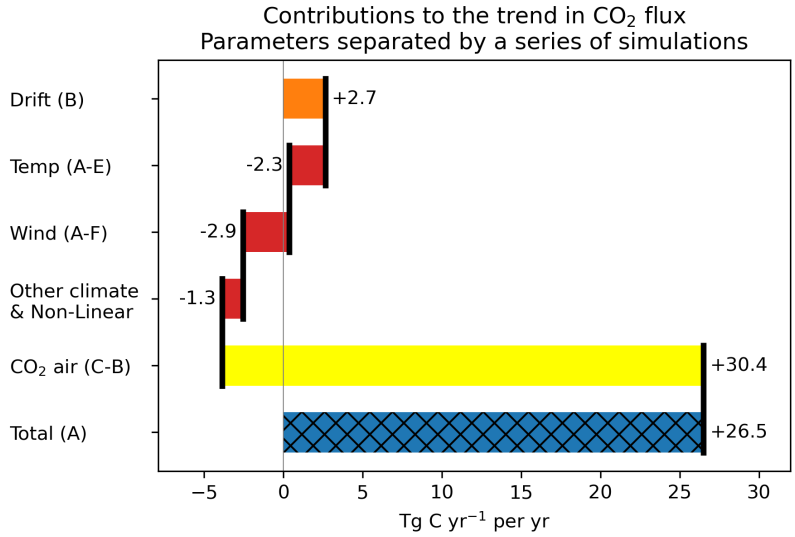

Figure 4.17: The parts of the trend of the globally integrated CO_2 flux caused by different effects, as derived by a series of simulations, are shown as bars in orange (model drift), red (climate) and yellow (atmospheric CO_2). They sum up to the total trend of CO_2 flux in the historical simulation (hatched blue bar at the bottom). Positive signifies an enhanced flux into the ocean. The effect of the other climatic forcing together with the nonlinear effect is calculated from simulations $E + F - A$ (Equation (3.15)).

are largely caused by the Southern Ocean SPSS and the STPS biome (40% and 38%). The remaining part mostly stems from the ICE and STSS biomes. A third of the negative wind-driven trend is offset by a wind-driven positive trends which stem from the North Atlantic STSS, North Pacific STSS and also the Indian Ocean STSS biome. The globally integrated temperature-driven trend in the CO_2 flux is dominated by the STPS biome due to its size. About a third of the negative regionally integrated trend is offset by a positive trend which stems from the North Atlantic SPSS and the adjacent ICE biome and from the Indian Ocean SPSS.

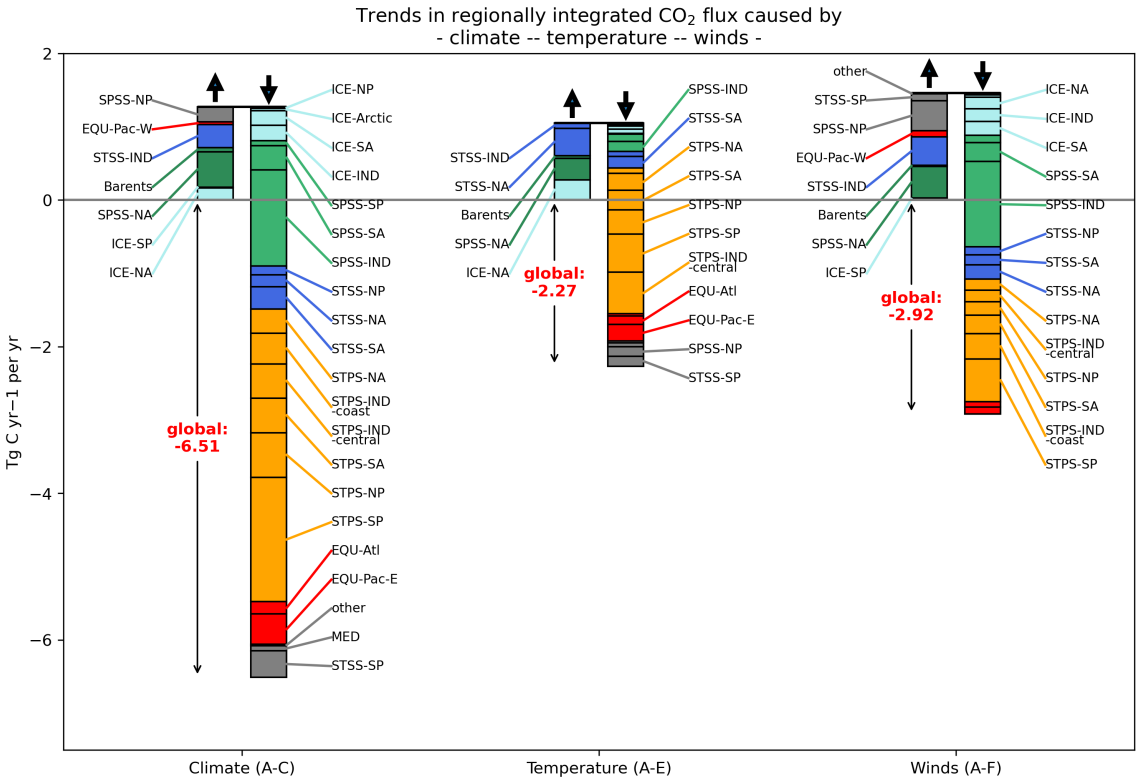

Figure 4.18: Trend in the regionally integrated CO_2 flux caused by the full climate change and variability and by winds and temperature separately. Positive denotes an enhanced flux into the ocean. As some canceling out of positive and negative trends happens already on the scale of regional integration, the results shown here depend on the choice of regions.

Table 4.5: The fluxes of natural (nat) and anthropogenic (ant) CO_2 in the presence (clim) and absence (no clim) of climate change and variability as defined in Section 3.1

(a) Mean CO_2 flux ($Pg\,C\,yr^{-1}$) from 1958-2019

Bias: **0.32**	Historical: **1.53**		
		Antropogenic: **1.62**	
	[clim, nat]: **-0.09**	[no clim, ant]: **1.63**	[clim, ant]: **-0.01**

(b) Trend in the CO_2 flux ($Tg\,C\,yr^{-1}\,per\,yr$) from 1958-2019

Drift: **2.7**	Historical: **23.9**		
		Antropogenic: **31.0**	
	[clim, nat]: **-7.2**	[no clim, ant]: **30.4**	[clim, ant]: **0.6**

(c) Cumulative CO_2 uptake ($Pg\,C$) from 1958-2019

Bias: **19.4**	Historical: **93.5**		
		Antropogenic: **99.0**	
	[clim, nat]: **-5.5**	[no clim, ant]: **99.4**	[clim, ant]: **-0.4**

Table 4.6: Cumulative carbon uptake from 1958 to 2019 in PgC

sim-A	sim-B	sim-C	sim-D	sim-E	sim-F
112.9	19.4	118.8	14.0	114.7	118.4

4.3.2 Regional impact of atmospheric CO_2 on the trend in the CO_2 flux density

The rising atmospheric CO_2 concentration leads to significant positive trends in the regional CO_2 flux density nearly everywhere on the globe (Figure 4.19). However, the magnitude of the trends is not spatially uniform. The impact of the increase in atmospheric CO_2 concentration is enhanced in the westerly wind zones in the STSS and SPSS in both hemispheres and in the trade wind zones in the STPS. Here, the presence of winds increases the gas exchange velocity k_w so that the increasing gradient of pCO_2^A and pCO_2^O is translated into strong trends in the CO_2 flux densities at high wind speeds. Furthermore, the trend in the CO_2 flux density caused by the increasing atmospheric CO_2 concentration is elevated where the mean export production is high, namely in all Southern Ocean biomes, as well in the STSS in the northern hemisphere, in the North Atlantic SPSS and in coastal upwelling systems. As described in Section 4.2.10, the ocean biology in REcoM does not react to the increasing atmospheric CO_2 concentrations and is thus not directly responsible for the uptake of any additional carbon. However, by drawing down the natural pCO_2^O during photosynthesis, ocean biology creates favorable conditions for the uptake of CO_2, which is amplified under increasing air-sea disequilibrium. The exception to this are the regions near the equator, where the high export production does not translate into an elevated trend in the CO_2 flux caused by atmospheric CO_2, possibly owing to a low gas transfer coefficient. In the Southern Ocean, the trends in the CO_2 flux caused by the rise of atmospheric CO_2 are zonally organized. Starting from the pole, they are low near the Antarctic continent and in the Weddell Sea and Ross Sea due to sea-ice cover, then high in the transition zone of the ICE and SPSS biome, somewhat smaller in the transition zone of the SPSS and STSS and then again higher in the STSS itself with exception of the East Pacific sector, where the STSS is narrower than in the rest of the Southern Ocean and also the trends are not as pronounced. In the North Atlantic, the trends in the CO_2 flux caused by the rise of atmospheric CO_2 are enhanced in the currents of the subpolar gyre, but not in the center of the gyre.

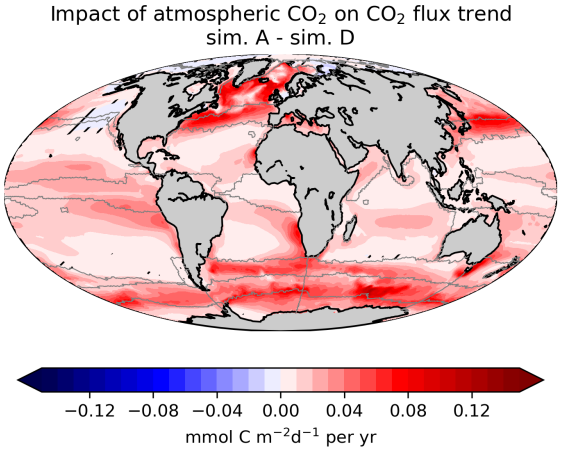

Figure 4.19: Impact of the increase of atmospheric CO_2 on the trend in the CO_2 flux density obtained as the difference between two simulations (sim-A minus sim-D, see Section 3.1). Positive signifies a trend towards more oceanic CO_2 uptake or less outgassing. (Sporadic) hatched areas indicate a low significance. The trend is significant almost everywhere.

4.3.3 Regional impact of climate variability on the trend in the CO_2 flux density

The impact of variability in climate on the trend in the CO_2 flux density results from the variability in temperature, winds and the other climate forcings, namely freshwater fluxes and sea level pressure. As outlined in more detail in the following, the largest part of the regional climate-driven variability in the trend in the CO_2 flux stems from winds (Section 4.3.3.1), whereas the impact of temperature is regionally often weaker, but globally more uniform (Section 4.3.3.2).

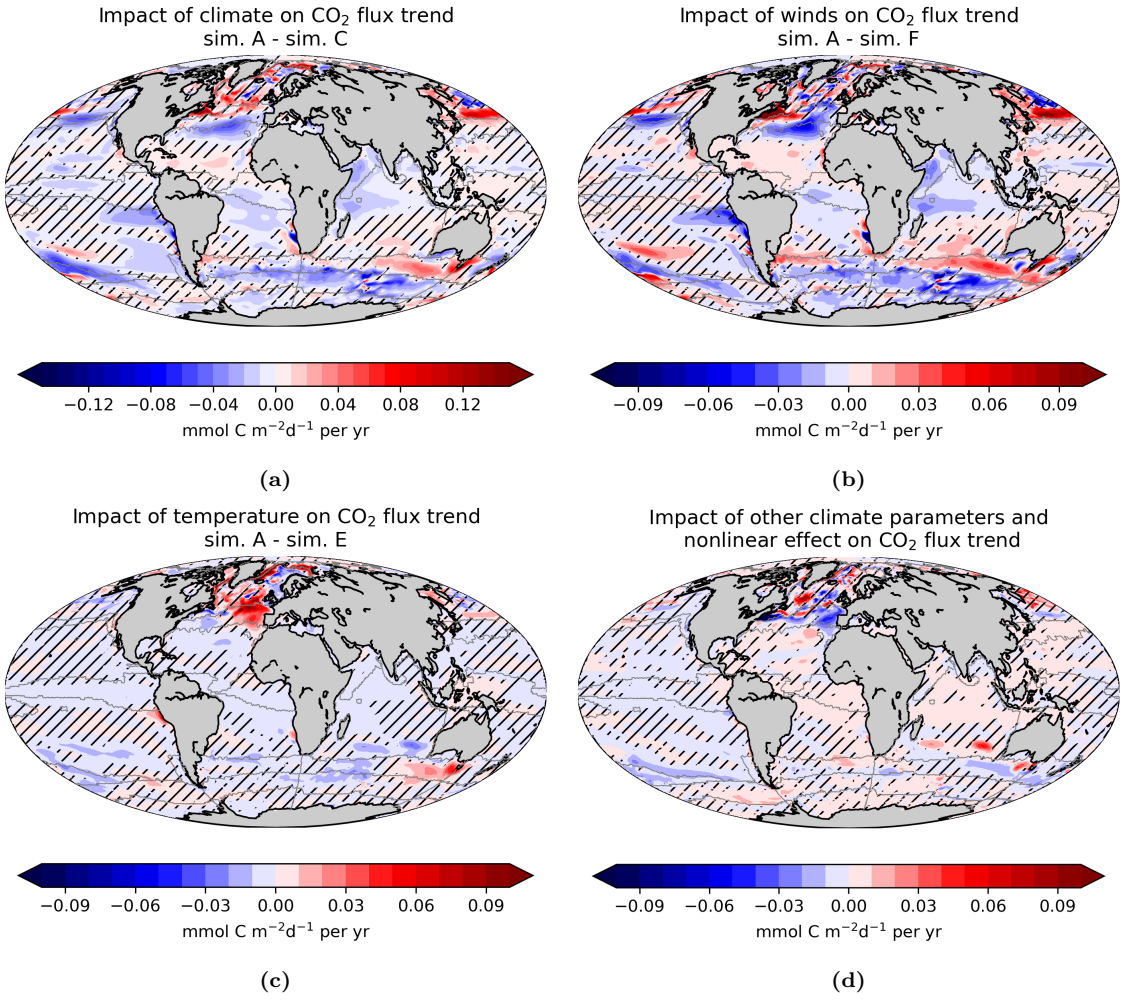

Figure 4.20: Impact of climate change and variability on the CO_2 flux trend obtained as the difference between two simulations (see Section 3.1). Positive denotes a trend towards more oceanic CO_2 uptake or less outgassing. Hatched areas indicate a low significance. (a) Full climate variability (b) Only winds. (c) Only temperature. (d) Other climate forcings and the nonlinear effect due to the combined variability of all climate forcings, calculated from simulations $E + F - A$ (Equation (3.15)).

4.3.3.1 Winds

The global mean trend in the CO_2 flux caused by trends and variability in winds is negative, i.e. towards more outgassing ($-1.8\,\mu mol\,C\,m^{-2}d^{-1}$ per yr, Figure 4.17). However, on a regional scale, the wind-driven trends in the CO_2 flux density are both positive and negative (Figure 4.20b). Their magnitude is weaker in the EQU and STPS biome and greater at high latitudes. This corresponds to the magnitude of the mean CO_2 flux density which is also weaker in the tropics and subtropics and greater at high latitudes (Figure 4.1a). The direct effect of the squared wind velocity on the global trend in the CO_2 flux via the gas transfer velocity k_w (see Sections 4.2.2 and 4.2.4) is in the opposite direction and somewhat smaller (~70%) than the all-encompassing effect of winds simulated here, and this direct effect of the wind velocity cannot explain the regional pattern either (compare Figure 4.20b and Figure 4.8c). Instead, the overall effect of winds on the global trend in the CO_2 flux appears to be dominated by indirect effects, involving implications of changes in the winds on the circulation.

In the Southern Ocean, the wind-driven trend in the CO_2 flux density varies with latitude, but is not zonally symmetric (Figure 4.20b). In the polar and subpolar zone, where the westerly winds over the SPSS drive an upwelling of water (Figure S13a and Figure S21a) and an outgassing of natural CO_2 in the mean state (Figure S1), the wind-driven trend is mostly towards enhanced outgassing of CO_2 in the ICE and SPSS biome. Reaching the STSS biome in the subtropics, where downwelling associated with the southern subtropical gyres occurs in the mean state, the trend is towards enhanced uptake of CO_2. The strengthening of the CO_2 flux densities in the respective regimes is assigned to the intensification of the westerly winds in the last decades which strengthens the upwelling and downwelling in the respective regimes (Hauck et al., 2013a). Although, we expect this to be visible in the trend in the vertical velocities (Figure S13c) and in the trend in the wind curl (Figure S21b), it is not. Furthermore, the effect also depends on the vertical gradient of sDIC (which is not assessed here). In addition to that, the variability of winds causes an enhanced primary production in several parts of the Southern Ocean related to a deepening of the mixed layer (Figure S19d, Figure S14d). While this cannot explain the meridional gradient, it might explain the zonal asymmetry, as the regions of enhanced CO_2 uptake in the East Atlantic, Indian Ocean and Australian sectors of the STSS biome coincide with more primary production and mixed layer deepening in the same places.

In the STPS and EQU biomes, the impact of winds on the trend in the CO_2 flux density is comparatively weaker (Figure 4.20b). In the South Atlantic STPS, the effect is negative, i.e. a trend towards more outgassing, which appears contradictory to a wind-driven surface cooling (Section 7.6) and an increase in primary production in this area (Figure S14d). Additionally, it doesn't seem to be related to the direct effect of winds on the gas transfer velocity (Figure 4.8c), trends in mixed layer depth (Figure S19d), vertical velocities (Figure S13c), salinity (Figure S17b) or alkalinity either (not shown). Similarly, the positive effect in the North Atlantic STPS remains unexplained. In the Indian Ocean STPS, the effect of winds on the trend in the CO_2 flux density is negative (Figure 4.20b), i.e. towards less CO_2 uptake, which regionally coincides with a shoaling of the mixed layer (Figure S19d).

In the North Atlantic, westerly winds are strengthening in the subpolar zone but winds are weakening in the subtropics in the seasonal transition zone of westerlies and trade winds (Figure 4.8b). Upwelling in the subpolar gyre (north of ~40°N) and downwelling in the northern part of the subtropical gyre (between ~30-40°N) are strengthened (Figure S13c) and the North Atlantic Current is shifted northward (Figure S20d). Off the US coast, this is associated with an increase in temperature and salinity, a deepening of the mixed layer, an increase in primary production (Section 7.6 and Figures S14d, S17b and S19d) and a trend in the CO_2 flux density towards more CO_2 uptake (Figure 4.20b). Towards the south and east of this, i.e. in the northern part of the STPS biome and in the Eastern part of the STSS biome, the mixed layer is shoaling, primary production decreases and there is a trend in the CO_2 flux density towards more outgassing. In most of the North Atlantic SPSS apart from the area off the US coast, the impact of winds on the CO_2 flux density is spatially

heterogeneous.

In the North Pacific, the impact of winds on the CO_2 flux density has a similar spatial structure as in the North Atlantic (Figure 4.20b). The North Pacific Current is shifted northward (Figure S20d). In the south-western part of the SPSS off Japan, the trend in the CO_2 flux density is towards more CO_2 uptake. To the west in the STSS, the trend in the CO_2 flux density is towards more outgassing.

In summary, the trend in the CO_2 flux density driven by winds is globally heterogeneous. It is mostly related to wind-driven changes in the circulation, firstly in the Southern Ocean related to wind-driven strengthening of upwelling and downwelling; and secondly in the northern hemisphere related to a shift of the North Atlantic and North Pacific Current. Locally, the strongest trends are found in the south-western parts of the North Pacific and North Atlantic SPSS biomes with an increase in the CO_2 uptake of more than 0.1 $\mathrm{mmol\,C\,m^{-2}d^{-1}\,per\,yr}$. The results need to be interpreted with caution as the choice of the wind forcing might affect the regional trends in the CO_2 flux density via wind- and circulation-driven changes in the ocean biology or the sea surface temperature (Le Quéré et al., 2010). The impact of winds on the gas transfer velocity as obtained with the offline calculation in Section 4.2.4 cannot explain the simulated pattern.

4.3.3.2 Temperature

The temperature-driven trend in the CO_2 flux examined here is defined as the difference in the trends in sim-A (full climate variability) and sim-E (no anthropogenic warming), acknowledging that there is a small additional temperature effect due to the remaining variability of temperature in sim-E, which is set up aiming to remove the impact of global warming (Figure 4.21a). As the remaining temperature variability in sim-E is small, the trends in the temperature difference between sim-A and sim-E capture most of the temperature trends in the historical simulation (compare Figure 4.21b and Figure 4.7b). According to the difference of sim-A and sim-E, the global mean ocean surface has warmed by 0.48°C during the simulated period from 1958 to 2019 with a downward decadal trend at the beginning of the timeseries and an increase in global mean temperature since the 1970s. The warming is strongest in the North Atlantic, which is consistent with the more rapid warming observed in the North Atlantic since the latter half of the 20th century (Marsh et al., 2008). The warming is weakest in the Southern Ocean ICE and SPSS biome, which is attributed to the upwelling of unmodified waters from depth (Armour et al., 2016). In the STPS and EQU biomes, the warming is relatively uniform around the global mean rate, but higher in the western Indian Ocean basin. The western Indian Ocean is known to feature a longterm temperature trend throughout the last century at a warming rate higher than that of any other ocean (Roxy et al., 2014). As a consequence of the global warming, weak temperature-driven trends in the CO_2 flux density towards more outgassing of up to $-0.01\,\mathrm{mmol\,C\,m^{-2}d^{-1}\,per\,yr}$ prevail in most of the ocean with statistical significance in about half the area (Figure 4.20c), averaging to $-1.4\,\mathrm{\mu mol\,C\,m^{-2}d^{-1}\,per\,yr}$. This is one magnitude less outgassing than expected from the offline linear approximation (widespread temperature-driven trends up $-0.02\,\mathrm{mmol\,C\,m^{-2}d^{-1}\,per\,yr}$ averaging to $-11.7\,\mathrm{\mu mol\,C\,m^{-2}d^{-1}\,per\,yr}$ in sim-A, Figure 4.7c and Table 4.3).

Consistent with the strong temperature trend in the North Atlantic, the impact of temperature on the trend in the CO_2 flux density is highest there (Figure 4.20c). Surprisingly, the trends in the North Atlantic are mostly positive, i.e. towards more CO_2 uptake, but there are also regions in the North Atlantic with negative values. This suggests the presence of competing effects. Firstly, the direct effect of warming is to reduce the solubility of CO_2, which leads to less uptake of carbon. Secondly, surface warming and in some regions also freshening (Figure S17a) increases stratification. This leads to less uptake of CO_2 because it slows down the removal of carbon from the surface with the circulation. Furthermore, the trends in mixed layer depth and net primary production at the surface are spatially nonuniform (Figure S19c, Figure S14c). In the western North Atlantic STSS, mixed layers get shallower and the net primary production decreases, so that the CO_2 uptake is lowered. In contrast, in the eastern North Atlantic STSS and adjacent parts of the SPSS, mixed

layers are deepening and the net primary production increases, so that the CO_2 uptake increases accordingly. Moreover, the warming causes a reduction in the sea-ice concentration at the transition zone of the North Atlantic SPSS and ICE biome (Figure S18a). As a consequence, a higher ocean surface area is exposed to the atmosphere, which then leads to an increased oceanic CO_2 uptake, given that ΔpCO_2 is generally positive in the North Atlantic. Furthermore, the reduction of sea-ice concentration exposes the ocean surface to winds so that the mixed layer deepens and together with the increased availability of light, this leads to an increase of primary production and thus a positive trend in the CO_2 flux density. The temperature-driven trend in the CO_2 flux integrated over the region where the ice retreats, i.e. the small transition zone of the North Atlantic ICE biome and the North Atlantic SPSS biome, contributes about as much to the global integral as the temperature-driven trend in the CO_2 flux in some much larger biomes, e.g. the South Pacific or Indian Ocean STPS ($0.5\,\mathrm{Tg\,C\,yr^{-1}}$ per yr).

Consistent with the warming in the western Indian Ocean STPS, significant negative trends in the CO_2 flux density, i.e. trends towards more outgassing, are found there (Figure 4.20c). They might be weak in magnitude compared to the northern North Atlantic, but they extend coherently over a large area. Because of that, the regionally integrated temperature-driven trend in the CO_2 flux from the Indian Ocean STPS is larger than that of any other biome ($-0.6\,\mathrm{Tg\,C\,yr^{-1}}$ per yr, Figure 4.18). The negative trends in the western Indian Ocean STPS are not only an effect of the lowered solubility of CO_2, but possibly also related to a temperature-related decline in primary production (Figure S14c). The temperature trends in the CO_2 flux density in the tropics and subtropics in the other oceans are often not significant, but overall negative with more significance in the Atlantic and in the EQU biome of the Pacific (Figure 4.20c).

In contrast to the rest of the globe, the warming calculated as the difference between sim-A and sim-E is weak in the Southern Ocean (Figure 4.21b) and there is even local cooling in sim-A (Figure 4.7b). From the weak warming and local cooling in the Southern Ocean, quite strong local trends with opposite signs in the CO_2 flux density of up to $\pm 0.08\,\mathrm{mmol\,C\,m^{-2}d^{-1}}$ per yr were obtained from the linear offline approximation (Figure 4.7c). Surprisingly, based on the difference between sim-A and sim-E, the trends in the CO_2 flux density surpass $\pm 0.02\,\mathrm{mmol\,C\,m^{-2}d^{-1}}$ per yr hardly anywhere in the Southern Ocean (Figure 4.20c). In fact, temperature-driven trends in the CO_2 flux in the Southern Ocean rather coincide with temperature-driven changes in mixed layer depth (Figure S19c) than with the change of the temperature itself. Furthermore, a quite strong effect of the warming on the trend in the CO_2 flux in the subpolar North Pacific is expected from the offline calculations (Figure 4.7c), but here, the temperature-driven trends separated using sim-E are not even statistically significant.

In summary, in most areas of the globe, the temperature-driven trends in the CO_2 flux are towards slightly more outgassing and relatively homogeneous. The exceptions to this are firstly the North Atlantic ice edge, where the reduction of the sea-ice concentration leads to more CO_2 uptake; and secondly the Eastern North Atlantic STSS biome where the variability in temperature leads to more uptake of CO_2, which is probably related to changes in the circulation or biology.

4.3.3.3 Full climate variability

The impact of full climate variability on the trend in the CO_2 flux density results from the sum of the change and variability in winds, temperature and all other climate forcings together with a nonlinear effect. Overall, the regional distribution is dominated by the effect of winds (compare Figure 4.20a and Figure 4.20b). In the effect of full climate variability on the CO_2 flux, the wind component on the CO_2 flux trend is apparent in several regions: Firstly, more uptake of CO_2 in the Southern Ocean SPSS and more outgassing in the Indian Ocean SPSS sector; secondly, more uptake in large areas of the tropical and subtropical ocean; and thirdly in the North Atlantic and North Pacific mid-latitudes with more uptake in the eastern STSS and more outgassing north-westward in the SPSS. The trends in the CO_2 flux density generated by the full climate variability are mostly more

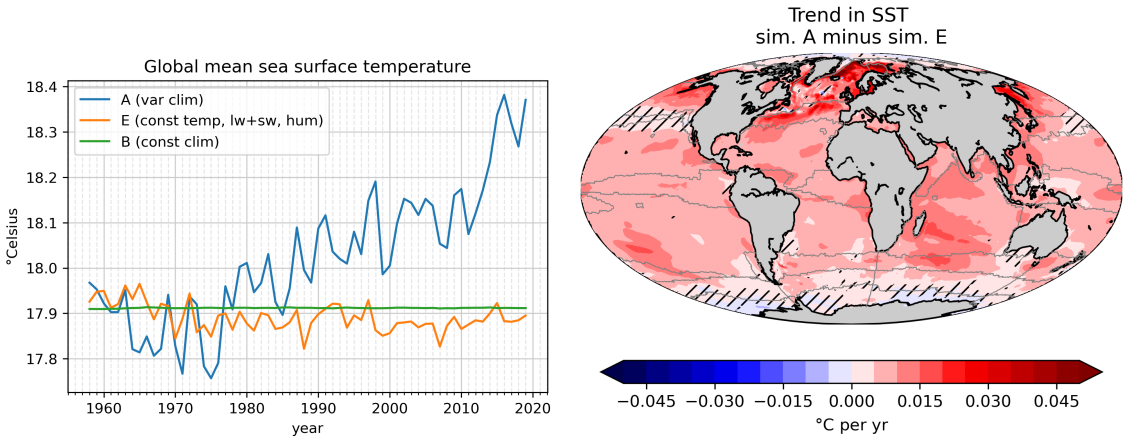

Figure 4.21: Comparison of sea surface temperature in the historical simulation (sim-A) and in sim-E, which is meant to be as close a possible to constant sea surface temperatures.

negative, i.e. towards more CO_2 leaving the ocean, than the effect of winds alone. This is attributed to the impact of global warming and temperature variability, which is uniformly negative globally apart from in the North Atlantic. The part of the climate-driven trends that cannot be explained by the sum of wind- and temperature-induced trends is attributed to the impact of other climate variability and the nonlinear effect which arises from the combination of the variability in winds and temperature. The impact of the other climate variability together with the nonlinear effect is very distinct in the North Atlantic. Here, the other climate variability together with the nonlinear effect attenuate the strong wind-driven effect, that is the trend in the CO_2 flux density towards more outgassing in the western mid-latidude North Atlantic. Furthermore, a distinct temperature-driven effect is attenuated, that is the trend towards more uptake in the North Atlantic eastern STSS. In sum, this leads to a weaker trend towards CO_2 uptake than expected from winds and temperature alone. This means that specifically in the North Atlantic, the climate-induced variability can only be understood as the sum of processes driven by the combined variability in winds and temperature and not by one of the factors alone.

4.3.4 Interannual and decadal variability of the CO_2 flux

In this thesis, the main goal is to analyze and quantify the effect of secular trends in climate variables on the air-sea CO_2 flux. But in the following section, firstly an excursion on the variability of the CO_2 flux caused by interannual fluctuations of the atmospheric partial pressure of CO_2 is presented. Secondly, we throw a glance at the effect of interannual climate variability, namely El Niño and volcanic eruptions, on the CO_2 flux.

The impact of climate on the trend in the globally and annually integrated CO_2 flux amounts to $-6.5\,\mathrm{Tg\,C\,yr^{-1}}$ per yr when averaged over the whole timeseries (Table 4.7). Furthermore, it shows interannual variability, ranging from $+0.4\,\mathrm{Pg\,C\,yr^{-1}}$ in 1964 to -0.6 $\mathrm{Pg\,C\,yr^{-1}}$ in 2001 (Figure 4.22) and has a standard deviation of 0.16 $\mathrm{Pg\,C\,yr^{-1}}$(Table 4.7). Most of the variability is generated by winds, which account for a standard deviation of 0.15 $\mathrm{Pg\,C\,yr^{-1}}$. Temperature fluctuations cause smaller CO_2 flux anomalies with a range of $\pm 0.2\,\mathrm{Pg\,C\,yr^{-1}}$ and a standard deviation of 0.08 $\mathrm{Pg\,C\,yr^{-1}}$. Overall, the temperature-induced variability is only stronger than that induced by winds on the decadal time scale (not shown).

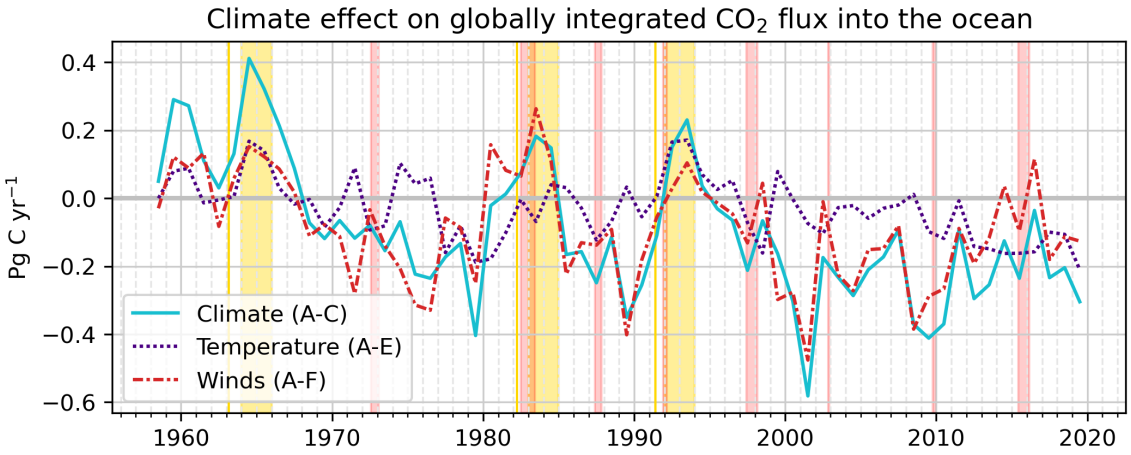

Figure 4.22: Timeseries of the globally integrated CO_2 flux caused by climate change and variability (cyan line) and variability only in winds (red dashed line) or temperature (violet dashed line) separately , calculated by subtracting the CO_2 flux in simulations C, E and F from the CO_2 flux in sim-A (Section 3.1). Positive denotes a flux into the ocean. The red vertical coloring indicates the timing of strong El-Niño events (ONI 1.5) calculated from sim-A. The yellow vertical lines indicate the timing of volcanic eruptions. Furthermore, the first and second year following each volcanic eruption are marked in yellow.

Table 4.7: Trend (Tg C yr^{-1} per yr) and standard deviation (Pg C yr^{-1}) of the globally integrated CO_2 flux separated into different contributing factors through a series of simulations.

	Net (A-B)	Atm. CO_2 (C-B)	Climate (A-C)	Temp. (A-E)	Winds (A-F)
Trend	23.8	30.4	-6.5	-2.3	-2.9
Standard deviation	0.16	0.06	0.16	0.08	0.15

4.3.4.1 Variability of atmospheric CO_2

During the last decades, the partial pressure of atmospheric CO_2 has increased all over the globe, driving an increase in pCO_2^O. But because the oceanic pCO_2 has increased slower than the pCO_2 of air, ΔpCO_2 and with that the air-sea CO_2 flux have gotten more positive. However, pCO_2^A additionally shows decadal and interannual fluctuations relative to its mean growth rate. McKinley et al. (2020) have brought up the question how much of the decadal variability in air-sea CO_2 flux can be explained by the variability of pCO_2^A. To analyze this, sim-C is the most suitable simulation, because all other factors apart from the atmospheric CO_2 concentration are held constant.

Because the ocean has a regionally heterogeneous sensitivity to changes in ΔpCO_2, the global mean ΔpCO_2 is more straight-forward to interpret when ΔpCO_2 is weighted by the gas transfer coefficient ($\alpha \cdot K_w$) for the averaging. Thereby, areas with a low gas transfer coefficient, which consequently are less sensitive to any change in the pCO_2 gradient, are weighted less; and areas with a high gas transfer coefficient, which therefore react more strongly to a change in the pCO_2 gradient, are weighted more heavily (see also Section 7.3). The annual timeseries of the weighted global mean ΔpCO_2 is highly correlated to the globally integrated CO_2 flux in sim-C (r=0.998 for sim-C, which doesn't include any climate variability; and r=0.67 for sim-D, which includes climate variability).

The weighted global means of pCO_2^A and pCO_2^O both increase at accelerating growth rates[8] (Figure 4.23). Hofmann et al. (2009) state that the growth of atmospheric CO_2 in the last decades was exponential. A second order polynomial fit of pCO_2^A mimics the growth reasonably well (Figure 4.23). To separate the interannual and decadal variability in pCO_2^A and pCO_2^O from the long-term growth, pCO_2^A and pCO_2^O were detrended by removing a polynomial fit (Figure 4.24a). The growth of pCO_2^O follows the growth of pCO_2^A, but at reduced growth rates and sometimes with a lag of up to one year, so that the peaks in the growth rate are smoothed in pCO_2^O compared to pCO_2^A (Figure 4.24a). Consequently, ΔpCO_2 increases mostly when the growth rate of pCO_2^A increases and decreases when the growth rate of pCO_2^A decreases, sometimes delayed by one year (compare Figure 4.24b and Figure 4.24a). However, there are differences in the strength of the increase and decrease, so that the lowest anomaly in the growth of pCO_2^A is in the 1990s (1993), whereas the ΔpCO_2 anomalies reach smaller values in other decades (e.g. 1965, 2001 or 2009); and the maximum of the ΔpCO_2 anomaly is in the 1980s (1988), whereas the anomaly of the pCO_2^A growth has multiple maxima from the 1970s to the end of the timeseries in 2019.

The interannual variability in ΔpCO_2 explains the annual anomalies of the CO_2 flux in sim-C almost entirely (compare cyan line in Figure 4.24b and Figure 4.24c). The anomaly of the CO_2 flux in the historical simulation (sim-A) is the sum of the variability generated by fluctuations in the atmospheric pCO_2^A (sim-C) and climate variability (sim-D) minus the model drift (sim-B) with a nonadditive effect due to the impact of climate variability on the anthropogenic carbon flux (Figure 4.24c). The standard deviation of the CO_2 flux anomaly caused by climate variability alone (sim-D) is $0.16\,\mathrm{Pg\,C\,yr^{-1}}$, meaning that climate variability explains most of the historical interannual variability. In contrast, the part generated by the interannual variability in the growth rate of atmospheric CO_2 (sim-C) is smaller with a standard deviation of $0.06\,\mathrm{Pg\,C\,yr^{-1}}$. The remaining non-additive part has a standard deviation of $0.03\,\mathrm{Pg\,C\,yr^{-1}}$.

During the 1990s, the oceanic uptake in sim-C stagnates due to anomalously low growth in the atmospheric pCO_2^A as proposed by McKinley et al. (2020). In particular, the period from 1988-1993 is striking with a strong decline in the anomaly of the growth rates of pCO_2^A and pCO_2^O with corresponding decline in the anomaly of ΔpCO_2 and in the anomaly of the CO_2 flux in sim-C (Figures 4.24a to 4.24c) followed by a recovery in the later years of the 1990s. As described in McKinley et al. (2020), in the simulation which includes a variable climate (sim-A), a local maximum in the CO_2 uptake following the eruption of Pinatubo in 1992 more than compensates for the drop in the CO_2 flux in 1993 expected from sim-C (Figure 4.24c) even though the applied atmospheric

[8] "growth rate" of pCO_2^A and pCO_2^O: the time derivative, that is $\frac{\partial}{\partial t} pCO_2^{O/A}$

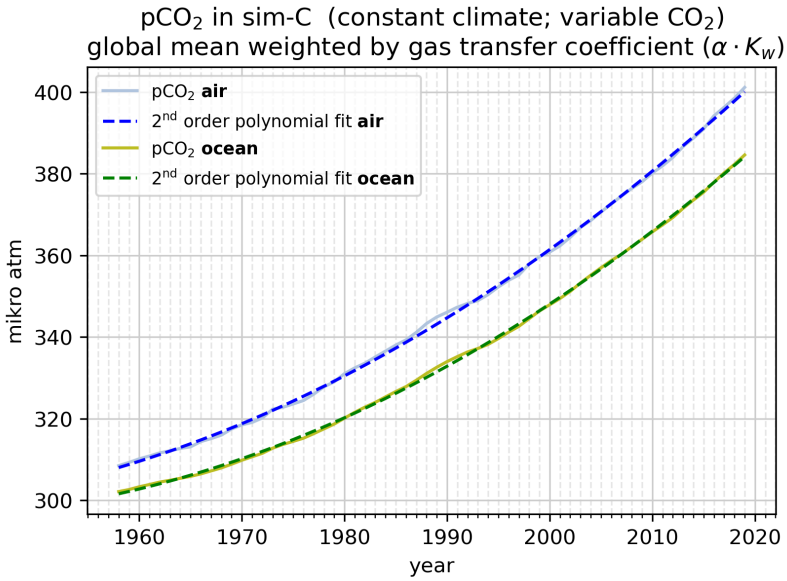

Figure 4.23: Timeseries of the globally weighted average of pCO_2^O (green line) and pCO_2^A (blue line): For the averaging, pCO_2^O and pCO_2^A are weighted by the mean gas transfer coefficient at each grid cell. The dashed lines are 2nd order polynomial fits. pCO_2^A is calculated offline from pCO_2^O and ΔpCO_2.

model forcing does not include the full temperature effect of the eruption (Section 4.3.4.3). In the years 2000 and 2001, the CO_2 flux in sim-A, sim-D and sim-E drops due to a wind-driven effect (Figures 4.3 and 4.22). This results in a period with an average decline in the CO_2 flux from 1993 to 2001 characterized by the impact of the Pinatubo eruption in the beginning and a wind-driven effect towards the end. Furthermore, there is a decline in the anomaly of the CO_2 flux from 1993-1998 in sim-A and sim-D (Figure 4.24c). McKinley et al. (2020) interpret the decline of the CO_2 flux in this period as a delayed effect of the decline in the anomalous atmospheric pCO_2^A from 1988-1993. In contrast, in FESOM-REcoM, the decline in the CO_2 flux from 1993-1998 seems to be purely climate-driven as it is detectable equally well in the simulation at constant atmospheric CO_2 (sim-D, Figure 4.24c). In conclusion, climate variability is the most important parameter to explain the interannual variability in the CO_2 flux. Still, the impact of interannual and decadal variability in atmospheric CO_2 accounts for an important part; yet in FESOM-REcoM, it does not have a delayed effect in the 1990s as proposed by McKinley et al. (2020).

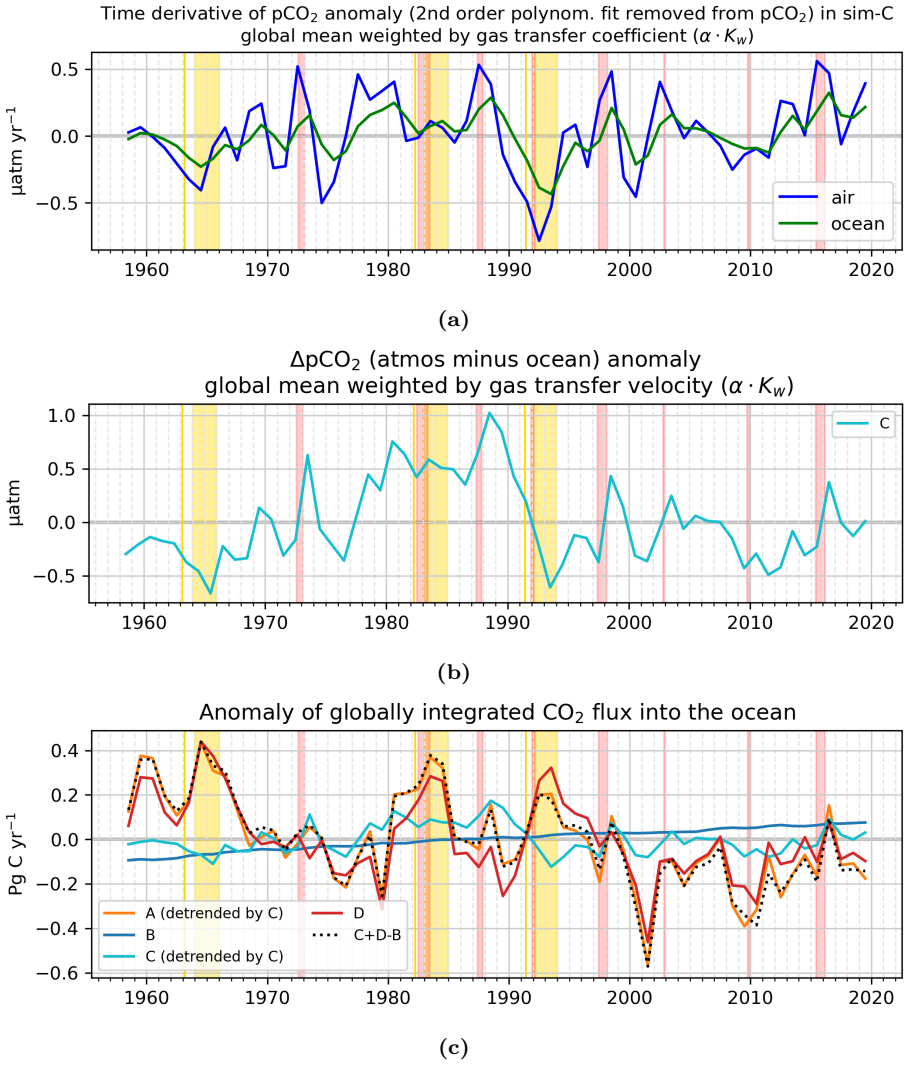

Figure 4.24: (a) Timeseries of the growth rate (time derivative) of the pCO_2^O (green) and pCO_2^A (blue) anomalies $\left(\frac{\partial}{\partial t}\left(pCO_{2,ano}\right)\right)$ in the simulation with variable atmospheric CO_2 only (sim-C). To obtain the anomalies, a 2nd order polynomial fit was removed from pCO_2 (see Figure 4.23). For the global average, pCO_2 was weighted by the gas transfer coefficient at each grid cell. The time derivative was calculated by finite central differences. (b) Timeseries of the anomaly of the globally averaged ΔpCO_2 in sim-C. To obtain the anomaly, a linear fit was removed. For the global average, ΔpCO_2 was weighted by the gas transfer coefficient at each grid cell. (c) The anomalies of the globally integrated CO_2 flux in simulations A, B, C and D (orange, dark blue, light blue and red line, respectively). For the simulations with rising atmospheric CO_2 concentrations (A and C), a linear fit was removed to obtain the anomaly. The dotted line is the sum of the CO_2 flux anomalies from the simulations C+D-B, i.e. variability in atmospheric CO_2 only and variability in climate only minus the drift. The vertical red coloring indicates the timing of strong El Niño events in the historical simulation (sim-A). The yellow vertical lines indicate the timing of volcanic eruptions and the yellow vertical coloring marks the 2-year-period after each eruption.

4.3.4.2 El Niño

Globally, the El Niño-Southern Oscillation (ENSO) is the most important mode of year-to-year climate variability (Schwalm et al., 2011). Therefore, it seems likely that ENSO might also affect the global variability in the CO_2 flux. Here, periods with an Oceanic Nino Index (ONI 3.4) over 1.5 based on the sea surface temperature in sim-A are examined. The index is based on the three month running mean of the sea surface temperature anomalies in the Niõ 3.4 region (5°N-5°S, 120-170°W) (NOAA, 2021a). The ONI 3.4 index in sim-A correlates with the ONI 3.4 index from the NOAA Climate Prediction Center with a correlation coefficient of r=0.95 (NOAA, 2021a). Based on this, the detected years with strong El Niño events are listed in Table 4.8:

Table 4.8: Years with strong El Niño events defined as ONI 3.4 $\geq$ 1.5 in FESOM-REcoM sim-A compared to the index from NOAA (2021a). In 2002/03, the index was $\geq$ 1.5 only for a single month in October 2002.

Sim-A	NOAA
-	1957/58
-	1965/66
1972/73	1972/73
1982/83	1982/83
1987/88	1987/88
1991/92	1991/92
1997/98	1997/98
2002/03	-
2009/10	2009/10
2015/16	2015/16

Multiple effects of ENSO on the global carbon cycle have been described in the literature, e.g., due to the sea surface temperature anomaly, changes of the ocean circulation and the anomaly of atmospheric CO_2 (Schwalm et al., 2011). In FESOM-REcoM, the effects of ENSO on air-sea CO_2 fluxes are not the same across El Niõ events. Firstly, the global mean sea surface temperature increases during El Niño events. In sim-A, the average warming is 0.13 °C during strong El Niño events, and the strongest warming occurs in the East Pacific EQU region (Figure 4.25a), where the characteristic equatorial cold tongue warms (Collins et al., 2010). In contrast, the warm pool in the western tropical Pacific and regions in the north and south subtropical Pacific experience cooling. The effect of the temperature anomaly during strong El Niños on the CO_2 flux was calculated using the temperature sensitivities of the CO_2 flux based on sim-A using Equation (3.30), but applying it on the temperature anomaly during strong El Niño events instead of on the long-term temperature trend. Because of the increasing surface ocean pCO_2^O in sim-A, the sensitivity of the CO_2 flux to temperature increases over time (not shown). During strong El Niños, a more negative CO_2 flux in the East Pacific EQU biome and a more positive CO_2 flux in the west Pacific are expected due to the regional changes in temperature (Figures 4.25a and 4.25b). Averaged over all El Niño events in the simulation period, the global effect of the El Niño temperature anomaly is an increased outgassing of approximately $-0.21\,\mathrm{Pg\,C\,yr^{-1}}$.

Secondly, ENSO is associated with changes in circulation. The anomaly of the CO_2 flux during strong El Niño events in sim-A is characterized by a strong reduction of outgassing in the upwelling system off the coast of Peru, which dominates over the opposite temperature effect in the same region (Figures 4.25c and 4.26). Thus, the reduction of outgassing must be attributed to the changes in circulation. As shown in Figure 4.1, the mean CO_2 flux off the Peruvian coast features the strongest outgassing flux of carbon per area worldwide. In fact, the Peruvian upwelling system dominates the CO_2 flux of the East Pacific EQU and South Pacific STPS regions, which together contribute almost half of the globally integrated outgassing of CO_2 (see Figure 4.2). This is in agreement with

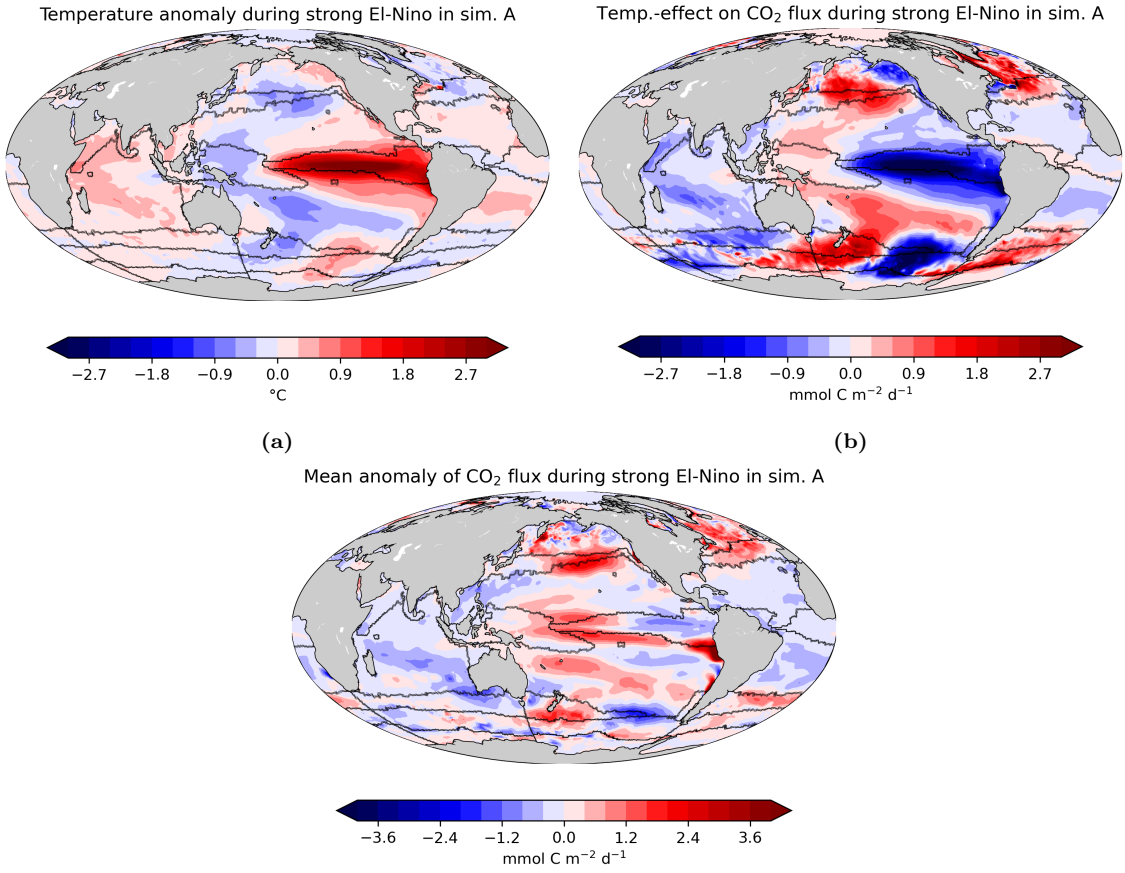

Figure 4.25: (a) Mean anomaly of the detrended and deseasonalized sea surface temperature during months with an ONI 3.4 $\geq$ 1.5 in the historical simulation (sim-A). (b) Estimate for the effect on the CO_2 flux generated by the temperature anomaly. (c) Mean anomaly of the detrended and deseasonalized CO_2 flux during during months with an ONI 3.4 $\geq$ 1.5.

observations, which show that in the Peruvian upwelling system, carbon is transported from the depth to the surface (Friederich et al., 2008). The waters brought to the surface warm rapidly and release carbon. While in other upwelling systems, some of the carbon from depth is taken up by biology, biology in the Peruvian upwelling system is limited by iron and nitrate availability and cannot fully compensate for the upwelling of carbon (Friederich et al., 2008). During El Niños, the upwelling of carbon is suppressed, resulting in less outgassing (Chatterjee et al., 2017). A regression of the CO_2 flux density on the ONI 3.4 confirms that the impact of ENSO on the CO_2 flux is largest off the Peruvian coast (not shown), whereas a correlation of the CO_2 flux density with the ONI 3.4 reveals the highest correlation in the western and central tropical Pacific (not shown). Here, a $\subset$-shaped region with more CO_2 uptake during positive El Niño phases surrounding the east Pacific EQU biome to the northwest, west and south appears (Figure 4.25c).

Thirdly, the anomaly of atmospheric CO_2 can be both positive or negative during El Niño events because the response of the land ecosystem e.g. via droughts and forest fires is complex (Schwalm et al., 2011). In sim-A, the global mean pCO_2^A drops by some 1/10 of µatm during most, but not all strong El Niño events in comparison to before and after the event (not shown). Given the global mean sensitivity of the integrated CO_2 flux to changes in pCO_2^A, which was calculated [9] to be $0.23\,\mathrm{Pg\,C\,yr^{-1}}$ per µatm, the effect of this on the global CO_2 flux is small (around 0.02-0.1 $\mathrm{Pg\,C\,yr^{-1}}$).

In sim-A, the globally integrated anomaly of CO_2 flux during strong El Niños is different for each event (not shown). The main reason for this is the underlying decadal and interannual climate variability unrelated to El Niños. Compared to the range of the interannual variability in the global CO_2 flux, the global temperature effect and the effect of upwelling in the east Pacific EQU biome caused by ENSO are one magnitude smaller. Furthermore, even the regional effect is not uniform. For example, during the 2009/2010 El Niño event, more outgassing of CO_2 off the Chilean coast appeared instead of more uptake off the Peruvian coast.

In summary, the detectable effect of El Niño on the CO_2 flux is limited to the equatorial Pacific. Whereas an increased outgassing of CO_2 during El Niño events is expected due to the increase in sea surface temperature, it turns out that the dominant effect is less outgassing of CO_2 off the coast of Peru related to suppressed upwelling during El Niño events. This effect is one magnitude smaller than the range of the interannual variability in the global CO_2 flux.

[9] using $\frac{\partial F_{\mathrm{surf}}}{\partial (\mathrm{pCO_2^A})} = k_w \cdot \alpha$ which follows from Equation (3.16)

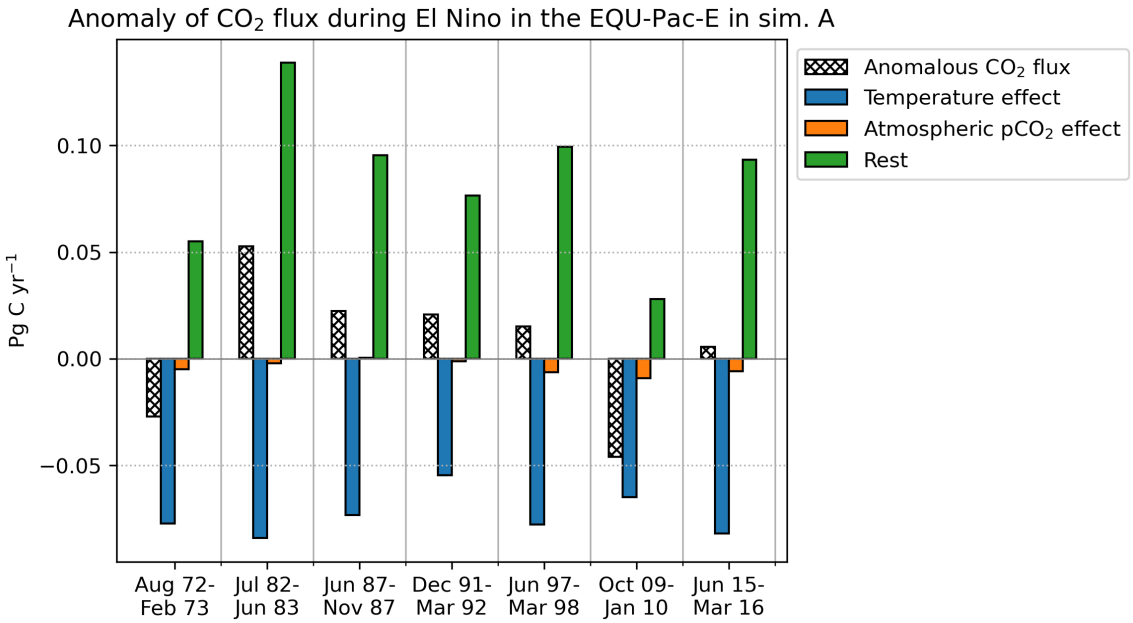

Figure 4.26: The net anomaly of the integrated CO_2 flux in the East Pacific EQU biome (hatched bars), the effect of the temperature anomaly (blue) and the effect of pCO_2^A anomaly (orange) on the CO_2 flux for individual El Niño events with an ONI 3.4 $\geq$ 1.5. The residual (green) is attributed to changes in circulation.

4.3.4.3 Volcanic eruptions

Two main mechanisms are proposed in the literature by which volcanic eruptions have an effect on the air-sea CO_2 flux: Firstly, the temperature effect; secondly, the effect of changes in the ocean circulation following the volcanic perturbation (Eddebbar et al., 2019). After an eruption, the reduction of shortwave radiation through volcanic aerosol scattering should lead to immediate cooling (McKinley et al., 2020). However, no such reduction of the shortwave radiation is seen in the forcing applied to the simulations used here because volcanic aerosols are not included in the data assimilation scheme for the radiative transfer in the JRA-55 reanalysis (JMA, 2021). Nevertheless, the globally integrated CO_2 flux in sim-A and sim-D has positive anomalies, that is more oceanic CO_2 uptake, during the 1st and 2nd year following the eruption year (i.e. 'year zero') of Agung, El Chichón and Pinatubo (Table 4.9):

Table 4.9: Anomalies of globally integrated CO_2 flux in $Pg\,C\,yr^{-1}$ for the first two years following the eruption year of Agung, El Chichón and Pinatubo, respectively. See also the yellow coloring in Figure 4.22.

	Agung (1963)	El Chichón (1982)	Pinatubo (1991)
sim-A	0.22	0.31	0.23
sim-D	0.30	0.25	0.31

These anomalies of 0.2-0.3 $Pg\,C\,yr^{-1}$ of the global mean CO_2 flux are similar in magnitude and duration to the ones described by Eddebbar et al. (2019), who detected the anomalies in the CO_2 flux in months 12-36 following the eruptions with an enhanced CO_2 uptake of 0.3 $Pg\,C\,yr^{-1}$. Eddebbar et al. (2019) propose that one year after the peak of the eruption, the ocean reacts with an El Niño-like response during which upwelling of carbon-rich waters is suppressed in the tropical Pacific, which is what appears to be happening in REcoM as well (Figure 4.27). This response is triggered

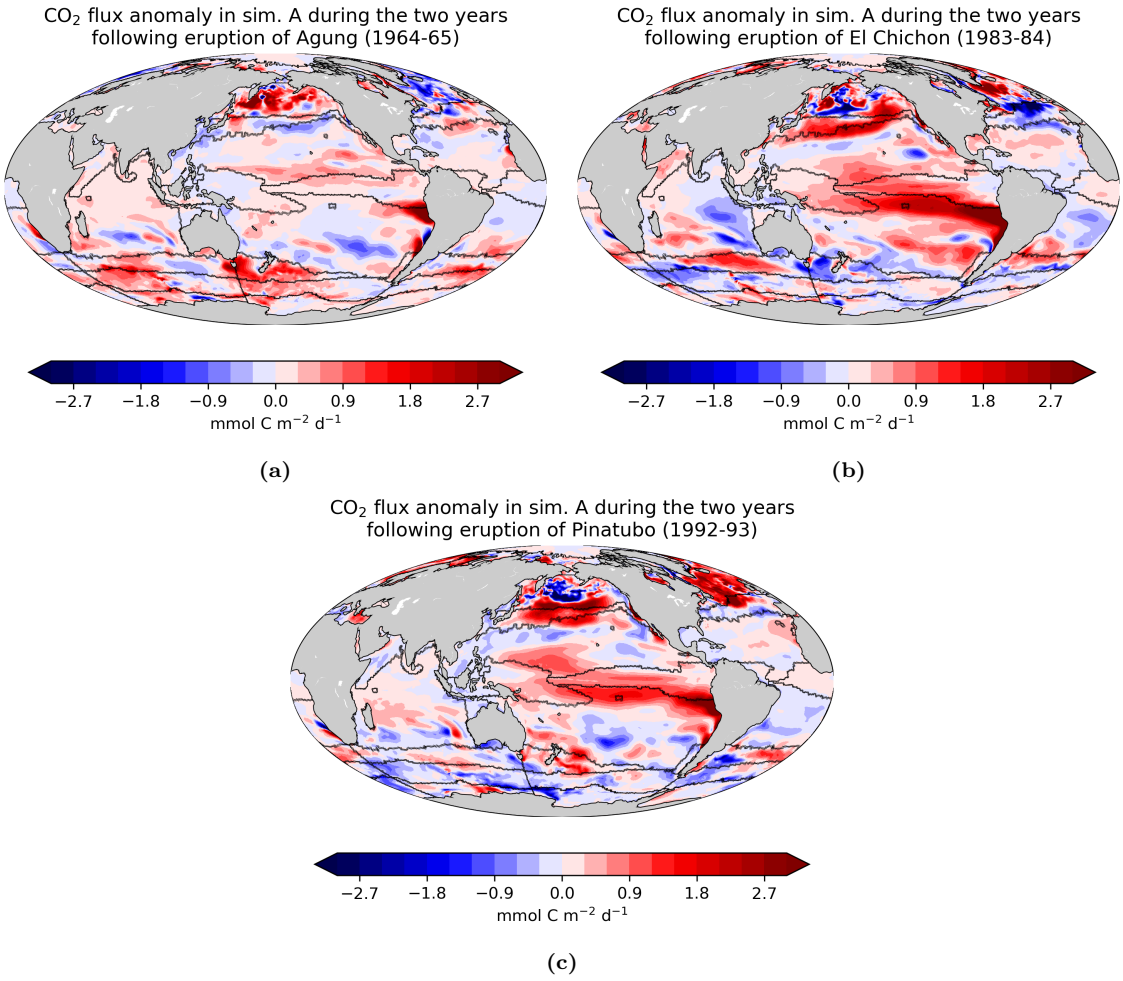

Figure 4.27: Mean anomaly of the CO_2 flux during the 1st and 2nd year following the year of the volcanic eruption ('0th year') in simulation (sim-A). (a) Following the eruption of Agung in 1963. (b) Following the eruption of El Chichón in 1982. (c) Following the eruption of Pinatubo in 1991.

by changes in the temperature and wind forcing. The differences between sim-A and sim-D result from the different atmospheric CO_2 growth rate in sim-A. In sim-A, the eruptions of Agung and Pinatubo both fell into periods of decreasing atmospheric pCO_2^A growth rates (Figure 4.24a) which reduced the anomaly of the oceanic carbon flux (Figure 4.24c, Table 4.9), whereas the eruption of El Chichón was associated with a stronger oceanic CO_2 uptake anomaly in sim-A than in sim-D, possibly because it fell into a decade of stronger than usual growth of atmospheric CO_2 in the 1980s.

Chapter 5

Discussion

5.1 Global CO_2 flux and trends

During the 1958-2019 period (62 years), the ocean took up $1.85\,\mathrm{Pg\,C\,yr^{-1}}$ of atmospheric CO_2 on average in FESOM-REcoM (Table 4.1). The ocean carbon sink has increased with a trend of $23.8\,\mathrm{Tg\,C\,yr^{-1}}$ per yr (after subtracting the model drift). Without climate variability and due to rising atmospheric CO_2 concentrations alone, this increase would have been $30.4\,\mathrm{Tg\,C\,yr^{-1}}$ per yr. Thus, climate variability has attenuated the trend in the ocean carbon sink by $-6.5\,\mathrm{Tg\,C\,yr^{-1}}$ per yr or 21%, thereby reducing ocean acidification but strengthening the greenhouse effect as the ocean removed less CO_2 from the atmosphere in a changing climate.

Table 5.1: Trend in the CO_2 flux separated into parameters by a series of simulations (Section 3.1) in comparison to the results in Le Quéré et al. (2010). Positive trends denote an increase in the oceanic carbon sink over the indicated period.

[Pg C yr^{-1} per yr]	LeQuéré (2010) 1981-2007	FESOM-REcoM 1981-2007	FESOM-REcoM 1958-2019
Historical w/o drift (A-B)	12	15.8	23.8
Atmospheric CO_2 (C-B)	32	25.9	30.4
Climate (A-C)	-20	-10.1	-6.5
Winds	-12	-8.9	-2.9
	Temperature sensitivity of carbon cycle switched off.	Temperature sensitivity of carbon cycle switched on.	
Temperature	-4	-0.6	-2.3
	Temperature effect only on the carbon cycle.	Full temperature effect (including carbon cycle, circulation, ...)	
Other	-3	-0.6	-1.3
	Temperature effect on everything but on the carbon cycle, freshwater fluxes, non-additive part.	Freshwater fluxes, non-additive part.	

5.1.1 Comparison with previous studies

Previously, the impact of climate change and variability on the CO_2 flux trend for the time period 1981-2007 (26 years) was estimated by Le Quéré et al. (2010) using another global ocean biogeochemistry model. Le Quéré et al. (2010) found a climate-induced trend in the CO_2 flux of $-20\,\mathrm{Tg\,C\,yr^{-1}}$ per yr which corresponds to an offset of 63% of the trend due to the rising atmospheric CO_2 (Table 5.1). Using the same setup of simulations as Le Quéré et al. (2010) with the model FESOM-REcoM, one obtains a higher net trend in the global CO_2 flux during this shorter time period ($15.8\,\mathrm{Tg\,C\,yr^{-1}}$ per yr in FESOM-REcoM compared to $12\,\mathrm{Tg\,C\,yr^{-1}}$ per yr). In agreement with Le Quéré et al. (2010), the FESOM-REcoM simulations suggest a reduction of the trend in the CO_2 flux due to climate change and variability. However, the magnitude of the components of the trend in the CO_2 flux is quite different between the results in Le Quéré et al. (2010) and those presented here. In FESOM-REcoM, both components – that is the component due to the increase in atmospheric CO_2 and the component due to climate change and variability – are smaller (Table 5.1). In particular, the effect of climate change and variability on the trend in the CO_2 flux in FESOM-REcoM is only $-10.1\,\mathrm{Tg\,C\,yr^{-1}}$ per yr between 1981-2007, corresponding to an offset of 40% of the trend due to the rising atmospheric CO_2 concentrations. Some of the climate-induced trend in the CO_2 flux detected during the period from 1981-2007 is probably due to the eruption of El Chichón towards the beginning in 1982 and due to a wind-driven anomalous drop in the CO_2 flux later on in the year 2001, suggesting a smaller trend on longer timescales. Indeed, by extending the time period to 1958-2019 (62 years), the climate-driven trend in the CO_2 flux becomes smaller.

Furthermore, Gruber et al. (2019) have quantified the cumulative anthropogenic CO_2 flux between 1994 and 2007 using an observation-based approach and a back-of-the-envelope estimate for the impact of climate variability on the CO_2 flux. During this period, the cumulative global

Table 5.2: The cumulative CO_2 uptake (Pg C) from 1994-2007 in the historical simulation, the component driven by climate variability and the component driven by the increase in atmospheric CO_2 concentration compared to the observation-based estimate in Gruber et al. (2019)

	FESOM-REcoM	Gruber et al. (2019)
Atmospheric CO_2	26	34
Climate	-3	-5
Historical	23	29

CO_2 uptake in FESOM-REcoM was smaller (23 Pg C) than Gruber et al.'s (2019) estimate (29 Pg C, Table 5.2). In FESOM-REcoM, 10% of the cumulative uptake of anthropogenic carbon was offset by an outgassing of natural carbon during that period, whereas it was 15% according to Gruber et al. (2019). All in all, the uptake of anthropogenic carbon and the climate-induced outgassing of natural carbon are apparently smaller in FESOM-REcoM compared to previous estimates.

5.1.2 Effects of climate variability on the natural and anthropogenic CO_2 flux

Through a series of simulations, the effects of climate change and variability on the CO_2 flux between 1958-2019 were separated into their natural and anthropogenic components. The effect of climate change and variability on the natural CO_2 flux was dominant. On average, climate change and variability led to more outgassing of natural CO_2 ($-0.09\,\mathrm{Pg\,C\,yr^{-1}}$, Table 4.5) and less uptake of anthropogenic CO_2 ($-0.01\,\mathrm{Pg\,C\,yr^{-1}}$). An effect towards more outgassing or equivalently less uptake is expected for example from global warming. However, climate change and variability also caused *a trend* towards more uptake of anthropogenic CO_2 during that period ($0.6\,\mathrm{Tg\,C\,yr^{-1}\,per\,yr}$), possibly corresponding to an increase in the downward transport of anthropogenic CO_2 through a climate-driven acceleration of the upper ocean overturning circulation (DeVries et al., 2017). To explain why the impact of climate change and variability is about one order of magnitude larger on the flux of natural CO_2 than on the flux of anthropogenic carbon in FESOM-REcoM, we draw on two measures: Firstly, about 98% of the dissolved inorganic carbon at the ocean surface was natural carbon [1] during the simulated period. The fraction of anthropogenic carbon is even smaller at depth. Thus, changes in the circulation and thus in the transport of sDIC affect primarily the fluxes of natural carbon. This is in agreement with Gruber et al. (2019) finding no indication that climate variability between 1994-2007 had an impact on the globally integrated uptake of anthropogenic carbon.

However, the offline approximation also points to a different line of argumentation. As pCO_2^O is not a linear function of sDIC, pCO_2^O at the ocean surface increased by almost a third through anthropogenic carbon during the simulated period. Because the effect of temperature, salinity and sAlk on the CO_2 flux depends rather on pCO_2^O than on the sDIC concentration (Equations (3.27), (3.40) and (3.45)), these drivers might have a non-negligible impact on the flux of anthropogenic CO_2. Accordingly, the effect of temperature, salinity and sAlk on the trend in the flux of anthropogenic CO_2 accounts for more than 25% of the historical trend caused by these drivers during the simulated period (Table 4.3). This is closer to DeVries et al.'s (2017) data-assimilating estimate, according to which the effect of decadal climate variability on the anthropogenic CO_2 flux accounted for 10-20% of the climate effect on the total CO_2 flux in the 1990s and 2000s.

The separation between climate-induced variability in the anthropogenic and natural carbon fluxes is further complicated by interactions between both components. For instance, the Revelle factor γ_{DIC} increases in the presence of anthropogenic carbon (see Section 7.2), which in turn affects both the natural and the anthropogenic component of the CO_2 flux. Yet, in total, the effect of

[1] Natural DIC: $1978\,\mathrm{mmol\,C\,m^{-3}}$ (sim-D)
Anthropogenic DIC: $43\,\mathrm{mmol\,C\,m^{-3}}$ (sim-A minus sim-D)

climate change and variability during the simulated period is to increase the outgassing of natural CO_2.

5.2 Compensating and competing effects

The net effect of climate change and variability on the trend in the CO_2 flux was reduced by competing and compensating processes. According to the offline approximation based on sim-D, the climate-driven trend in the global CO_2 flux would have been almost $30\,\mathrm{Tg\,C\,yr^{-1}}$ per yr in the absolute if all factors had worked in the same direction in FESOM-REcoM during the simulated time period (Figure 4.5). However, as this is not the case, the net trend in the CO_2 flux was only $-4.3\,\mathrm{Tg\,C\,yr^{-1}}$ per yr.

In the following, these competing effects will be synthesized. I will discuss the contributions of different climate factors on the ocean carbon sink from two approaches: Firstly, using model experiments with the full and a subset of the climate forcing fields; and secondly applying offline diagnostics (linear approximation) on simulations with the full climate forcing.

5.3 The effect of increasing temperatures on the trend in the CO_2 flux

According to the linear approximation that was made to estimate the contribution of several variables to the climate-induced trend in the global CO_2 flux, the largest effect was caused by the increasing temperatures, namely a trend towards more outgassing of $-18.7\,\mathrm{Tg\,C\,yr^{-1}}$ per yr due to a warming-related reduction of the solubility of CO_2 in the historical simulation (Equation (3.27)). When I separated the effect of global warming on the trend in the CO_2 flux using a simulation without global warming, the effect turned out much smaller ($-2.3\,\mathrm{Tg\,C\,yr^{-1}}$ per yr).

In relation to other climate variables affecting the trend in the CO_2 flux, the temperature variability is particularly important at low latitudes, that is in the EQU, STPS and the STSS biome. Both the offline approximation and the simulation suggest that here, the temperature is the most important climate factor (Figures S27 to S29). The STPS accounts for at least half of the global temperature effect due to its size. In contrast, other climate factors are dominant at high latitudes, that is in the Southern Ocean SPSS, North Atlantic SPSS and ICE biomes (Figures S24 to S26).

According to the linear approximation, the temperature effect on the trend in the CO_2 flux density is largest in the STSS and SPSS biomes (Figure 4.7c). Still, the effects of sDIC and sAlk on the trend in the CO_2 flux density are even larger than the effect of temperature in the STSS and SPSS biomes, so that the temperature effect is less important in relation to other parameters there. In contrast to the linear approximation, the simulated temperature effect shows little latitudinal dependence but deviates in the North Atlantic from the rest of the globe (Figure 4.20c).

5.3.1 Negative feedback in the CO_2 flux

The simulated temperature effect was smaller than the linear approximation because it is the remainder of the sum of two opposing effects: On the one hand, the increasing sea surface temperatures reduced the solubility of CO_2 and thus led to more outgassing of CO_2. On the other hand, the surface sDIC concentration was reduced by $-0.07\,\mathrm{mmol\,C\,m^{-3}}$ per yr which led to less outgassing of CO_2 (Figure S31b). These two processes are linked through a negative feedback (Figure 5.1). Any change in temperature affects pCO_2^O (Equation (3.27)). Similarly, changes in alkalinity and salinity affect pCO_2^O (Equations (3.40) and (3.45)), but during the time period considered, the temperature trend was the most important factor. As a consequence of global warming, pCO_2^O increases, which leads to more outgassing of CO_2. In turn, the enhanced air-sea flux lowers the mixed layer sDIC

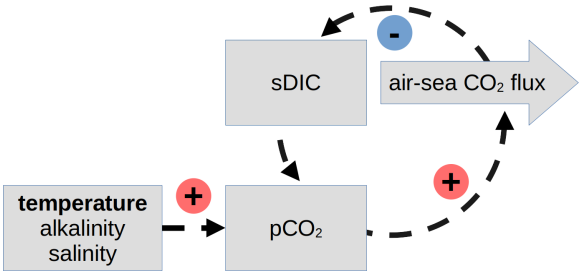

Figure 5.1: Changes in temperature, alkalinity and salinity affect pCO_2^O, which in turn affects the CO_2 flux. Changes in the CO_2 flux affect the sDIC concentration, thus partly compensating for the disturbance in pCO_2^O.

concentration and consequentially, pCO_2^O decreases, thus partly compensating for the thermally-driven increase in pCO_2^O. This negative feedback reduces the thermally-driven trend towards more outgassing of CO_2 compared to what is expected from a warming at constant sDIC concentrations.

The strength of the feedback depends on how quickly warmed-up water of the mixed layer with a reduced sDIC concentration is replaced by upwelling of unmodified water with a sDIC concentration that has not yet been affected by the warming. The more unmodified water is transported to the surface and subsequently warms, the stronger is the thermally-driven outgassing and the less important is the feedback. This might be one of the reasons why the temperature effect is particularly important in the tropics, where unmodified waters are brought to the surface by equatorial upwelling. If all of the difference between the linear approximation and the simulated effect of global warming on the trend in the global CO_2 flux was attributed to the feedback, it could account for a reduction of the temperature-related outgassing by almost 90% in FESOM-REcoM. However, other processes provoked by the temperature-related model forcing additionally play a role in explaining the difference. Clearly, the reduction of sDIC was the most important factor compensating for the reduced solubility of CO_2. Mixed layer sDIC might have been altered by thermally-driven changes in the circulation or biology besides the changes in the air-sea CO_2 flux which are attributable to the feedback. Furthermore, the warming-driven decrease of sea-ice cover and the temperature effect on alkalinity add to the difference between the linear approximation and the simulated temperature effect.

5.3.2 Comparison with Le Quéré et al. (2010)

The estimate for the temperature effect on the trend in the CO_2 flux by Le Quéré et al. (2010) is much larger ($-4\,\mathrm{Tg\,C\,yr^{-1}}$ per yr during 1981-2007) than the estimate for the same time period in the FESOM-REcoM simulation ($-0.6\,\mathrm{Tg\,C\,yr^{-1}}$ per yr, Table 5.1). Besides differences in the model code, a reason for the discrepancy might be that Le Quéré et al. (2010) performed a model experiment in which only the temperature effect on the carbon cycle was switched off, thus not including any thermally-driven changes in the circulation and biology in their estimate for the temperature effect.

5.4 The effect of variability in winds on the trend in the CO_2 flux

According to the series of simulations, the variability of winds had a larger effect on the trend in the global CO_2 flux ($-2.9\,\mathrm{Tg\,C\,yr^{-1}}$ per yr) than temperature during the 1958-2019 time period ($-2.3\,\mathrm{Tg\,C\,yr^{-1}}$ per yr, Table 5.1). Most of the simulated wind effect arose from changes in the surface sDIC concentration. Through the variability in the wind forcing, the global mean surface sDIC concentration increased by $0.01\,\mathrm{mmol\,C\,m^{-3}}$ per yr, which is mostly ascribed to wind-driven changes in the transport of natural carbon with the circulation (Figure S31b, Section 4.3.3.1). Using

a linear approximation to estimate the effect of the wind velocity on the gas transfer coefficient ($\alpha \cdot k_w$), it turned out that the trends in the wind velocity induced a trend towards more uptake of $2.1\,\mathrm{Tg\,C\,yr^{-1}}$ per yr in the global CO_2 flux. Among all the drivers of the trend in the CO_2 flux which were affected by the wind forcing – e.g. trends in the mixed layer sDIC concentration, the wind-driven transport of freshwater with sea-ice and trends in the sea surface temperature due to changes in the wind-driven circulation – the effect of trends in the wind velocity on the gas transfer coefficient was comparatively small. This is in agreement with Le Quéré et al.'s (2007) statement that the effect of wind-driven changes of the gas transfer coefficient on the CO_2 flux is much smaller than the effect of winds on the ocean circulation and thereby on the CO_2 flux.

Significant wind-related trends in the CO_2 flux were only found in about 47% of the ocean (Figure 4.20b) in the FESOM-REcoM simulation. Trends in the wind velocity as well as wind-driven trends in the CO_2 flux were regionally heterogeneous, which is summarized in the following:

Southern Ocean ICE biome According to the linear approximation, the effect of winds was small (less than $\pm 1\,\mu\mathrm{mol\,C\,m^{-2}d^{-2}}$ per yr), whereas strong wind-driven trends towards more outgassing (-6 to $-7\,\mu\mathrm{mol\,C\,m^{-2}d^{-2}}$ per yr) in the Atlantic and Indian sector were found using a series of simulations, possibly related to changes in the freshwater transport with sea ice.

Southern Ocean SPSS According to the linear approximation, the effect of winds was notably towards more uptake of CO_2 (3 to $6\,\mu\mathrm{mol\,C\,m^{-2}d^{-2}}$ per yr) because the increase in westerly winds enhanced the mean CO_2 flux from the atmosphere into the ocean, whereas strong wind-driven trends towards more outgassing in the Atlantic and Indian sector (-8 and $-22\,\mu\mathrm{mol\,C\,m^{-2}d^{-2}}$ per yr, respectively) were found using a series of simulations probably related to more upwelling of sDIC.

Southern Ocean STSS According to the linear approximation, the effect of winds was a strong trend towards more uptake of CO_2 (6 to $8\,\mu\mathrm{mol\,C\,m^{-2}d^{-2}}$ per yr) related to the strengthening of westerly winds which enhanced the mean CO_2 flux directed into the ocean, whereas the wind-driven trends in the CO_2 flux density found using a series of simulations were not uniform: Towards somewhat more outgassing in the Atlantic sector probably due to more upwelling of sDIC in the southern part of the STSS ($-3\,\mu\mathrm{mol\,C\,m^{-2}d^{-2}}$ per yr) and towards much more uptake in the Indian sector probably due to more downwelling in the northern part of the STSS ($7\,\mu\mathrm{mol\,C\,m^{-2}d^{-2}}$ per yr).

STPS According to the linear approximation, the effect of winds was small (less than $\pm 1\,\mu\mathrm{mol\,C\,m^{-2}d^{-2}}$ per yr), whereas the wind-driven trends in the CO_2 flux density found using a series of simulations were towards somewhat more outgassing (-1 to $-3\,\mu\mathrm{mol\,C\,m^{-2}d^{-2}}$ per yr).

EQU The effect of winds was between $\pm 1\,\mu\mathrm{mol\,C\,m^{-2}d^{-2}}$ per yr according to the linear approximation and between $\pm 2\,\mu\mathrm{mol\,C\,m^{-2}d^{-2}}$ per yr according to the series of simulations.

Northern hemisphere STSS According to the linear approximation, variability in winds induced a considerable trend towards less uptake of CO_2 (between -2 and $-3\,\mu\mathrm{mol\,C\,m^{-2}d^{-2}}$ per yr) as winds were weakening, thus reducing the mean flux of CO_2 directed into the ocean. According to the simulation, the effect was even stronger (between -2 and $-7\,\mu\mathrm{mol\,C\,m^{-2}d^{-2}}$ per yr).

North Atlantic SPSS According to the linear approximation, variability in winds induced a strong trend towards more CO_2 uptake ($\sim 6\,\mu\mathrm{mol\,C\,m^{-2}d^{-2}}$ per yr) as winds were strengthening, thus increasing the mean flux of CO_2 directed into the ocean. According to the simulation, the effect was even stronger ($\sim 10\,\mu\mathrm{mol\,C\,m^{-2}d^{-2}}$ per yr) related to changes in the western part of the SPSS associated with a displacement of the North Atlantic Current.

Northern hemisphere ICE The effect of winds was regionally heterogeneous for both approaches.

5.4.1 Comparison with Le Quéré et al. (2010)

Same as for the effect of temperature and total climate variability, the effect of winds simulated by FESOM-REcoM during 1981-2007 has the same sign, but is smaller than in Le Quéré et al.'s (2010) model experiment ($-8.9\,\mathrm{Tg\,C\,yr^{-1}}$ per yr in FESOM-REcoM compared to $-12\,\mathrm{Tg\,C\,yr^{-1}}$ per yr). At least partly, this can be explained by differences in the setup of the model experiments. Consistent with Le Quéré et al.'s (2010) model setup, a simulation with fully variable atmospheric forcing is compared to a simulation with constant wind forcing to separate the effect of the wind forcing. But whereas Le Quéré et al. (2010) performed the model experiment with a carbon cycle insensitive to temperature variability, the carbon cycle in FESOM-REcoM is sensitive to temperature variability. Consequently, Le Quéré et al. (2010) have **not** included nonlinearities such as a simultaneous upwelling and warming in their estimate for the effect of variability in winds on the CO_2 flux. In addition, the choice of the time period is crucial, as decadal variability can induce a wind-driven trend in the CO_2 flux that disappears on longer time scales. In fact, in FESOM-REcoM, the wind-driven trend in the CO_2 flux is smaller when considering the whole simulation length ($-2.9\,\mathrm{Tg\,C\,yr^{-1}}$ per yr) than for the shorter time span ($-8.9\,\mathrm{Tg\,C\,yr^{-1}}$ per yr for 1981-2007).

5.5 Effect of sDIC and sAlk on the CO_2 flux trend

Most of the disagreement between the linear approach and the model experiment stems from the impact of climate variability on the surface concentration of sDIC. Trends in sDIC are mostly caused either by climate-driven changes in the transport of natural sDIC with the circulation ($-2.80\,\mathrm{mmol\,C\,m^{-3}}$ per yr, Table 4.4) or changes in the air-sea carbon flux ($2.98\,\mathrm{mmol\,C\,m^{-3}}$ per yr). The impact of changes in the ocean biology on the mixed layer sDIC concentration is comparatively smaller ($0.08\,\mathrm{mmol\,C\,m^{-3}}$ per yr). By running model simulations with constant forcing fields for wind and temperature, respectively, I found an increase or decrease in the surface sDIC concentration trend (by 0.01 and $-0.07\,\mathrm{mmol\,C\,m^{-3}}$ per yr) in each simulation. These trends in the surface sDIC concentration are assigned to the wind and temperature forcing. They probably account for a large part of the indirect effect of the wind and temperature forcing on the trend in the CO_2 flux. However, the trend in the surface sDIC concentration was only $-0.02\,\mathrm{mmol\,C\,m^{-3}}$ per yr in the historical simulation, which is much less than the sum of the trends in sDIC attributed to the variability of winds or temperature alone.

5.5.1 Stabilization of the sDIC concentration by the air-sea CO_2 flux

Regarding the simulation with a fully variable atmospheric climate forcing at constant atmospheric CO_2 concentrations (sim-D), the trend in the surface sDIC concentration was separated into parts arising due to trends in the air-sea flux, transport with the circulation and biological productivity (Section 4.2.10). It turned out that trends in the sDIC concentration due to trends in these drivers mostly canceled out so that the net trend in sDIC appeared comparatively small. This suggests that changes in the surface flux of CO_2 (F_{surf}) compensate for changes in the oceanic fluxes (F_{circ} and F_{bio}). Changes in the oceanic fluxes alter the mixed layer sDIC concentration, which leads to a change of $\mathrm{pCO_2^O}$ at the ocean surface and a response of the air-sea flux. Changes in the air-sea flux (ΔF_{surf}) fully compensate for changes in the oceanic fluxes (ΔF_{circ} and ΔF_{bio}) when

$$\Delta F_{\mathrm{surf}} = \frac{\partial F_{\mathrm{surf}}}{\partial(\mathrm{sDIC})} \cdot \Delta\mathrm{sDIC} = -(\Delta F_{\mathrm{circ}} + \Delta F_{\mathrm{bio}}) \tag{5.1}$$

Thus at:

$$\Delta\mathrm{sDIC} = \left(-\frac{\partial F_{\mathrm{surf}}}{\partial(\mathrm{sDIC})}\right)^{-1} \cdot (\Delta F_{\mathrm{circ}} + \Delta F_{\mathrm{bio}}) \approx 7\frac{\mathrm{mmol\,C\,m^{-3}}}{\mathrm{mmol\,C\,m^{-2}d^{-1}}} \cdot (\Delta F_{\mathrm{circ}} + \Delta F_{\mathrm{bio}}) \tag{5.2}$$

where $7\frac{\text{mmol C m}^{-3}}{\text{mmol C m}^{-2}\text{d}^{-1}}$ is the global mean calculated from Equation (3.37) using the model output and only considering ice-free grid cells because $\frac{\partial F_{\text{surf}}}{\partial(\text{sDIC})} = 0$ if the surface is covered by ice. In sim-D, the trend in the oceanic CO_2 fluxes ($\beta(F_{\text{circ}}) + \beta(F_{\text{bio}})$) is estimated to be ~$2.4\,\mu\text{mol C m}^{-2}\text{d}^{-1}$ per yr. Without a compensation by the air-sea CO_2 flux, this would have induced an increase in mixed layer sDIC concentrations by ~$0.90\,\text{mmol C m}^{-3}$ per yr (Table 4.4). However, it follows from Equation (5.2) that a trend in the oceanic fluxes by $2.4\,\mu\text{mol C m}^{-2}\text{d}^{-1}$ per yr leads to a fully compensating outgassing air-sea flux already under an increase of the mixed layer sDIC concentration by ~$0.02\,\text{mmol C m}^{-3}$ per yr. This illustrates that the air-sea flux is very sensitive to changes in F_{circ} and F_{bio} and stabilizes the mixed layer sDIC concentration through its response.

5.5.2 Removal of anthropogenic sDIC from the surface by the circulation

In the simulation with historical atmospheric CO_2 concentrations at a constant climate (sim-C), the increase in atmospheric CO_2 drove an increase in the air-sea CO_2 flux. If all of the anthropogenic CO_2 had remained at the ocean surface, the mixed layer sDIC concentration would have increased by ~$4.40\,\text{mmol C m}^{-3}$ per yr (Table 4.4), corresponding to an increase in integrated mixed layer sDIC content by $1.1\,\text{Pg C yr}^{-1}$ (using a mixed layer volume of ~$7.6 \times 10^6\,\text{m}^3$). About $3.81\,\text{mmol C m}^{-3}$ per yr of this, that is $0.96\,\text{Pg C yr}^{-1}$ or 87%, were compensated by an increase in the transport of anthropogenic CO_2 into the depth with the circulation. Only the fraction of sDIC that remains at the surface affects the surface pCO_2^O and thus the air-sea CO_2 flux.

5.5.3 Competing effect of variability in sDIC and sAlk on the CO_2 flux

In the absence of anthropogenic carbon, the changes in sDIC and sAlk at the ocean surface are sometimes related to each other through upwelling of water that is rich in both sDIC and sAlk. Furthermore, some biological processes alter both sDIC and sAlk. Additionally, sDIC and sAlk might sometimes appear pseudo-correlated as both are affected by the salinity normalization. Consequentially, the trends in sDIC and sAlk were often, but not everywhere, anti-correlated in the FESOM-REcoM simulations. Because the Revelle factor γ_{DIC} is positive and γ_{Alk} is negative, trends in sDIC and sAlk have a competing effect on the trend in the CO_2 flux. Locally, the effect of trends in sDIC on the CO_2 flux is often between 1 and 1.5 times higher than the effect of sAlk.

At high latitudes, that is in the SPSS and STSS biomes, variability in sDIC was the most important climate factor affecting the trend in the CO_2 flux density (Figures S25 to S27). Because the effect of sDIC on the trend in the CO_2 flux density had the opposite sign in different parts of the world, it largely canceled out on the global scale. Due to the compensation of regionally rather large effects, already small differences in some regions between models can result in comparatively large differences globally. On the other hand, since more upwelling of sDIC in one place is connected to less upwelling of sDIC in another place, some globally compensating effects are expected in any model. In contrast to sDIC, much of the sAlk-induced regional trends in the CO_2 flux did not cancel out on the global scale, so that sAlk had a stronger impact on the trend in the global mean CO_2 flux than sDIC.

5.5.4 The impact of model physics

Given the importance of variability in sDIC concentrations for the trend in the CO_2 flux, it might also account for parts of the discrepancy between Le Quéré et al.'s (2010) and Gruber et al.'s (2019) estimates and FESOM-REcoM. The lower estimate for the effect of increasing atmospheric CO_2 on the CO_2 flux in FESOM-REcoM (Tables 5.1 and 5.2) suggests that the removal of anthropogenic sDIC from the mixed layer into the intermediate and deep ocean with the circulation is less efficient in FESOM-REcoM, while the lower estimate for the effect of global warming on the CO_2 flux in FESOM-REcoM suggests that there is less transport of waters with unmodified sDIC concentrations

to the surface; all in all, a more sluggish transport of sDIC with the circulation in FESOM-REcoM. Differences in the model physics are known to give rise to considerable inter-model spread in the biogeochemical fields (Doney et al., 2004), as the strength of overturning varies between models by ~20-30% (Huber and Zanna, 2017). The spread in model physics is particularly large in the Atlantic Nordic Seas related to the formation of North Atlantic Deep Water and in the region of the Antarctic Circumpolar Current related to wind-driven overturning. Both are regions with high trends in the CO_2 flux density in FESOM-REcoM that contribute above average to the globally integrated CO_2 flux trend (Figures 4.1b and 4.4). The strength of the Atlantic Meridional Overturning Circulation in the ocean-only version of FESOM falls within the lower range compared to other ocean circulation models (Hirschi et al., 2020), which could be an indication for less transport of sDIC. However, studies of the vertical sDIC gradient and the inventory of natural and anthropogenic carbon at different depth levels combined with an evaluation of the physical fields are needed to evaluate the role of model physics on the transport of sDIC and the resulting air-sea CO_2 fluxes, which is beyond the scope of this thesis.

5.6 Sea-ice

According to the series of simulations, the decrease of the sea-ice concentration in the northern hemisphere over the simulation period was a consequence of global warming. Hence, the model experiments with and without global warming also sheds light on the impact of the retreat of sea-ice on the CO_2 flux at the relevant locations. According to the series of simulations, the reduction of the sea-ice concentration at the transition zone of the North Atlantic SPSS biome and the North Atlantic ICE biome led to a trend towards more uptake of $\sim 0.3\,\mathrm{Tg\,C\,yr^{-1}\,per\,yr}$, thus making a non-negligible contribution to the climate-related trend in the globally integrated CO_2 flux. In the North Atlantic, the linear approximation of the impact of the decreasing sea-ice concentration on the CO_2 flux yielded a value corresponding to only 30% of the simulated effect, because only the impact of sea-ice on the air-sea gas transfer is included in the estimate, while a deepening of the mixed layer and an increase in biological productivity related to the decrease in sea-ice concentration play an additional role in the simulation. In the Asian and Pacific sector of the northern hemisphere ICE biome, the retreat of sea-ice led to more outgassing of CO_2. Here, the linear approximation yields higher values for the trend in the CO_2 flux density due to the retreat of sea-ice than the simulated effect. This can be explained by unrealistically high pCO_2^O below the ice-cover in these regions in FESOM-REcoM, implying an overestimated linear sensitivity of the CO_2 flux to sea-ice changes (Equation (3.25)). When the trend in the CO_2 flux in the same region is analyzed by comparing the model experiments with and without the warming-driven retreat of sea-ice, a smaller effect of sea-ice on the trend in the CO_2 flux is found, as the high pCO_2^O below the sea-ice cover diminishes with the disappearance of the sea-ice.

5.7 Salinity and freshwater fluxes

According to the linear approximation, the impact of change and variability in freshwater fluxes on the trend in the CO_2 flux is mostly generated at high latitudes, meaning that the ICE and SPSS biomes account for more than 50% of the (S+FW)-related trend in the globally integrated CO_2 flux. This is likely due to two factors: On the one hand, the CO_2 flux is very sensitive to changes in salinity and freshwater fluxes in the SPSS biome as the gas transfer coefficient is high there. On the other hand, the variability in freshwater fluxes is large at high latitudes related to changes in sea-ice formation, transport and melt (Haumann et al., 2016).

Furthermore, the impact of changes in the salinity and freshwater fluxes was much higher on the historical CO_2 flux (in sim-A) than on the natural CO_2 flux (in sim-D), which was particularly visible in the Southern Ocean. Firstly, the impact of freshwater fluxes on the DIC concentration

is proportional to the salinity-normalized DIC concentration (Equation (3.33)). Secondly, the sensitivity of pCO_2^O to freshwater-driven changes in DIC, the Revelle factor, is higher at high DIC concentrations (Equation (3.35)). Thus, the presence of anthropogenic carbon enhanced the effect of freshwater fluxes on the CO_2 flux, thus explaining some of the differences between the simulation with and without atmospheric CO_2 increase.

For this thesis, I did not perform a model simulation to explicitly separate the effect of freshwater fluxes on the CO_2 flux. Instead, the freshwater fluxes are contained in the "other climate parameters" as the residual trend in the CO_2 flux which cannot be attributed to the sum of winds and temperature and which partly arises due to nonlinear effects. Le Quéré et al. (2010) grouped the effect of freshwater fluxes with heat fluxes, thus including the combined variability of the thermohaline circulation in one set of forcings which partly overlaps with my definition of the temperature effect.

5.8 Conclusions

In the simulated time period from 1958-2019, the ocean acted as a sink for anthropogenic CO_2. Simultaneously, climate change and variability have caused the ocean to release more natural CO_2 into the atmosphere. Climate change and variability have offset about 21% of the trend in the CO_2 flux towards more oceanic uptake driven by the anthropogenic increase in atmospheric CO_2. In FESOM-REcoM, the climate-related outgassing of natural CO_2 is less prominent than in previous studies. On the one hand, this is related to the time period considered: In the simulations for this thesis, we consider a multidecadal time period and thus eliminate some of the decadal variability captured in previous studies. Furthermore, earlier decades in which the effect of climate change was presumably weaker than in the 21st century are included here. Additionally, some of the discrepancy even remains when the same time period is considered and hence, the discrepancy must be related to differences between the models, parameter choices and forcing data sets.

The change and variability in winds are the most important factors driving the outgassing of natural CO_2 mainly through a changed transport of sDIC with the circulation. Therefore, the simulated effect of winds strongly depends on the model physics. The second most important driver is global warming. A linear approximation of the temperature effect resulted in an overestimate compared to the simulated temperature effect. Again, the simulated effect depends on the model physics, as it is regulated by the upwelling of waters which subsequently experience warming at the ocean surface. Compared to the effect of climate change and variability on the natural air-sea flux of CO_2, the impact of climate on the anthropogenic carbon uptake is smaller and more unclear. Furthermore, a better look into the effect of sAlk on the CO_2 flux is needed, as the trend in sAlk was the second most important variable affecting the trend in the globally integrated CO_2 flux according to the linear approximation. Therefore, the role of alkalinity appears to go beyond a compensation of changes in sDIC.

If anthropogenic CO_2 emissions cease in the future, the anthropogenic component of the air-sea CO_2 flux directed into the ocean is expected to stop growing. In contrast, the trend in the air-sea CO_2 flux towards more outgassing of natural CO_2 driven by climate change is expected to persist longer (Solomon et al., 2009). Therefore, the separation of the total CO_2 flux into the climate-driven component and the part driven by the increase in atmospheric CO_2 is relevant for future projections. Considering the separation in these two components of the CO_2 flux, the discrepancy between FESOM-REcoM and other studies is considerable, which suggests that more studies must be included for a realistic estimate of both components. Thereby, the separation of the climate effect and anthropogenic CO_2 fluxes is most straight-forward in model studies. The North Atlantic and Southern Ocean are of particular interest because of the above-average trends in the CO_2 flux densities, whereas the tropical and subtropical regions are mostly relevant due to their size.

Chapter 6

Directory

Abbreviations

A, B, C, D, E and F	Simulations (see Table 2.1)
α	Solubility of CO_2 in water
Alk	Alkalinity
airT	Air temperature
$\beta(...)$	Trend in a variable
$\beta^*(F)$	Trend in the CO_2 flux approximated following Section 3.2
DIC	Dissolved inorganic carbon
ΔpCO_2	$pCO_2^A - pCO_2^O$
ENSO	El Niño-Southern Oscillation
F_{surf}	CO_2 flux from the atmosphere into the ocean
FW	Freshwater fluxes
ice	Sea-ice concentration, i.e. fraction of grid cell that is ice-covered
J_{bio}	Removal of DIC from the mixed layer through biological export production (only negative values)
J_{circ}	Transport of DIC into the mixed layer due to the circulation (positive: from depth or adjacent grid cells into the mixed layer)
J_{surf}	Change of DIC in the mixed layer due to the CO_2 flux from the atmosphere at the ocean surface (positive: increase of DIC)
k_w	Gas transfer velocity (piston velocity)
MLD	Mixed layer depth
ONI 3.4	Oceanic Niño Index 3.4
pCO_2^A	Atmospheric partial pressure of CO_2
pCO_2^O	Partial pressure of CO_2 at the ocean surface
sAlk	Salinity-normalized alkalinity (Equation (3.39))
sDIC	Salinity-normalized dissolved inorganic carbon (Equation (3.33))
S	Salinity
Sc	Schmidt number
SST	Sea surface temperature
T	Sea surface temperature
U	Wind velocity

List of Tables

References

Armour, K. C., Marshall, J., Scott, J. R., Donohoe, A., and Newsom, E. R. Southern Ocean warming delayed by circumpolar upwelling and equatorward transport. *Nature Geoscience*, 9(7):549–554, 2016. ISSN 17520908. doi: 10.1038/ngeo2731.

Bakker, D. C. E., Pfeil, B., Landa, C. S., Metzl, N., O'Brien, K. M., Olsen, A., Smith, K., Cosca, C., Harasawa, S., Jones, S. D., Nakaoka, S., Nojiri, Y., Schuster, U., Steinhoff, T., Sweeney, C., Takahashi, T., Tilbrook, B., Wada, C., Wanninkhof, R., Alin, S. R., Balestrini, C. F., Barbero, L., Bates, N. R., Bianchi, A. A., Bonou, F., Boutin, J., Bozec, Y., Burger, E. F., Cai, W.-J., Castle, R. D., Chen, L., Chierici, M., Currie, K., Evans, W., Featherstone, C., Feely, R. A., Fransson, A., Goyet, C., Greenwood, N., Gregor, L., Hankin, S., Hardman-Mountford, N. J., Harlay, J., Hauck, J., Hoppema, M., Humphreys, M. P., Hunt, C. W., Huss, B., Ibánhez, J. S. P., Johannessen, T., Keeling, R., Kitidis, V., Körtzinger, A., Kozyr, A., Krasakopoulou, E., Kuwata, A., Landschützer, P., Lauvset, S. K., Lefèvre, N., Lo Monaco, C., Manke, A., Mathis, J. T., Merlivat, L., Millero, F. J., Monteiro, P. M. S., Munro, D. R., Murata, A., Newberger, T., Omar, A. M., Ono, T., Paterson, K., Pearce, D., Pierrot, D., Robbins, L. L., Saito, S., Salisbury, J., Schlitzer, R., Schneider, B., Schweitzer, R., Sieger, R., Skjelvan, I., Sullivan, K. F., Sutherland, S. C., Sutton, A. J., Tadokoro, K., Telszewski, M., Tuma, M., van Heuven, S. M. A. C., Vandemark, D., Ward, B., Watson, A. J., and Xu, S. A multi-decade record of high-quality fco_2 data in version 3 of the surface ocean co_2 atlas (socat). *Earth System Science Data*, 8(2): 383–413, 2016. doi: 10.5194/essd-8-383-2016. URL `https://essd.copernicus.org/articles/8/383/2016/`.

Chatterjee, A., Gierach, M. M., Sutton, A. J., Feely, R. A., Crisp, D., Eldering, A., Gunson, M. R., O'Dell, C. W., Stephens, B. B., and Schimel, D. S. Influence of El Niño on atmospheric CO2 over the tropical Pacific Ocean: Findings from NASA's OCO-2 mission. *Science*, 358(6360), 2017. ISSN 10959203. doi: 10.1126/science.aam5776.

Collins, M., An, S. I., Cai, W., Ganachaud, A., Guilyardi, E., Jin, F. F., Jochum, M., Lengaigne, M., Power, S., Timmermann, A., Vecchi, G., and Wittenberg, A. The impact of global warming on the tropical Pacific Ocean and El Nino. *Nat. Geosci.*, 3(6):391–397, 2010. ISSN 17520894. doi: 10.1038/ngeo868.

Deser, C., Alexander, M. A., Xie, S. P., and Phillips, A. S. Sea surface temperature variability: Patterns and mechanisms. *Annual Review of Marine Science*, 2(1):115–143, 2010. ISSN 19411405. doi: 10.1146/annurev-marine-120408-151453.

DeVries, T., Holzer, M., and Primeau, F. Recent increase in oceanic carbon uptake driven by weaker upper-ocean overturning. *Nature*, 542(7640):215–218, 2017. ISSN 14764687. doi: 10.1038/nature21068. URL `http://dx.doi.org/10.1038/nature21068`.

DeVries, T., Le Quéré, C., Andrews, O., Berthet, S., Hauck, J., Ilyina, T., Landschützer, P., Lenton, A., Lima, I. D., Nowicki, M., Schwinger, J., and Séférian, R. Decadal trends in the ocean carbon

sink. *Proceedings of the National Academy of Sciences of the United States of America*, 116(24): 11646–11651, 2019. ISSN 10916490. doi: 10.1073/pnas.1900371116.

Doney, S. C., Lindsay, K., Caldeira, K., Campin, J.-M., Drange, H., Dutay, J.-C., Follows, M., Gao, Y., Gnanadesikan, A., Gruber, N., Ishida, A., Joos, F., Madec, G., Maier-Reimer, E., Marshall, J. C., Matear, R. J., Monfray, P., Mouchet, A., Najjar, R., Orr, J. C., Plattner, G.-K., Sarmiento, J., Schlitzer, R., Slater, R., Totterdell, I. J., Weirig, M.-F., Yamanaka, Y., and Yool, A. Evaluating global ocean carbon models: The importance of realistic physics. *Global Biogeochemical Cycles*, 18(3), 2004. doi: https://doi.org/10.1029/2003GB002150.

Eddebbar, Y. A., Rodgers, K. B., Long, M. C., Subramanian, A. C., Xie, S. P., and Keeling, R. F. El Niño-like physical and biogeochemical ocean response to tropical eruptions. *Journal of Climate*, 32(9):2627–2649, 2019. ISSN 08948755. doi: 10.1175/JCLI-D-18-0458.1.

Egleston, E. S., Sabine, C. L., and Morel, F. M. Revelle revisited: Buffer factors that quantify the response of ocean chemistry to changes in DIC and alkalinity. *Global Biogeochemical Cycles*, 24 (1):1–9, 2010. ISSN 08866236. doi: 10.1029/2008GB003407.

Evans, J. and Argüeso, D. Guidance on the use of bias corrected data. *NARCliM Consortium, Sydney, Australia*, 2014. NARCliM Technical Note 3.

Fassbender, A. J., Sabine, C. L., and Palevsky, H. I. Nonuniform ocean acidification and attenuation of the ocean carbon sink. *Geophysical Research Letters*, 44(16):8404–8413, 2017. ISSN 19448007. doi: 10.1002/2017GL074389.

Fay, A. R. and McKinley, G. A. Global open-ocean biomes: Mean and temporal variability. *Earth System Science Data*, 6(2):273–284, 2014. ISSN 18663516. doi: 10.5194/essd-6-273-2014.

Friederich, G. E., Ledesma, J., Ulloa, O., and Chavez, F. P. Air-sea carbon dioxide fluxes in the coastal southeastern tropical Pacific. *Progress in Oceanography*, 79(2-4):156–166, 2008. ISSN 00796611. doi: 10.1016/j.pocean.2008.10.001. URL `http://dx.doi.org/10.1016/j.pocean.2008.10.001`.

Friedlingstein, P., O'Sullivan, M., Jones, M. W., Andrew, R. M., Hauck, J., Olsen, A., Peters, G. P., Peters, W., Pongratz, J., Sitch, S., Le Quéré, C., Canadell, J. G., Ciais, P., Jackson, R. B., Alin, S., Aragão, L. E. O. C., Arneth, A., Arora, V., Bates, N. R., Becker, M., Benoit-Cattin, A., Bittig, H. C., Bopp, L., Bultan, S., Chandra, N., Chevallier, F., Chini, L. P., Evans, W., Florentie, L., Forster, P. M., Gasser, T., Gehlen, M., Gilfillan, D., Gkritzalis, T., Gregor, L., Gruber, N., Harris, I., Hartung, K., Haverd, V., Houghton, R. A., Ilyina, T., Jain, A. K., Joetzjer, E., Kadono, K., Kato, E., Kitidis, V., Korsbakken, J. I., Landschützer, P., Lefèvre, N., Lenton, A., Lienert, S., Liu, Z., Lombardozzi, D., Marland, G., Metzl, N., Munro, D. R., Nabel, J. E. M. S., Nakaoka, S.-I., Niwa, Y., O'Brien, K., Ono, T., Palmer, P. I., Pierrot, D., Poulter, B., Resplandy, L., Robertson, E., Rödenbeck, C., Schwinger, J., Séférian, R., Skjelvan, I., Smith, A. J. P., Sutton, A. J., Tanhua, T., Tans, P. P., Tian, H., Tilbrook, B., van der Werf, G., Vuichard, N., Walker, A. P., Wanninkhof, R., Watson, A. J., Willis, D., Wiltshire, A. J., Yuan, W., Yue, X., and Zaehle, S. Global Carbon Budget 2020. *Earth System Science Data*, 12(4):3269–3340, 2020. doi: 10.5194/essd-12-3269-2020.

Fung, I. Y., Doney, S. C., Lindsay, K., and John, J. Evolution of carbon sinks in a changing climate. *Proceedings of the National Academy of Sciences of the United States of America*, 102 (32):11201–11206, 2005. ISSN 00278424. doi: 10.1073/pnas.0504949102.

Garcia, H., Locarnini, R., Boyer, T., Antonov, J., Baranova, O., Zweng, M., Reagan, J., and Johnson, D. World Ocean Atlas 2013, Volume 4 : Dissolved Inorganic Nutrients (phosphate, nitrate, silicate). *NOAA Atlas NESDIS 76*, 4(September):25, 2013.

Gruber, N., Clement, D., Carter, B. R., Feely, R. A., van Heuven, S., Hoppema, M., Ishii, M., Key, R. M., Kozyr, A., Lauvset, S. K., Monaco, C. L., Mathis, J. T., Murata, A., Olsen, A., Perez, F. F., Sabine, C. L., Tanhua, T., and Wanninkhof, R. The oceanic sink for anthropogenic CO2 from 1994 to 2007. *Science*, 363(6432):1193–1199, 2019. ISSN 10959203. doi: 10.1126/science.aau5153.

Gürses, Ö. REcoM2 Documentation, 2021. `https://recom.readthedocs.io/` [accessed 31.05.2021].

Hanawa, K. and D.Talley, L. Chapter 5.4 mode waters. In Siedler, G., Church, J., and Gould, J., editors, *Ocean Circulation and Climate*, volume 77 of *International Geophysics*, pages 373–386. Academic Press, 2001. doi: https://doi.org/10.1016/S0074-6142(01)80129-7. URL `https://www.sciencedirect.com/science/article/pii/S0074614201801297`.

Hauck, J., Völker, C., Wang, T., Hoppema, M., Losch, M., and Wolf-Gladrow, D. A. REcoM model equations (supplement). *Global Biogeochemical Cycles*, 27(4):1236–1245, 2013a. ISSN 08866236. URL `http://doi.wiley.com/10.1002/2013GB004600`.

Hauck, J., Völker, C., Wang, T., Hoppema, M., Losch, M., and Wolf-Gladrow, D. A. Seasonally different carbon flux changes in the Southern Ocean in response to the southern annular mode. *Global Biogeochemical Cycles*, 27(4):1236–1245, 2013b. ISSN 08866236. doi: 10.1002/2013GB004600.

Hauck, J., Zeising, M., Le Quéré, C., Gruber, N., Bakker, D. C., Bopp, L., Chau, T. T. T., Gürses, Ö., Ilyina, T., Landschützer, P., Lenton, A., Resplandy, L., Rödenbeck, C., Schwinger, J., and Séférian, R. Consistency and Challenges in the Ocean Carbon Sink Estimate for the Global Carbon Budget. *Frontiers in Marine Science*, 7(October):1–22, 2020. ISSN 22967745. doi: 10.3389/fmars.2020.571720.

Hauck, J., Gruber, N., Orr, J., Müller, J. D., and Gregor, L. About reccap2-ocean, 2021. `https://reccap2-ocean.github.io/` [accessed 25.06.2021].

Haumann, A., Gruber, N., Münnich, M., Frenger, I., and Kern, S. Sea-ice transport driving Southern Ocean salinity and its recent trends. *Nature*, 537(7618):89–92, 2016. ISSN 14764687. doi: 10.1038/nature19101.

Haumann, F. A., Gruber, N., and Münnich, M. Sea-Ice Induced Southern Ocean Subsurface Warming and Surface Cooling in a Warming Climate. *AGU Advances*, 1(2):e2019AV000132, 2020. doi: https://doi.org/10.1029/2019AV000132.

Hirschi, J. J.-M., Barnier, B., Böning, C., Biastoch, A., Blaker, A. T., Coward, A., Danilov, S., Drijfhout, S., Getzlaff, K., Griffies, S. M., Hasumi, H., Hewitt, H., Iovino, D., Kawasaki, T., Kiss, A. E., Koldunov, N., Marzocchi, A., Mecking, J. V., Moat, B., Molines, J.-M., Myers, P. G., Penduff, T., Roberts, M., Treguier, A.-M., Sein, D. V., Sidorenko, D., Small, J., Spence, P., Thompson, L., Weijer, W., and Xu, X. The Atlantic Meridional Overturning Circulation in High-Resolution Models. *Journal of Geophysical Research: Oceans*, 125(4):e2019JC015522, 2020. doi: https://doi.org/10.1029/2019JC015522. e2019JC015522 2019JC015522.

Hofmann, D. J., Butler, J. H., and Tans, P. P. A new look at atmospheric carbon dioxide. *Atmospheric Environment*, 43(12):2084–2086, 2009. ISSN 1352-2310. doi: https://doi.org/10.1016/j.atmosenv.2008.12.028.

Huber, M. B. and Zanna, L. Drivers of uncertainty in simulated ocean circulation and heat uptake. *Geophysical Research Letters*, 44(3):1402–1413, 2017. doi: https://doi.org/10.1002/2016GL071587.

IPCC. Chapter 10 - Detection and attribution of climate change: From global to regional. In Bindoff, N., Stott, P., Achuta-Rao, K., Allen, M., Gillett, N., Gutzler, D., Hansingo, K., Hegerl,

G., Hu, Y., Jain, S., Mokhov, I., Overland, J., Perlwitz, J., Sebbari, R., and Zhang, X., editors, *Climate Change 2013: The Physical Science Basis. Contribution of Working Group I to the Fifth Assessment Report of the Intergovernmental Panel on Climate Change*. Cambridge University Press, 2013a.

IPCC. Chapter 12 - Long-term climate change: Projections, commitments and irreversibility. In Collins, M., Knutti, R., Arblaster, J., Dufresne, J.-L., Fichefet, T., Friedlingstein, P., Gao, X., Gutowski, W., Johns, T., Krinner, G., Shongwe, M., Tebaldi, C., Weaver, A., and Wehner, M., editors, *Climate Change 2013: The Physical Science Basis. Contribution of Working Group I to the Fifth Assessment Report of the Intergovernmental Panel on Climate Change*. Cambridge University Press, 2013b.

IPCC. Technical Summary. In Stocker, T., Qin, D., Plattner, G.-K., Alexander, L., Allen, S., Bindoff, N., Bréon, F.-M., Church, J., Cubasch, U., Emori, S., Forster, P., Friedlingstein, P., Gillett, N., Gregory, J., Hartmann, D., Jansen, E., Kirtman, B., Knutti, R., Krishna-Kumar, K., Lemke, P., Marotzke, J., Masson-Delmotte, V., Meehl, G., Mokhov, I., Piao, S., Ramaswamy, V., Randall, D., Rhein, M., Rojas, M., Sabine, C., Shindell, D., Talley, L., Vaughan, D., and Xie, S.-P., editors, *Climate Change 2013: The Physical Science Basis. Contribution of Working Group I to the Fifth Assessment Report of the Intergovernmental Panel on Climate Change*. Cambridge University Press, 2013c.

Jacobson, A. R., Mikaloff Fletcher, S. E., Gruber, N., Sarmiento, J. L., and Gloor, M. A joint atmosphere-ocean inversion for surface fluxes of carbon dioxide: 2. regional results. *Global Biogeochemical Cycles*, 21(1), 2007. doi: https://doi.org/10.1029/2006GB002703. URL `https://agupubs.onlinelibrary.wiley.com/doi/abs/10.1029/2006GB002703`.

JMA. About JRA-55: The Japanese 55-year Reanalysis, 2021. `https://jra.kishou.go.jp/JRA-55/index_en.html#jra-55` [accessed 14.06.2021].

Landschützer, P., Gruber, N., Haumann, F. A., Rödenbeck, C., Bakker, D. C. E., Heuven, S. V., Hoppema, M., Metzl, N., Sweeney, C., and Takahashi, T. Ocean carbon sink. *Science*, 349(6253): 1221–1224, 2015.

Landschützer, P., Gruber, N., and Bakker, D. C. Decadal variations and trends of the global ocean carbon sink. *Global Biogeochemical Cycles*, 30(10):1396–1417, 2016. ISSN 19449224. doi: 10.1002/2015GB005359.

Landschützer, P., Ilyina, T., and Lovenduski, N. S. Detecting Regional Modes of Variability in Observation-Based Surface Ocean pCO_2. *Geophysical Research Letters*, 46(5):2670–2679, 2019. ISSN 19448007. doi: 10.1029/2018GL081756.

Large, W. G. and Yeager, S. G. The global climatology of an interannually varying air - Sea flux data set. *Clim. Dyn.*, 33(2-3):341–364, 2009. ISSN 09307575. doi: 10.1007/s00382-008-0441-3.

Lauvset, S. K., Key, R. M., Olsen, A., Van Heuven, S., Velo, A., Lin, X., Schirnick, C., Kozyr, A., Tanhua, T., Hoppema, M., Jutterström, S., Steinfeldt, R., Jeansson, E., Ishii, M., Perez, F. F., Suzuki, T., and Watelet, S. A new global interior ocean mapped climatology: The $1^\circ \times 1^\circ$ GLODAP version 2. *Earth System Science Data*, 8(2):325–340, 2016. doi: 10.5194/essd-8-325-2016.

Le Quéré, C., Rödenbeck, C., Buitenhuis, E. T., Conway, T. J., Langenfelds, R., Gomez, A., Labuschagne, C., Ramonet, M., Nakazawa, T., Metzl, N., Gillett, N., and Heimann, M. Saturation of the Southern Ocean CO_2 Sink Due to Recent Climate Change. *Science*, 316(5832): 1735–1738, 2007. ISSN 0036-8075. doi: 10.1126/science.1136188.

Le Quéré, C., Raupach, M. R., Canadell, J. G., Marland, G., Bopp, L., Ciais, P., Conway, T. J., Doney, S. C., Feely, R. A., Foster, P., Friedlingstein, P., Gurney, K., Houghton, R. A., House, J. I., Huntingford, C., Levy, P. E., Lomas, M. R., Majkut, J., Metzl, N., Ometto, J. P., Peters, G. P., Prentice, I. C., Randerson, J. T., Running, S. W., Sarmiento, J. L., Schuster, U., Sitch, S., Takahashi, T., Viovy, N., Van Der Werf, G. R., and Woodward, F. I. Trends in the sources and sinks of carbon dioxide. *Nat. Geosci.*, 2(12):831–836, 2009. ISSN 17520894. doi: 10.1038/ngeo689.

Le Quéré, C., Takahashi, T., Buitenhuis, E. T., Rödenbeck, C., and Sutherland, S. C. Impact of climate change and variability on the global oceanic sink of CO_2. *Global Biogeochemical Cycles*, 24(4):1–10, 2010. ISSN 08866236. doi: 10.1029/2009GB003599.

Levèvre, N., Watson, A. J., Olsen, A., Ríos, A. F., Pérez, F. F., and Johannessen, T. A decrease in the sink for atmospheric CO_2 in the North Atlantic. *Geophysical Research Letters*, 31(7):2–5, 2004. ISSN 00948276. doi: 10.1029/2003GL018957.

Lovenduski, N. S., Gruber, N., Doney, S. C., and Lima, I. D. Enhanced CO_2 outgassing in the Southern Ocean from a positive phase of the Southern Annular Mode. *Global Biogeochemical Cycles*, 21(2):1–14, 2007. ISSN 08866236. doi: 10.1029/2006GB002900.

Macovei, V. A., Hartman, S. E., Schuster, U., Torres-Valdés, S., Moore, C. M., and Sanders, R. J. Impact of physical and biological processes on temporal variations of the ocean carbon sink in the mid-latitude North Atlantic (2002–2016). *Prog. Oceanogr.*, 180(September 2019):102223, 2020. ISSN 00796611. doi: 10.1016/j.pocean.2019.102223. URL `https://doi.org/10.1016/j.pocean.2019.102223`.

Marsh, R., Josey, S. A., de Cuevas, B. A., Redbourn, L. J., and Quartly, G. D. Mechanisms for recent warming of the North Atlantic: Insights gained with an eddy-permitting model. *Journal of Geophysical Research: Oceans*, 113(4):1–21, 2008. ISSN 21699291. doi: 10.1029/2007JC004096.

McKinley, G. A., Pilcher, D. J., Fay, A. R., Lindsay, K., Long, M. C., and Lovenduski, N. S. Timescales for detection of trends in the ocean carbon sink. *Nature*, 530(7591):469–472, 2016. ISSN 14764687. doi: 10.1038/nature16958.

McKinley, G. A., Fay, A. R., Eddebbar, Y. A., Gloege, L., and Lovenduski, N. S. External Forcing Explains Recent Decadal Variability of the Ocean Carbon Sink. *AGU Advances*, 1(2), 2020. ISSN 2576-604X. doi: 10.1029/2019av000149.

NASA. Chlorophyll, 2021. `https://earthobservatory.nasa.gov/global-maps/MY1DMM_CHLORA` [accessed 19.06.2021].

NOAA. Historical El Nino / La Nina episodes (1950-present), 2021a. `https://origin.cpc.ncep.noaa.gov/products/analysis_monitoring/ensostuff/ONI_v5.php` [accessed 25.06.2021].

NOAA. Monitoring CO_2 at Mauna Loa, Hawaii, 2021b. `https://gml.noaa.gov/ccgg/trends/weekly.html` [accessed 25.06.2021].

Orr, J. C. and Epitalon, J. M. Improved routines to model the ocean carbonate system: Mocsy 2.0. *Geoscientific Model Development*, 8(3):485–499, 2015. ISSN 19919603. doi: 10.5194/gmd-8-485-2015.

Orr, J. C., Najjar, R. G., Aumont, O., Bopp, L., Bullister, J. L., Danabasoglu, G., Doney, S. C., Dunne, J. P., Dutay, J. C., Graven, H., Griffies, S. M., John, J. G., Joos, F., Levin, I., Lindsay, K., Matear, R. J., McKinley, G. A., Mouchet, A., Oschlies, A., Romanou, A., Schlitzer, R., Tagliabue, A., Tanhua, T., and Yool, A. Biogeochemical protocols and diagnostics for the CMIP6 Ocean Model Intercomparison Project (OMIP). *Geoscientific Model Development*, 10(6):2169–2199, 2017. ISSN 19919603. doi: 10.5194/gmd-10-2169-2017.

Rahmstorf, S., Box, J. E., Feulner, G., Mann, M. E., Robinson, A., Rutherford, S., and Schaffernicht, E. J. Exceptional twentieth-century slowdown in Atlantic Ocean overturning circulation. *Nature Climate Change*, 5(5):475–480, 2015. ISSN 17586798. doi: 10.1038/nclimate2554.

Resplandy, L., Keeling, R. F., Rödenbeck, C., Stephens, B. B., Khatiwala, S., Rodgers, K. B., Long, M. C., Bopp, L., and Tans, P. P. Revision of global carbon fluxes based on a reassessment of oceanic and riverine carbon transport. *Nature Geoscience*, 11(7):504–509, 2018. ISSN 17520908. doi: 10.1038/s41561-018-0151-3. URL `http://dx.doi.org/10.1038/s41561-018-0151-3`.

Rödenbeck, C., Bakker, D. C., Gruber, N., Iida, Y., Jacobson, A. R., Jones, S., Landschützer, P., Metzl, N., Nakaoka, S., Olsen, A., Park, G. H., Peylin, P., Rodgers, K. B., Sasse, T. P., Schuster, U., Shutler, J. D., Valsala, V., Wanninkhof, R., and Zeng, J. Data-based estimates of the ocean carbon sink variability - First results of the Surface Ocean pCO2 Mapping intercomparison (SOCOM). *Biogeosciences*, 12(23):7251–7278, 2015. ISSN 17264189. doi: 10.5194/bg-12-7251-2015.

Roxy, M. K., Ritika, K., Terray, P., and Masson, S. The curious case of Indian Ocean warming. *Journal of Climate*, 27(22):8501–8509, 2014. ISSN 08948755. doi: 10.1175/JCLI-D-14-00471.1.

Sabine, C. L., Feely, R. A., Gruber, N., Key, R. M., Lee, K., Bullester, J. L., Wanninkhof, R., Wong, C. S., Wallace, D. W. R., Tilbrook, B., Millero, F. J., Peng, T.-H., Kozyr, A., Ono, T., and Rios, A. F. The oceanic sink for anthropogenic CO_2. *Science*, 305(July):367–371, 2004.

Sarmiento, J. L. and Gruber, N. Sinks for anthropogenic carbon. *Physics Today*, 55(8):30, 2002. ISSN 00319228. doi: 10.1063/1.1510279.

Sarmiento, J. L. and Gruber, N. *Ocean Biogeochemical Dynamics*. Princeton University Press, 2006. ISBN 9780691017075.

Schourup-Kristensen, V., Sidorenko, D., Wolf-Gladrow, D. A., and Völker, C. A skill assessment of the biogeochemical model REcoM2 coupled to the finite element sea ice-ocean model (FESOM 1.3). *Geoscientific Model Development*, 7(6):2769–2802, 2014. ISSN 19919603. doi: 10.5194/gmd-7-2769-2014.

Schourup-Kristensen, V., Wekerle, C., Wolf-Gladrow, D. A., and Völker, C. Arctic Ocean biogeochemistry in the high resolution FESOM 1.4-REcoM2 model. *Prog. Oceanogr.*, 168(September):65–81, 2018. ISSN 00796611. doi: 10.1016/j.pocean.2018.09.006. URL `https://doi.org/10.1016/j.pocean.2018.09.006`.

Schwalm, C. R., Williams, C. A., Schaefer, K., Baker, I., Collatz, G. J., and Rödenbeck, C. Does terrestrial drought explain global CO 2 flux anomalies induced by El Niño? *Biogeosciences*, 8(9):2493–2506, 2011. ISSN 17264170. doi: 10.5194/bg-8-2493-2011.

Solomon, S., Plattner, G.-K., Knutti, R., and Friedlingstein, P. Irreversible climate change due to carbon dioxide emissions. *Proceedings of the National Academy of Sciences*, 106(6):1704–1709, 2009. ISSN 0027-8424. doi: 10.1073/pnas.0812721106.

Takahashi, T., Olafsson, J., Goddard, J. G., Chipman, D. W., and Sutherland, S. C. Seasonal variation of co2 and nutrients in the high-latitude surface oceans: A comparative study. *Global Biogeochemical Cycles*, 7(4):843–878, 1993. doi: https://doi.org/10.1029/93GB02263.

Thompson, D. W. J., Solomon, S., Kushner, P. J., England, M. H., Grise, K. M., and Karoly, D. J. Signatures of the antarctic ozone hole in southern hemisphere surface climate change. *Nature Geoscience*, 4(11):741–749, 2011. doi: 10.1038/ngeo1296.

Tsujino, H., Urakawa, S., Nakano, H., Small, R. J., Kim, W. M., Yeager, S. G., Danabasoglu, G., Suzuki, T., Bamber, J. L., Bentsen, M., Böning, C. W., Bozec, A., Chassignet, E. P., Curchitser, E., Boeira Dias, F., Durack, P. J., Griffies, S. M., Harada, Y., Ilicak, M., Josey, S. A., Kobayashi, C., Kobayashi, S., Komuro, Y., Large, W. G., Le Sommer, J., Marsland, S. J., Masina, S., Scheinert, M., Tomita, H., Valdivieso, M., and Yamazaki, D. JRA-55 based surface dataset for driving ocean–sea-ice models (JRA55-do). *Ocean Modelling*, 130(July):79–139, 2018. ISSN 14635003. doi: 10.1016/j.ocemod.2018.07.002.

Völker, C., Wallace, D. W., and Wolf-Gladrow, D. A. On the role of heat fluxes in the uptake of anthropogenic carbon in the North Atlantic. *Global Biogeochemical Cycles*, 16(4):85–1–85–9, 2002. ISSN 08866236. doi: 10.1029/2002gb001897.

Wang, Q., Danilov, S., Sidorenko, D., Timmermann, R., Wekerle, C., Wang, X., Jung, T., and Schröter, J. The Finite Element Sea Ice-Ocean Model (FESOM) v.1.4: Formulation of an ocean general circulation model. *Geoscientific Model Development*, 7(2):663–693, 2014. ISSN 19919603. doi: 10.5194/gmd-7-663-2014.

Wanninkhof, R., Park, G. H., Takahashi, T., Sweeney, C., Feely, R., Nojiri, Y., Gruber, N., Doney, S. C., McKinley, G. A., Lenton, A., Le Quere, C., Heinze, C., Schwinger, J., Graven, H., and Khatiwala, S. Global ocean carbon uptake: Magnitude, variability and trends. *Biogeosciences*, 10 (3):1983–2000, 2013. ISSN 17264170. doi: 10.5194/bg-10-1983-2013.

Wanninkhof, R. Relationship between wind speed and gas exchange over the ocean revisited. *Limnology and Oceanography: Methods*, 12(JUN):351–362, 2014. ISSN 15415856. doi: 10.4319/lom.2014.12.351.

Chapter 7

Supplementary Material

7.1 Mean and trend in the CO_2 flux for all simulations

Supplementary figures for Section 4.1.

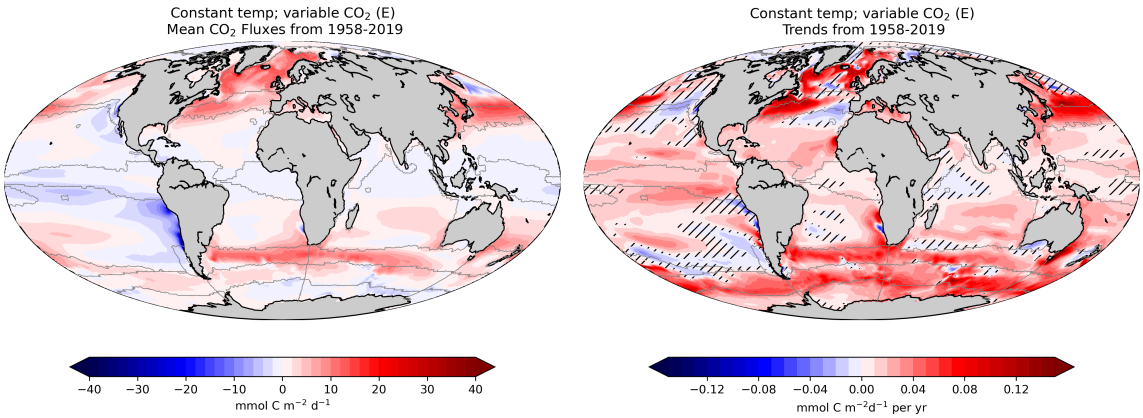

(a)

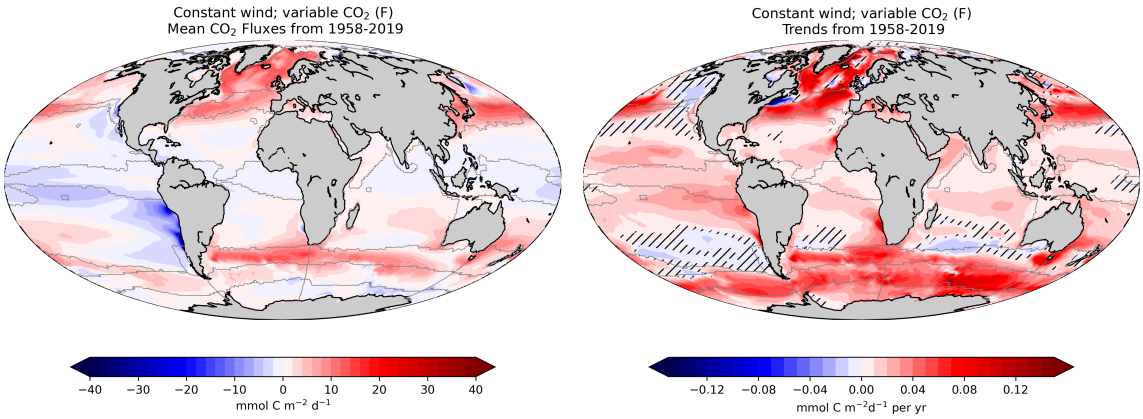

(b)

Figure S1: Mean and trends of CO_2 flux density in sim-E and sim-F. Positive denotes a flux into the ocean. Hashed areas indicate low significance of trends (p-values greater than 0.05.)

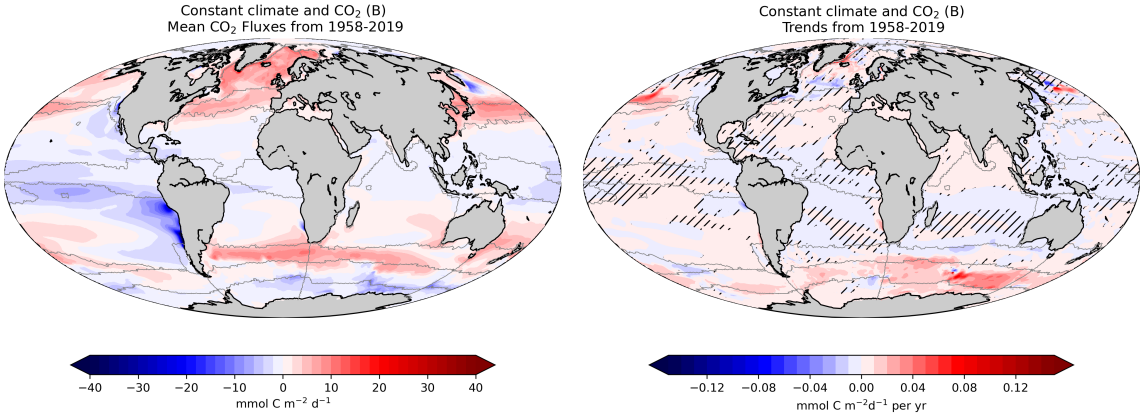

(a)

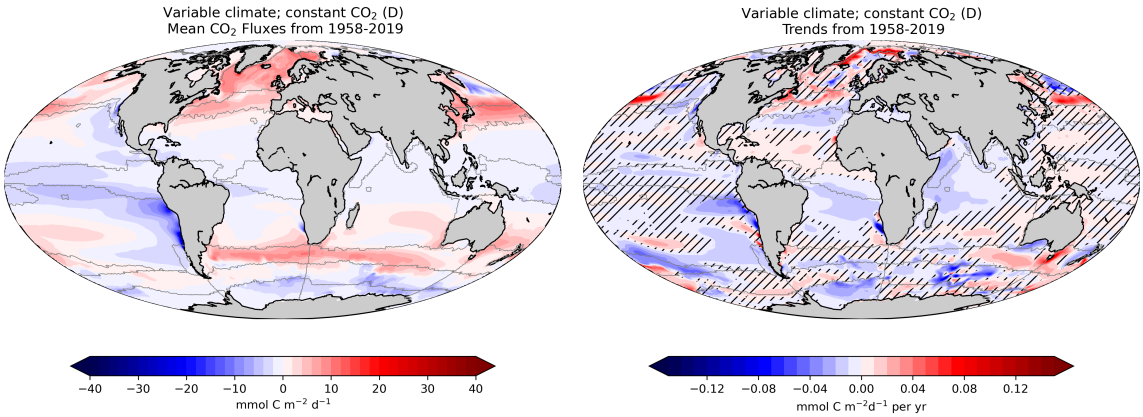

(b)

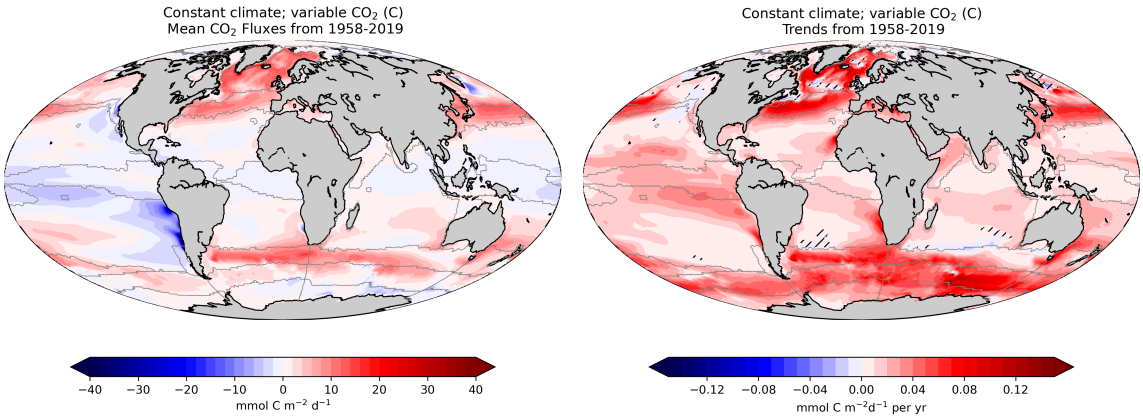

(c)

Figure S2: Mean and trends of CO_2 flux density in sim-D and sim-C. Positive denotes a flux into the ocean. Hashed areas indicate low significance of trends (p-values greater than 0.05.)

7.2 Increase of the buffer factor in simulation A

Most of the CO_2 that dissolves in seawater is chemically transformed through a reaction with water molecules. Thereby, bicarbonate HCO_3^- and carbonate CO_3^{2-} are formed. Thus, the dissolved CO_2 (i.e. carbonic acid H_2CO_3) is largely eliminated, so that a low pCO_2^O is maintained, which allows for the uptake of more atmospheric CO_2. This capacity of the ocean to absorb carbon, but to undergo only small changes pCO_2^O in the process, is described by the ocean's buffer factor γ_{DIC} (see Equation (3.34), Sarmiento and Gruber (2006).)

Regions with a low buffer factor maintain stable pCO_2^O at comparatively large changes of DIC. The buffer factor is determined by DIC and alkalinity (Equation (3.35)) and because the global distribution of alkalinity is relatively uniform, the geographical distribution γ_{DIC} follows mainly DIC with low γ_{DIC} in warm waters and high γ_{DIC} in cold regions (γ_{DIC}: Figure S4a, DIC: Figure 4.12a). This is why the tropics are quite efficient at taking up anthropogenic carbon (0.5-1.5 mmol C $d^{-1}m^{-2}$) even though they don't provide a pathway for the removal of anthropogenic carbon into the deep. However, as described in Section 4.1, the extratropical regions which provide such a pathway either through export production or transport with the circulation, take up anthropogenic carbon even more efficiently (1.5-4 mmol C $d^{-1}m^{-2}$ per yr.)

According to Sarmiento and Gruber (2006) and Egleston et al. (2010), γ_{DIC} increases with DIC, reaches a maximum at DIC=Alk and declines after. Fassbender et al. (2017) have raised the question how sensitive γ_{DIC} is to the anthropogenic enhancement of DIC, if and when the maximum of γ_{DIC} at DIC=Alk will be reached and how this impacts the oceanic carbon sink. Figure S3 shows that the global mean γ_{DIC} has almost linearly grown and increased by 1.2 since the beginning of the timeseries. Despite the globally relatively uniform increase in DIC (Figure 4.16a), the increase of γ_{DIC} is highest at high latitudes (Figure S4b and Figure S3.), which confirms that the sensitivity of γ_{DIC} to rising pCO_2^A is higher in colder, fresher waters (Fassbender et al., 2017). Contradictory to that, Figure S4b shows that trends in γ_{DIC} are smallest in the ICE biome. Here, γ_{DIC} has already reached maximum values. However, this result is probably a false outcome resulting from the discontinuity of the equation that was used to calculate γ_{DIC} (Equation (3.35)). In fact, Fassbender et al. (2017) observe that in the current ocean, γ_{DIC} has not reached maximum values yet.

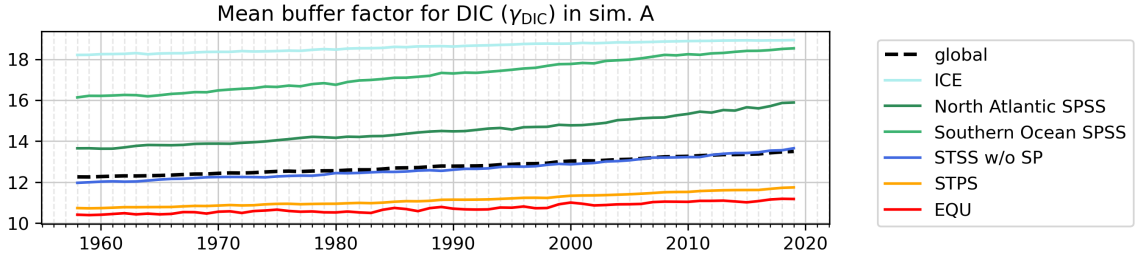

Figure S3: Timeseries of the global mean buffer factor for DIC in sim-A (bold black dashed line) and the same for regional means (colored lines).

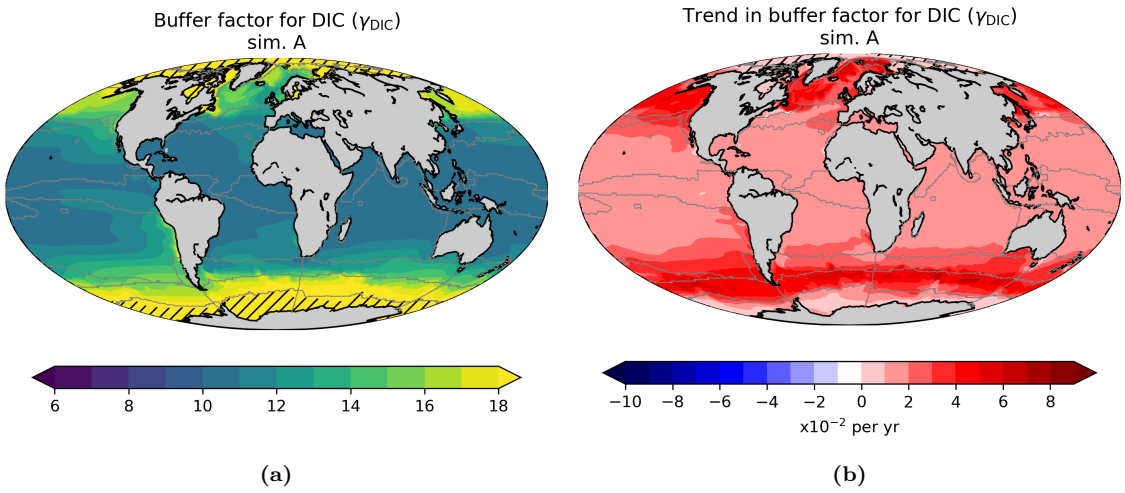

(a) **(b)**

Figure S4: The left panel shows the mean buffer factor for DIC in sim-A. Hatched areas indicate that more than 50% of the values there exceeded the threshold value of 19 and were set 19. The right panel shows the trend in the buffer factor. Hatched areas indicate a low significance of the trend.

7.3 Global mean ΔpCO_2 and the direction of the CO_2 flux

The gradient ΔpCO_2 is defined as $pCO_2^A - pCO_2^A$. In sim-C, the global mean pCO_2^O is higher than the global mean pCO_2^A (thus, ΔpCO_2 is negative) for most of the time period. This changes only after the beginning of the 2000s. At first, it might appear contra-intuitive why the global ocean would take up carbon despite that the global mean pCO_2^O ocean is higher than the mean pCO_2^A. Wouldn't pCO_2^O seek to be in balance with pCO_2^A, thus requiring for an outgassing to decrease pCO_2^O? To understand this, we need to consider the geographical distribution and high regional variability of pCO_2^O. There are extensive areas where pCO_2^O is higher than pCO_2^A. These areas are found mainly in the tropics and subtropics, where the outgassing per surface area is weak despite the relatively strong negative pCO_2 gradient. This is because in the tropics and subtropics, the high temperatures reduce the gas transfer coefficient. Furthermore, pCO_2^O is also often much higher than pCO_2^A in ice-covered regions, where the ice cover prevents CO_2 fluxes. In contrast, the regions where the ocean takes up carbon due to a positive pCO_2 gradient cover a smaller area, but are more efficient. They are found in the subpolar region, where cold surface temperatures and high wind velocities result in high gas transfer coefficients. This is why the global CO_2 flux in FESOM-REcoM is zero in a state in which the global mean pCO_2^O is higher than pCO_2^A (at approximately $\Delta pCO_2 = -3.63\mu atm$ in sim-B, which has a global mean CO_2 flux close to zero).

7.4 Miscellaneous

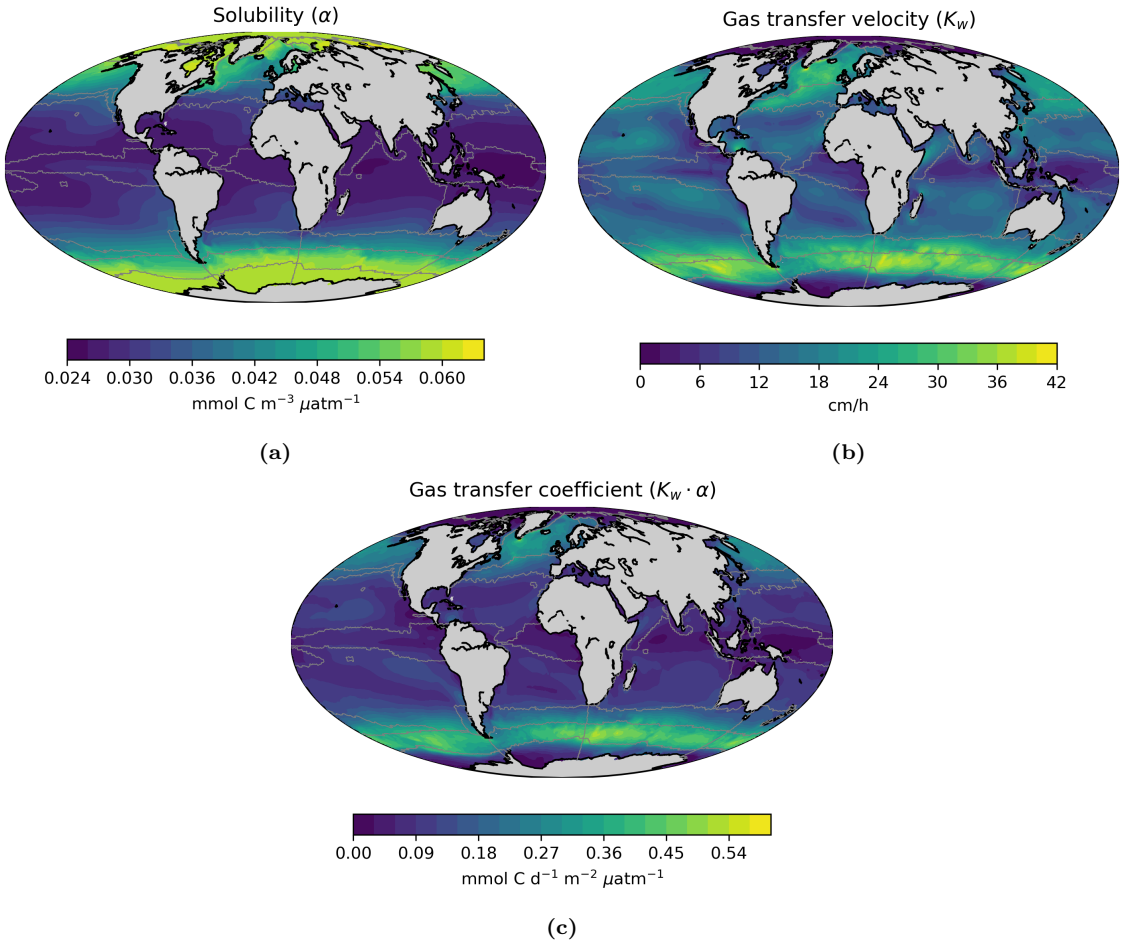

Figure S5: In sim-A: (a) The mean solubility of CO_2 (α, Equation (3.26)) available from the model output. (b) The mean gas transfer velocity (k_w, Equation (3.18)) available from the model output. (c) The mean gas transfer coefficient ($k_w \cdot \alpha$) calculated offline from monthly values.

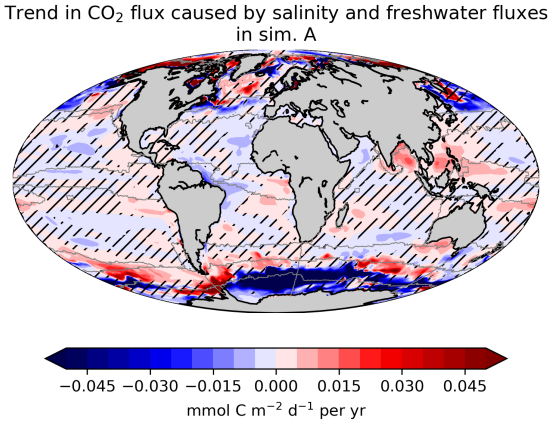

Figure S6: The trend in CO_2 flux density that is expected from the trend in salinity and freshwater fluxes in sim-A, where positive denotes a trend towards more uptake. Hatched areas indicate low significance (p-values greater than 0.05.)

7.5 Effect of circulation and biology on sDIC

Supplementary figures for Section 4.2.10.

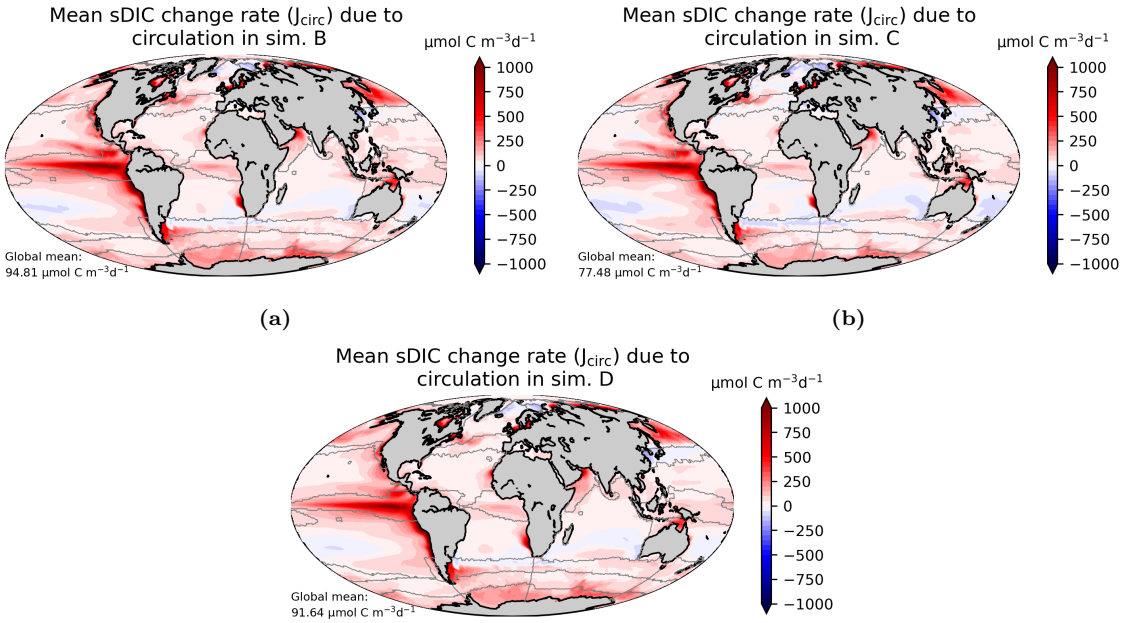

Figure S7: Temporal mean of carbon transport with the circulation per volume of mixed surface water in simulation B, C and D. Positive flux corresponds to an increase in surface DIC, i.e. positive is either from the depth or horizontally from adjacent regions into the mixed layer.

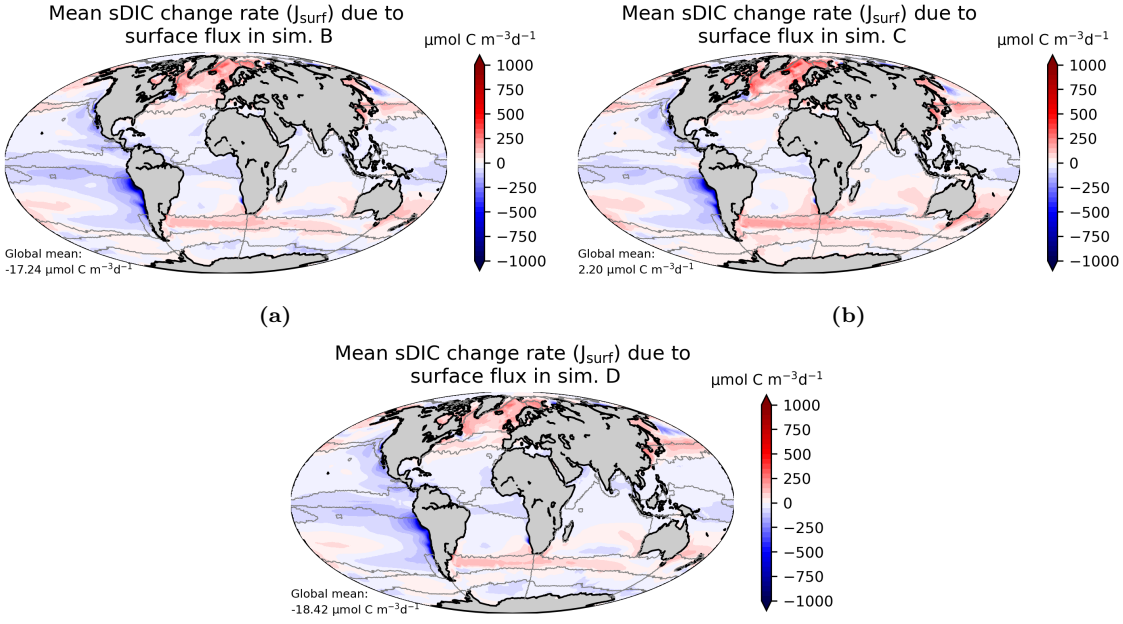

Figure S8: Temporal mean of air-sea carbon fluxes per volume of mixed surface water in simulations B, C and D. Positive flux corresponds to an increase in surface DIC, i.e. positive is from the atmosphere into the mixed layer.

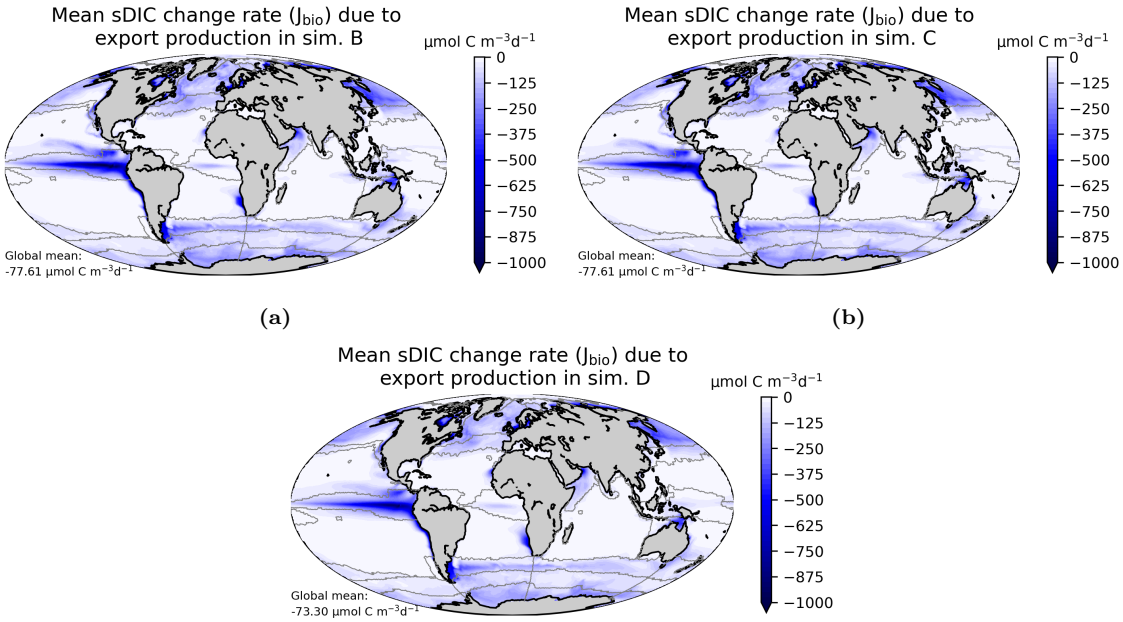

Figure S9: Temporal mean of export production per volume of mixed surface water in simulation B, C and D. Negative flux corresponds to a decrease in surface DIC, i.e. negative is from the mixed layer into the depth.

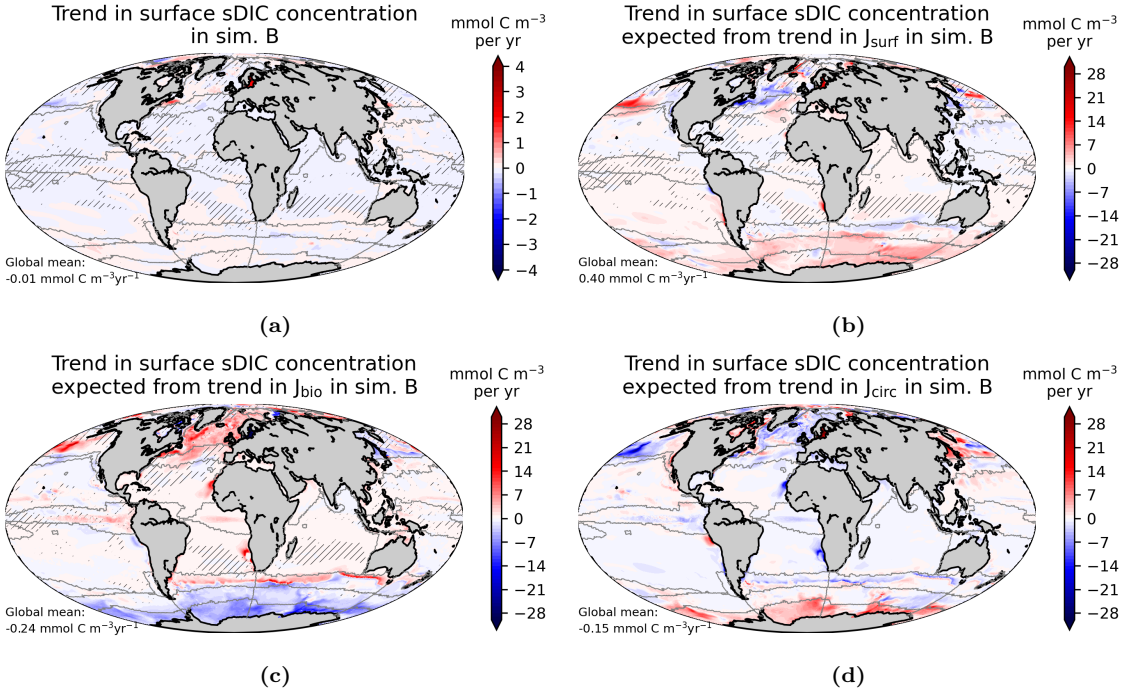

Figure S10: (a) Trend in sDIC concentration in sim-B, i.e. the drift. (b,c,d) The trends in sDIC concentration which are expected from the trends in (b) J_{surf}, (c) J_{bio} and (d) J_{circ} in sim-B, i.e. expected from the drift of the J's. Positive values correspond to an increase in sDIC. Hatched areas mark low significance. In panel (a), there is no information on the significance. The global mean is calculated as the trend in the global mean timeseries, not as the mean of the regional trends.

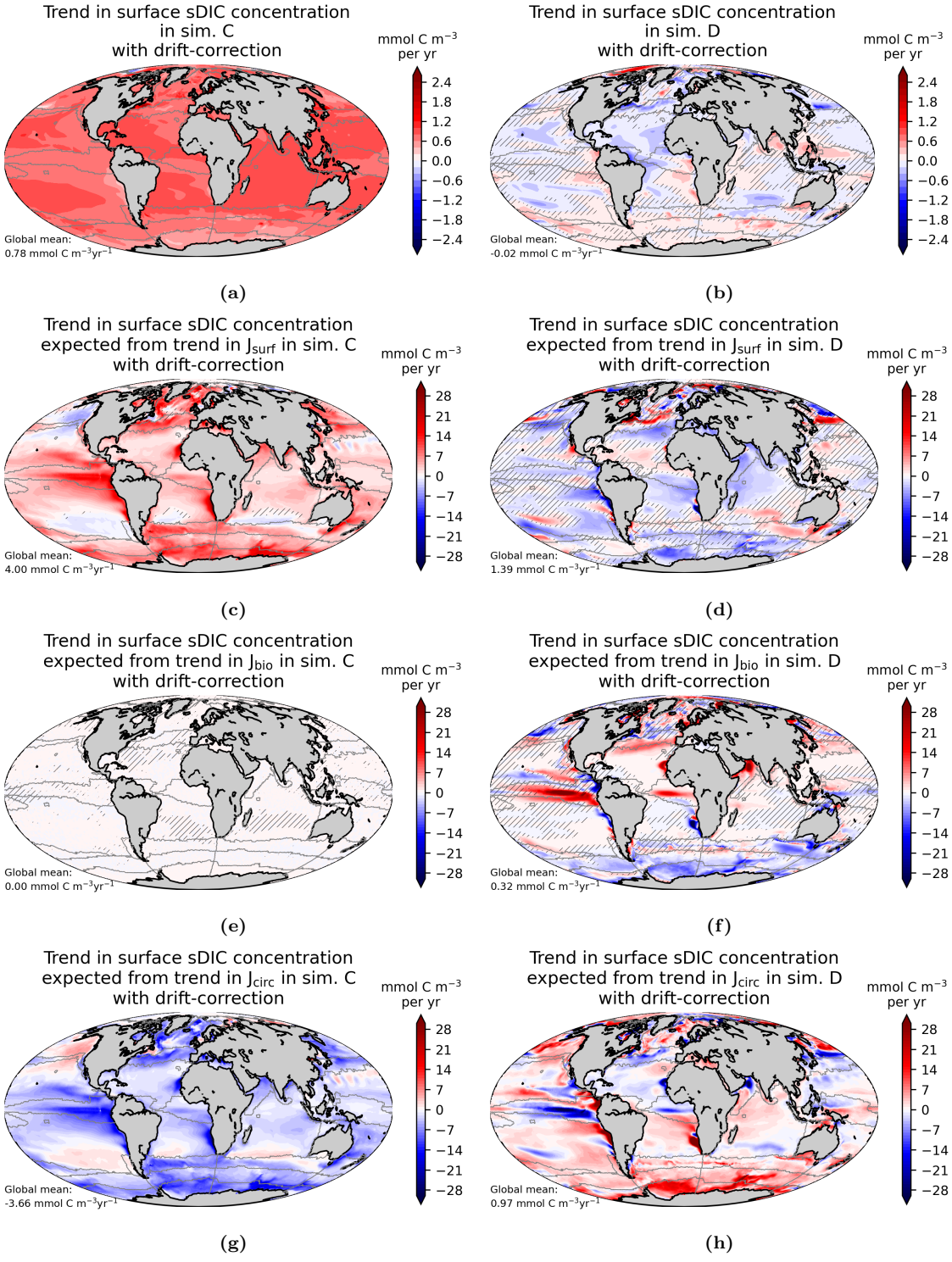

Figure S11: (a,b) Trend in sDIC concentration in sim-C and sim-D with drift correction using sim-B. (c-h) The components of the trend in sDIC concentration due to the trends in (c,d) J_{surf}, (e,f) J_{bio} and (g,h) J_{circ} with drift correction. Positive values correspond to an increase in sDIC. Hatched areas mark low significance. In panels g and h, there is no information on the significance. Trends from sim-B (Figure S10) were subtracted for the drift-correction. The global mean is calculated as the trend in the global mean timeseries, not as the mean of the regional trends.

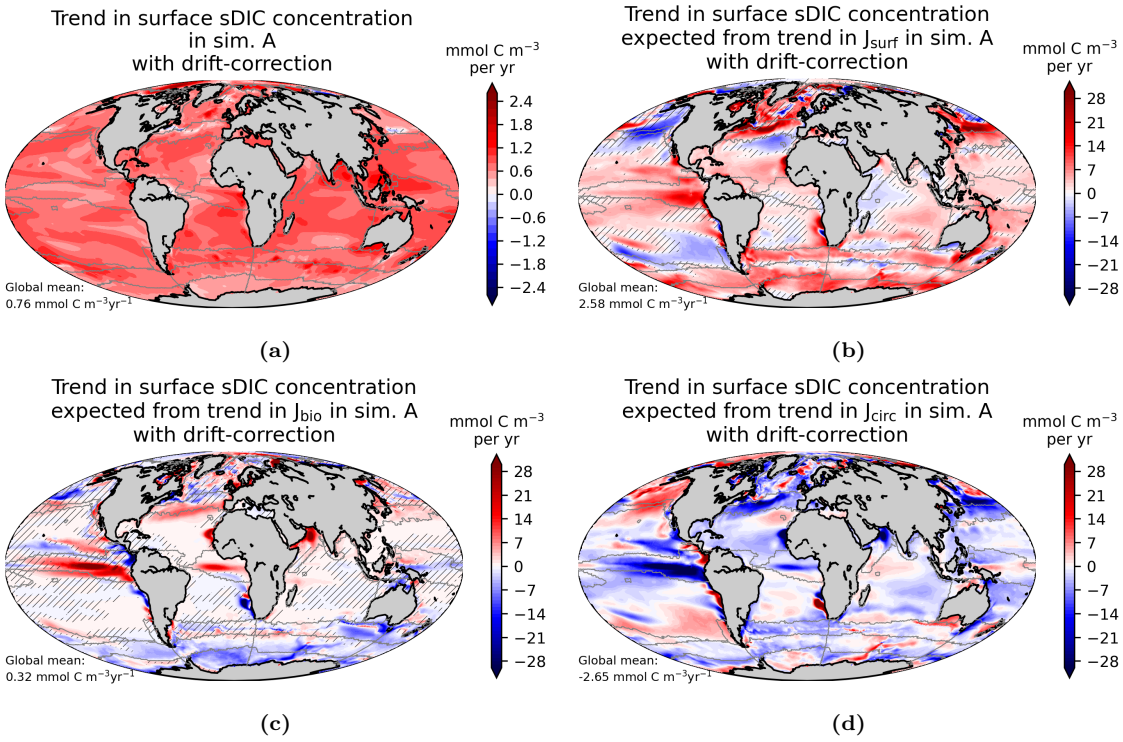

Figure S12: (a) Trend in sDIC concentration in sim-A. (b,c,d) The trends in sDIC concentration which are expected from the trends in (b) J_{surf}, (c) J_{bio} and (d) J_{circ}. Positive values correspond to an increase in sDIC. Hatched areas mark low significance. In panel d, there is no information on the significance. Trends from sim-B (Figure S10) were subtracted for the drift-correction. The global mean is calculated as the trend in the global mean timeseries, not as the mean of the regional trends.

7.6 Impact of climate variability on miscellaneous variables

Supplementary figures for Section 4.3.3.

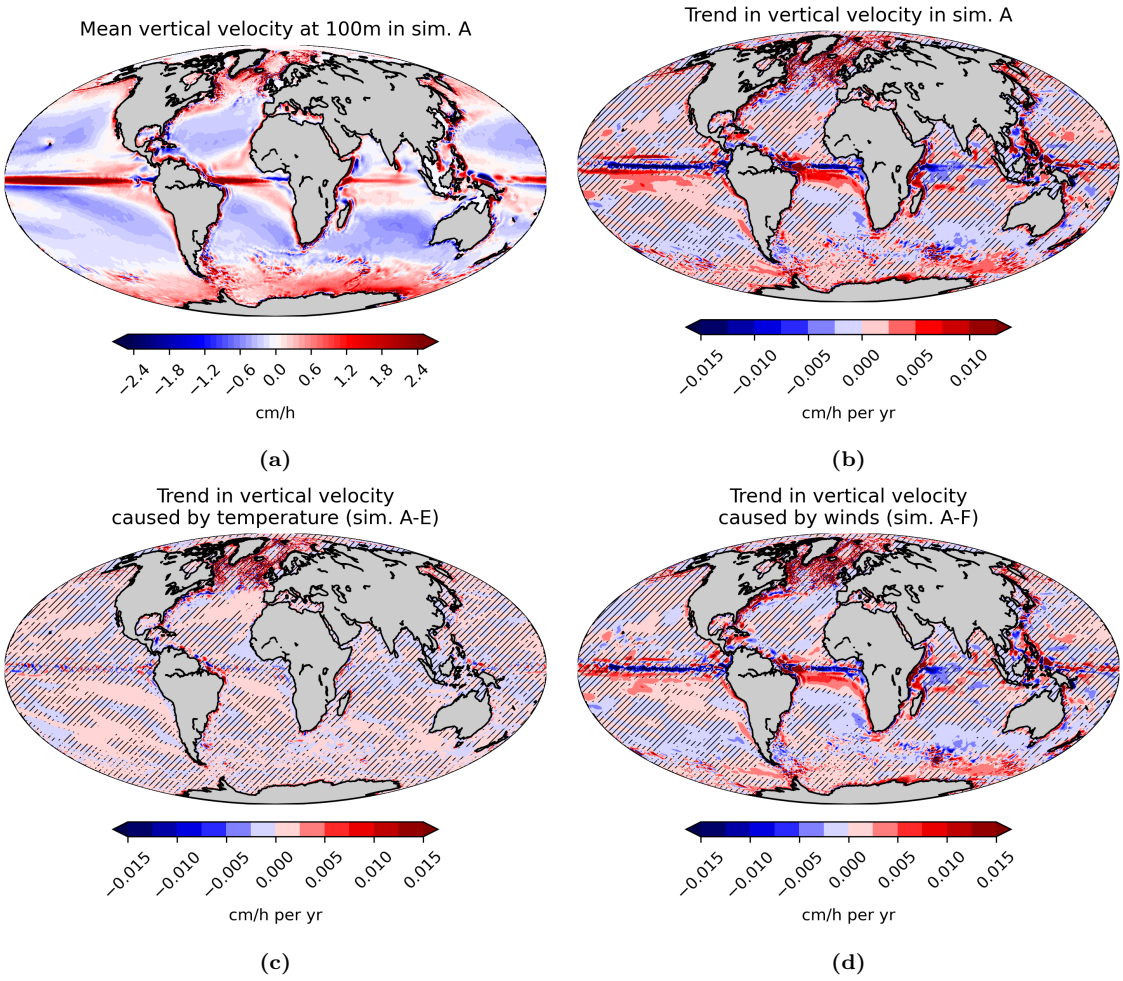

Figure S13: (a) Mean of the vertical velocities at 100m depth in the historical simulation. (b) The trend in vertical velocities in the historical simulation. (c) The impact of sea surface temperature variability on the trend in vertical velocities. (d) The impact of variability in winds on the trend in vertical velocities.

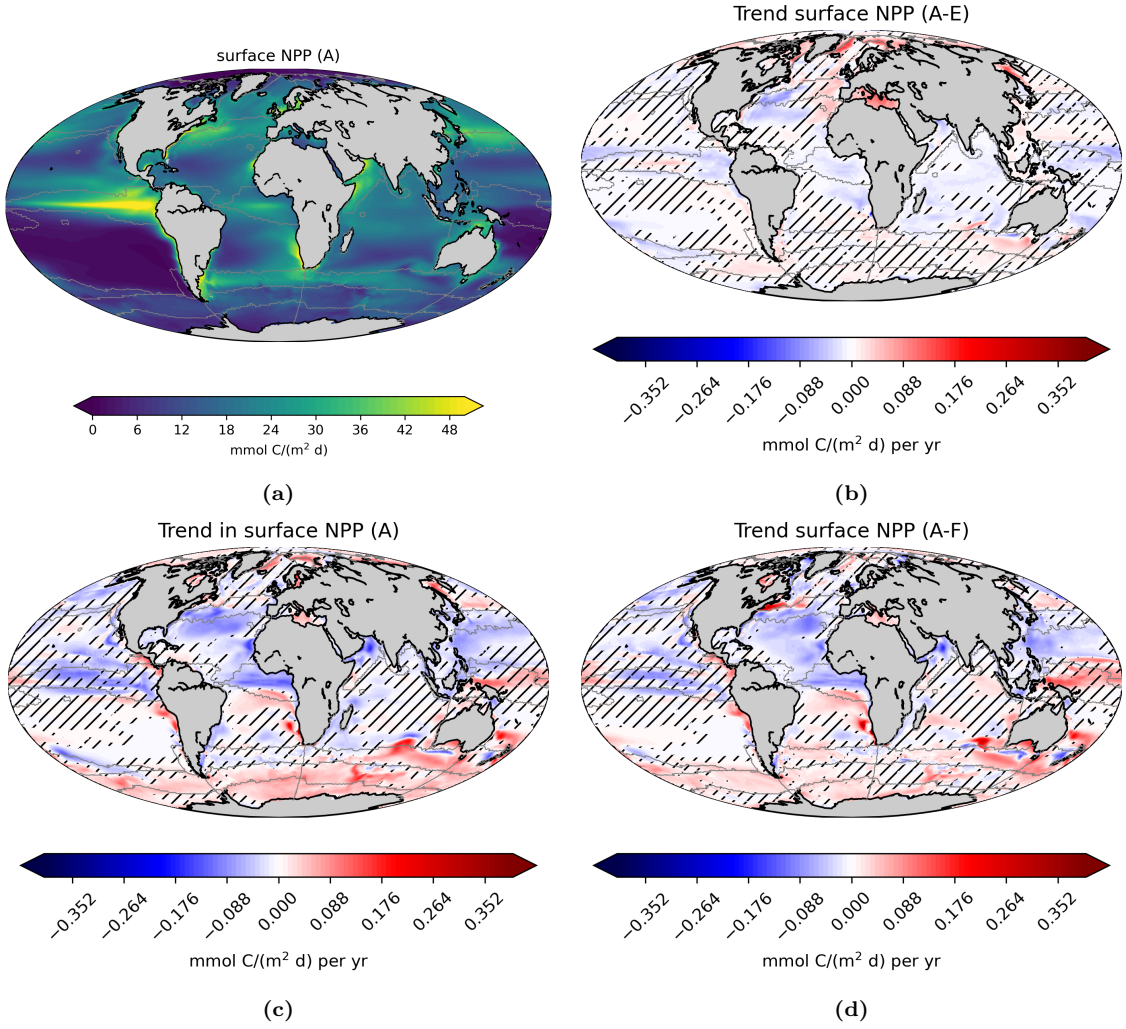

Figure S14: (a) Mean net primary production at the surface in the historical simulation. (b) The trend in the net primary production in the historical simulation. (c) The impact of sea surface temperature variability on the trend in primary production. (d) The impact of variability in winds on the trend in primary production.

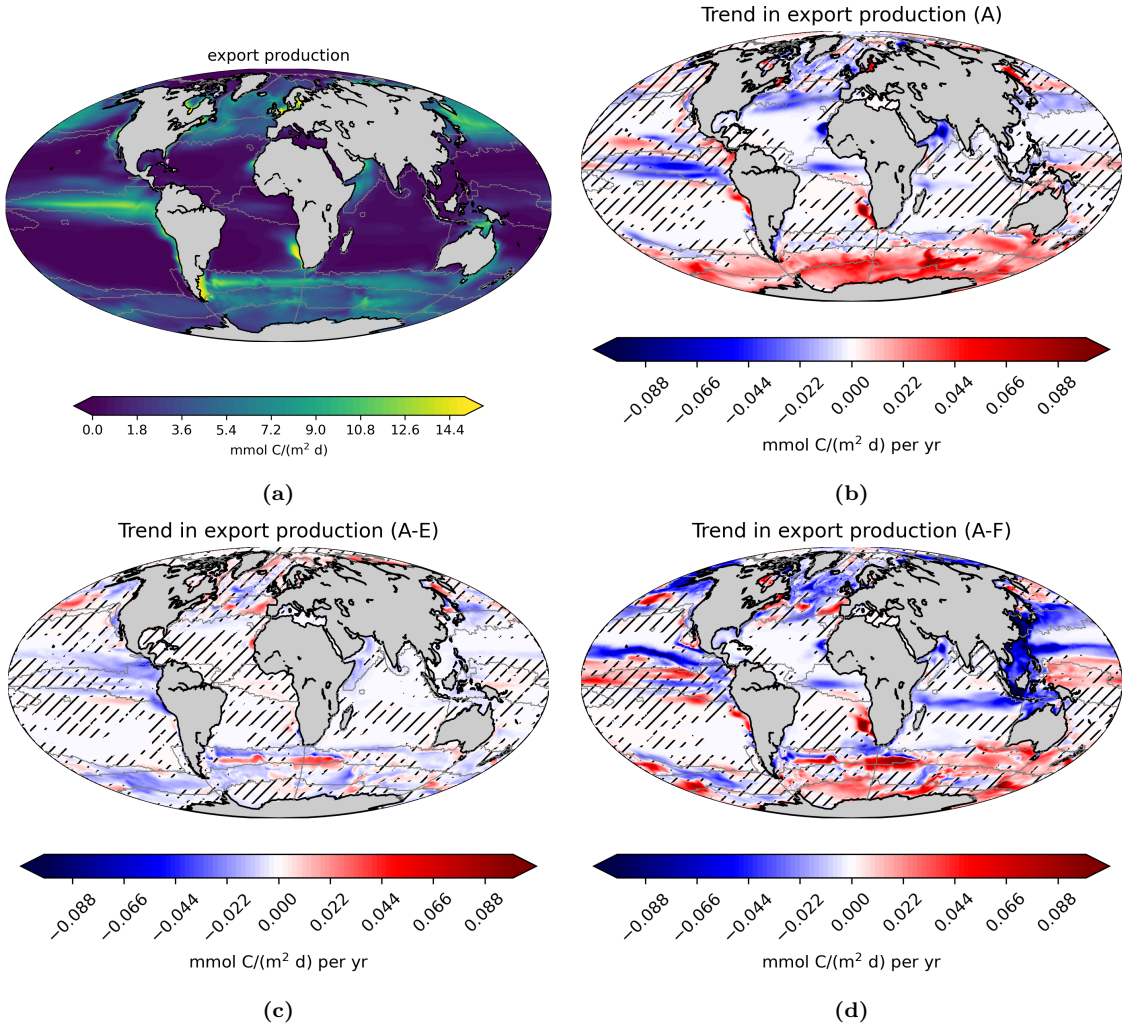

Figure S15: (a) Mean biological export at mixed layer depth directed from the surface into the deep in the historical simulation. (b) The trend in the biological export in the historical simulation. (c) The impact of sea surface temperature variability on the trend in biological export. A positive trend signifies more export of carbon into the deep. (d) The impact of variability in winds on the trend in biological export.

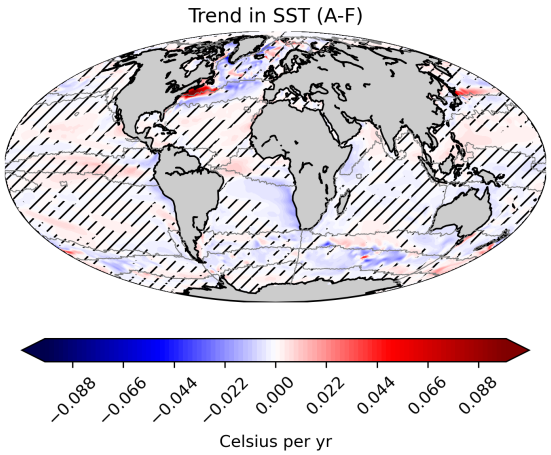

Figure S16: The impact of variability in winds on the trend in the sea surface temperature.

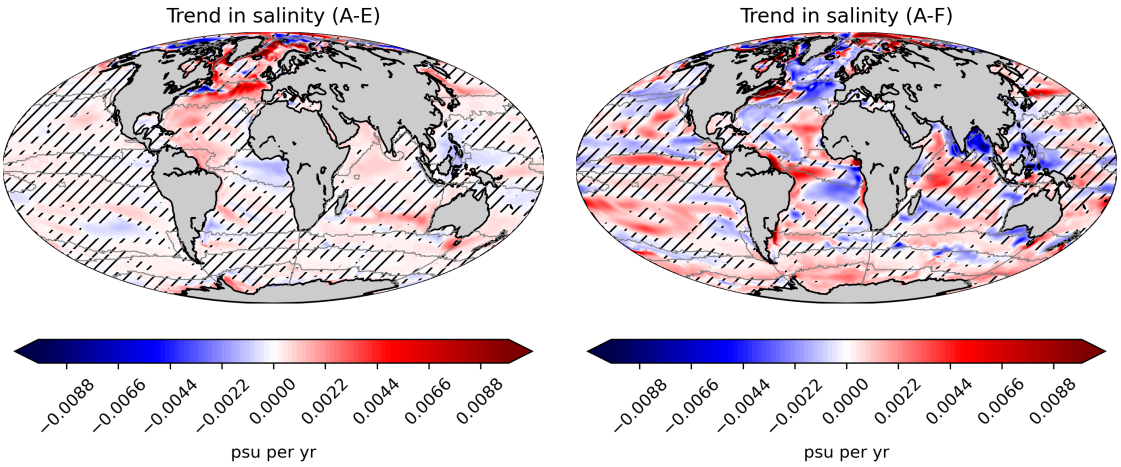

Figure S17: (a) The impact of sea surface temperature variability on the trend in the salinity. (b) The impact of variability in winds on the trend in the salinity.

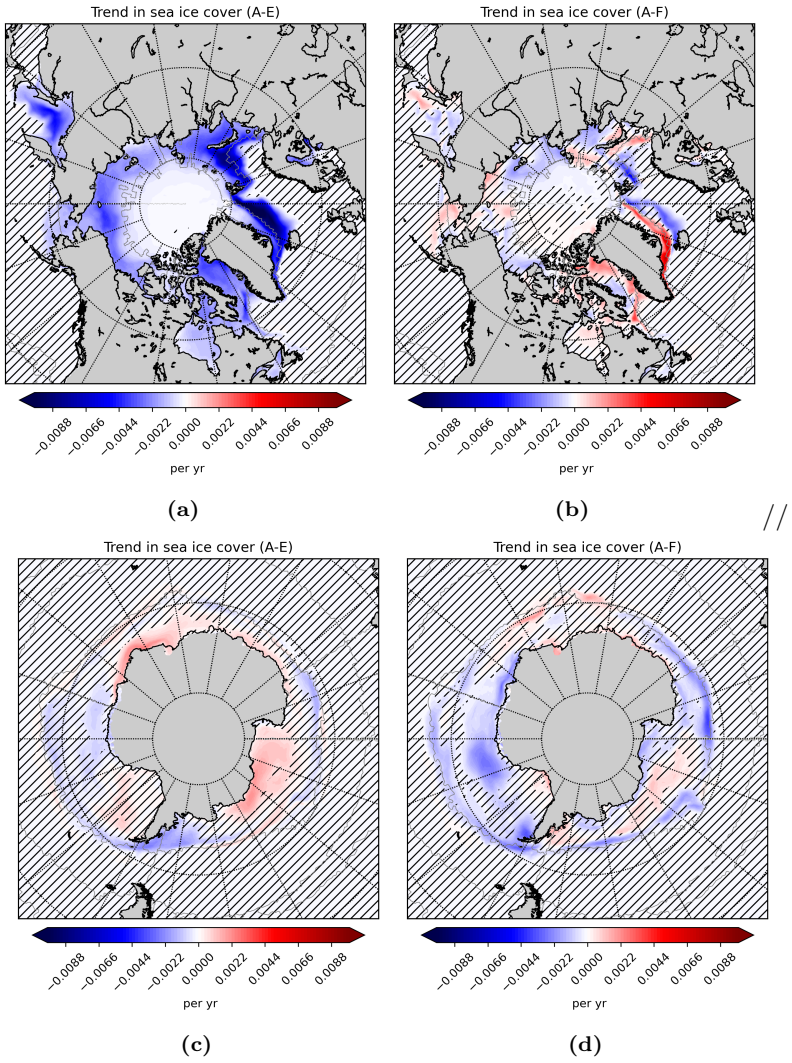

Figure S18: (a,c) The impact of sea surface temperature variability on the trend in the sea ice concentration. (b,d) The impact of variability in winds on the trend in the sea ice concentration.

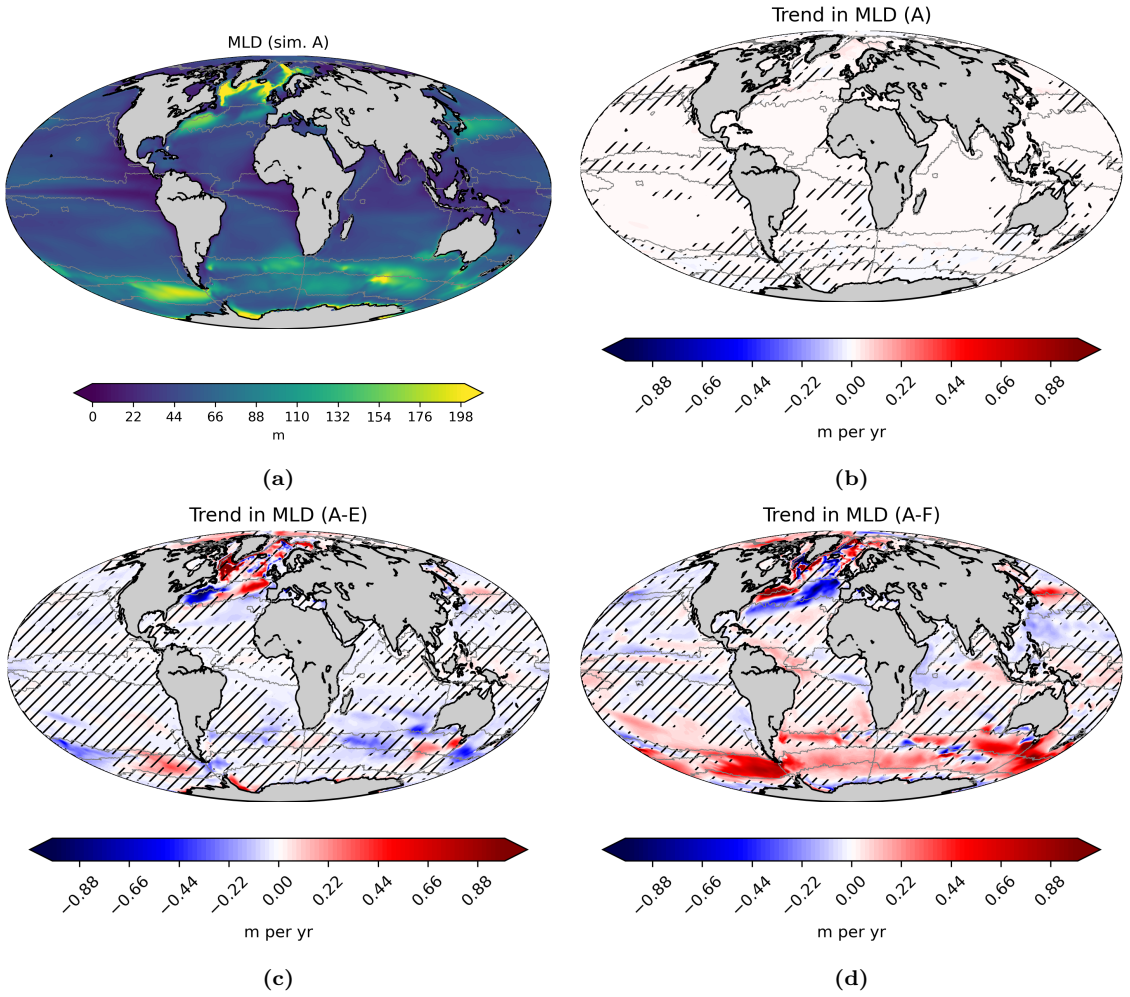

Figure S19: (a) Mean mixed layer depth in the historical simulation. (b) The trend in mixed layer depth in the historical simulation. Positive is a trend towards deeper mixed layers. (c) The impact of sea surface temperature variability on the trend in mixed layer depth. Positive is a trend towards deeper mixed layers. (d) The impact of variability in winds on the trend in mixed layer depth.

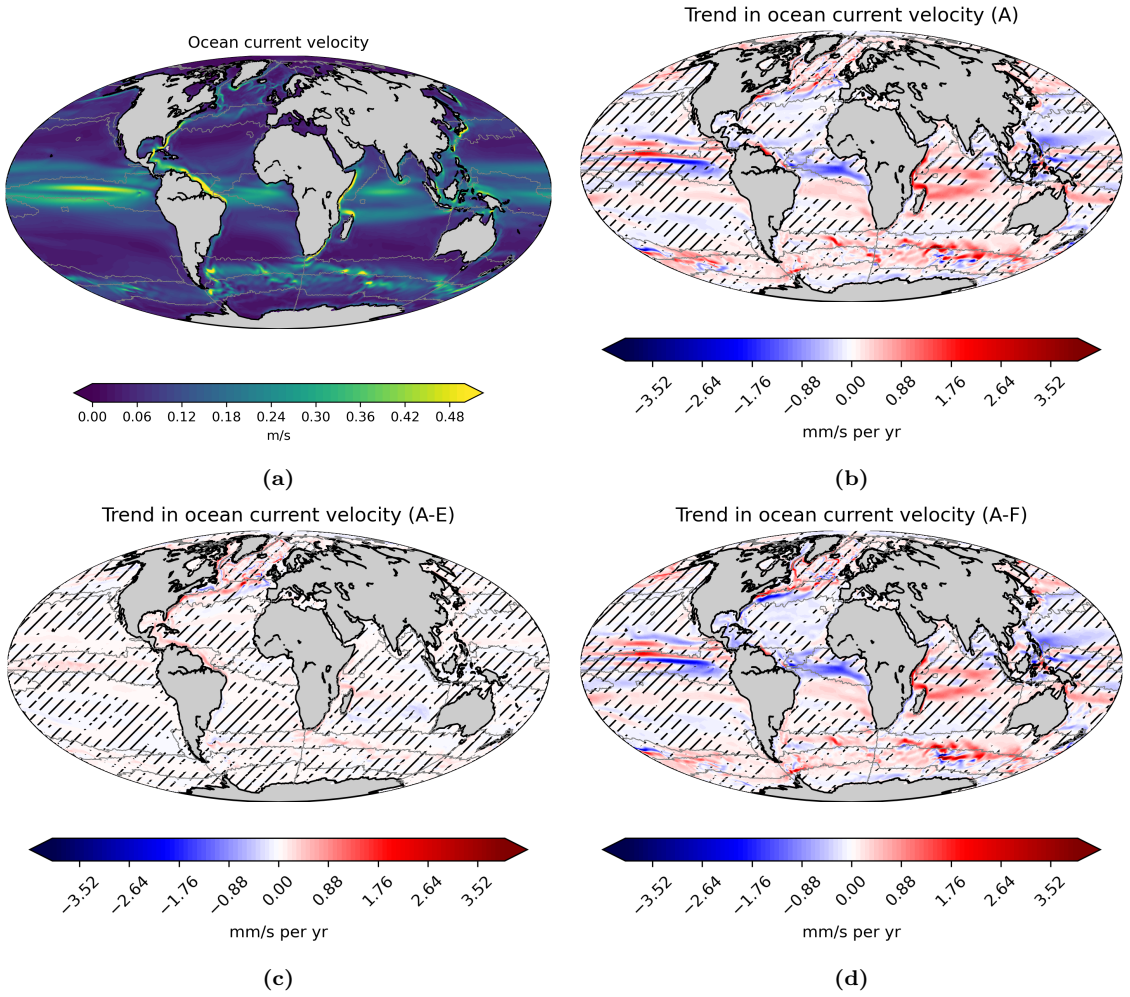

Figure S20: (a) Mean surface velocity in the historical simulation. (b) The trend in the surface velocity in the historical simulation. (c) The impact of sea surface temperature variability on the trend in the surface velocity. (d) The impact of variability in winds on the trend in the surface velocity.

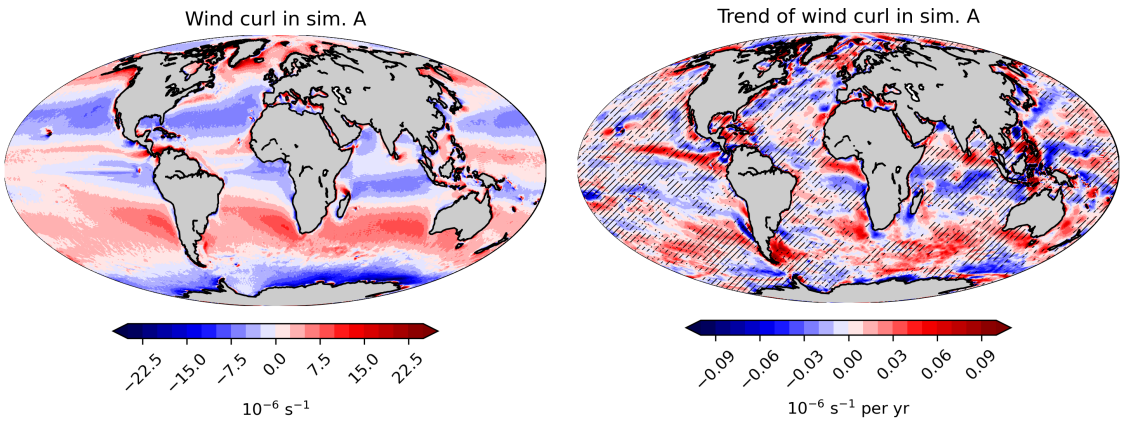

(a) **(b)**

Figure S21: (a) Mean wind curl (from the JRA forcing). (b) Trend in the wind curl (from the JRA forcing).

7.7 Trends in the CO_2 flux biome-wise

7.7.1 Overview of all biomes

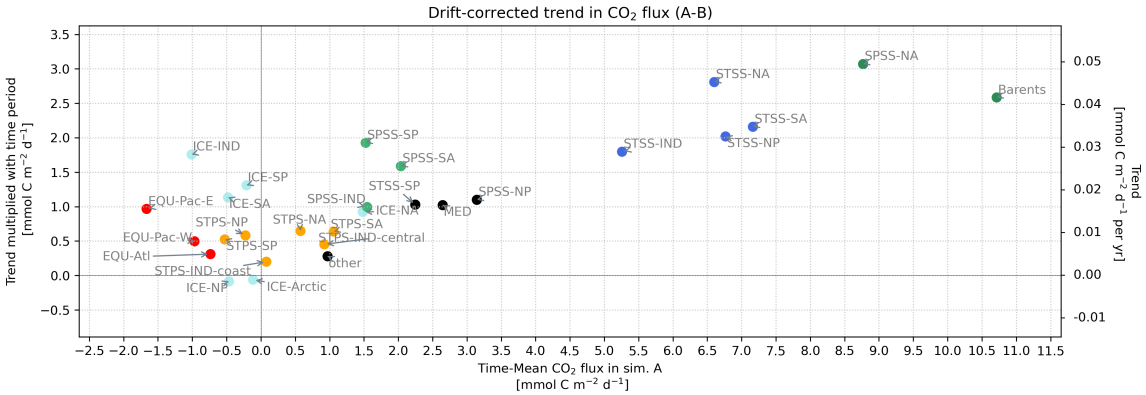

(a)

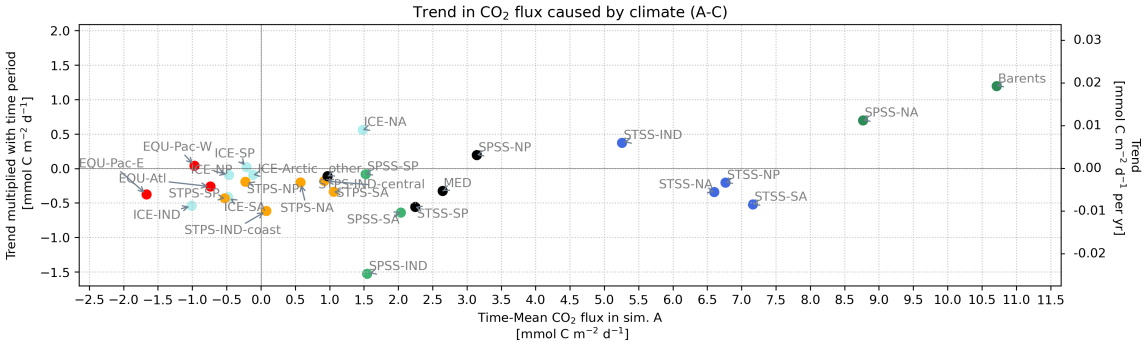

(b)

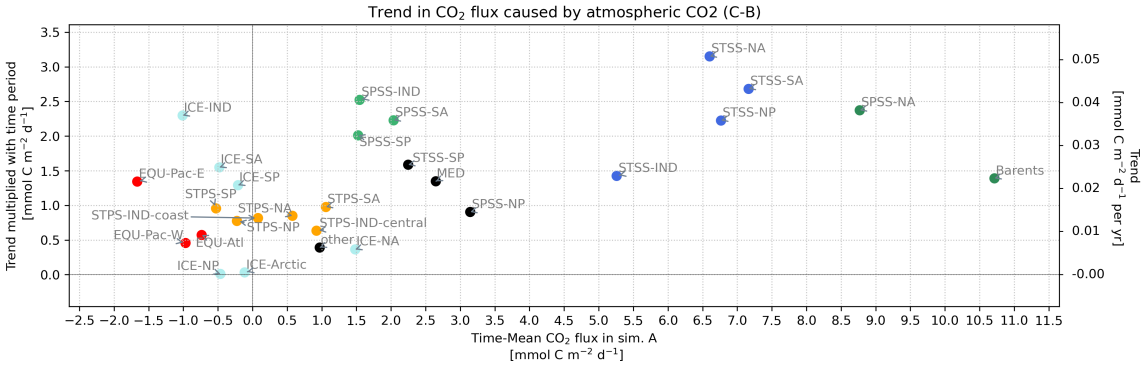

(c)

Figure S22: Mean of CO_2 flux density in sim-A for all sub-regions with (a) drift-corrected trends, (b) trends caused by increase of atmospheric CO_2 and (c) trends caused by climate variability. Axis scaling is chosen so that the x-axis (mean value) and left y-axis (approximate change over the time period 1958-2019) are proportional (1:1).

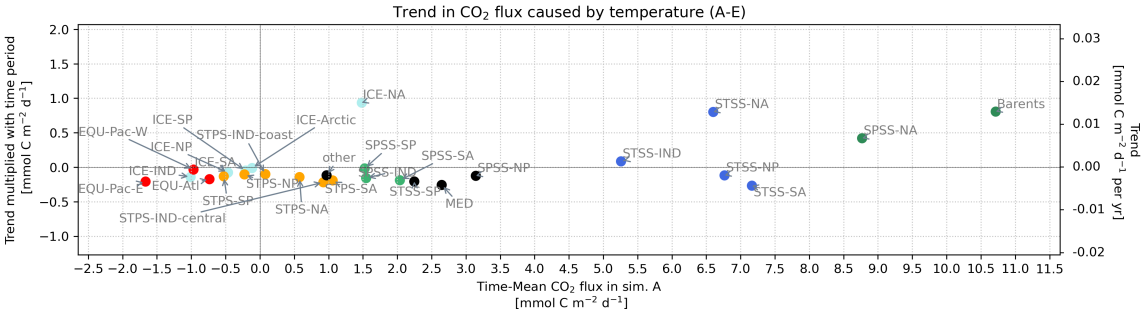

(a)

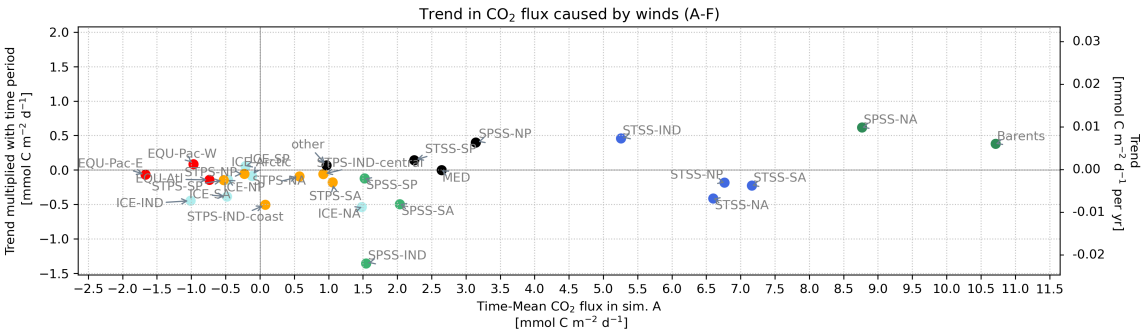

(b)

Figure S23: Mean of CO_2 flux density in sim-A for all sub-regions with (a) trends caused by temperature variability and (b) trends caused by variability in winds. Axis scaling is chosen so that the x-axis (mean value) and left y-axis (approximate change over the time period 1958-2019) are proportional (1:1).

7.7.2 Individual biomes

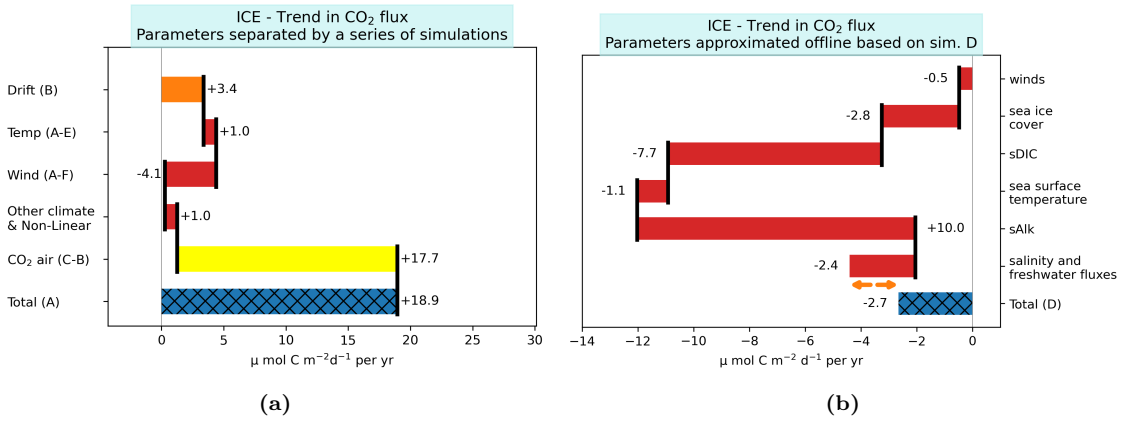

Figure S24: The total trend in the CO_2 flux per surface area (blue hashed bar at the bottom) in the ICE biome (a) in the historical simulation and (b) in the simulation with variable climate and constant CO_2 is decomposed into the parts of the trend which are caused by different parameters (other colorful bars).

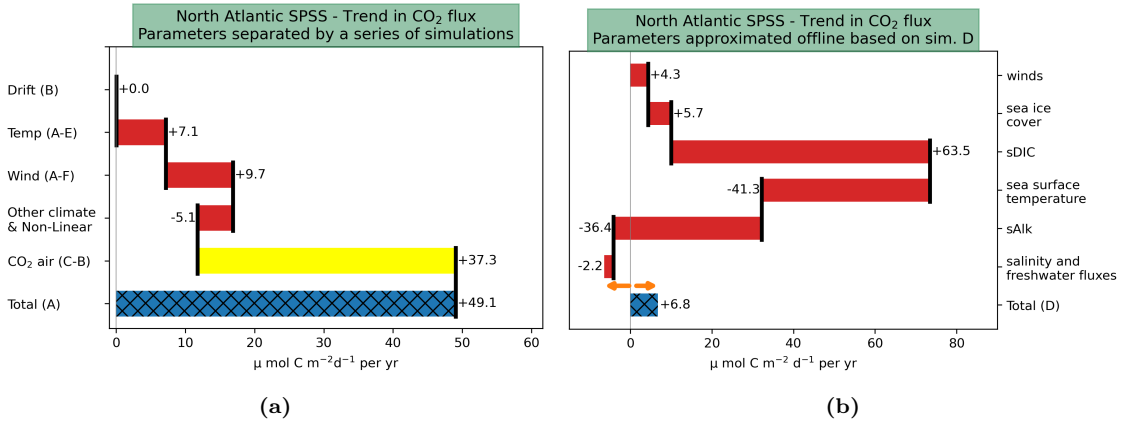

Figure S25: As in Figure S24, but for the North Atlantic SPSS.

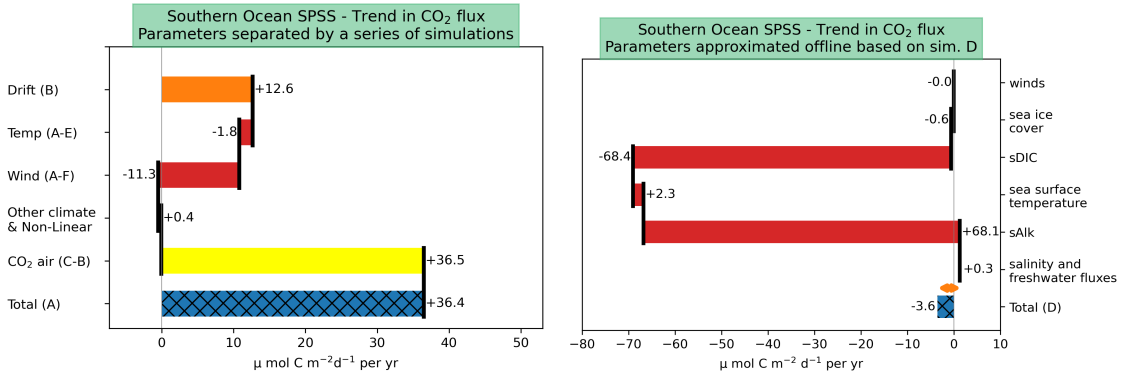

(a) **(b)**

Figure S26: As in Figure S24, but for the Southern Ocean SPSS.

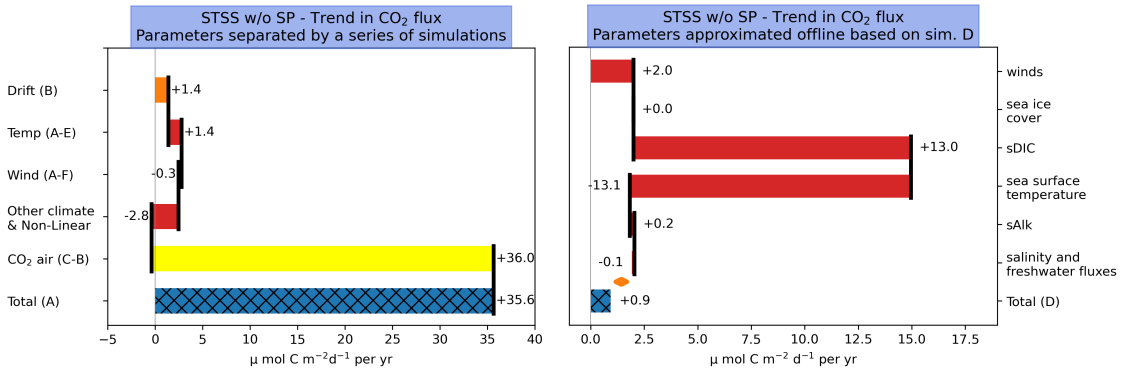

(a) **(b)**

Figure S27: As in Figure S24, but for the STSS without the South Pacific.

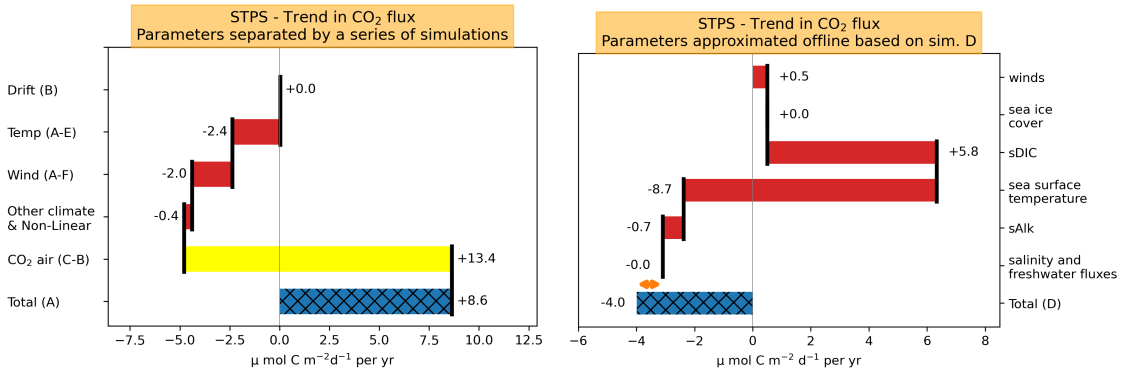

(a) **(b)**

Figure S28: As in Figure S24, but for the STPS biome.

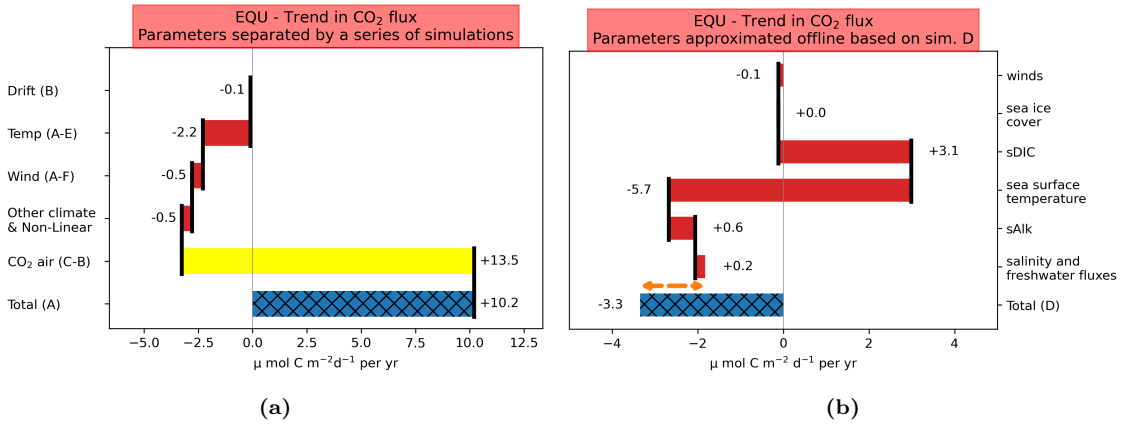

Figure S29: As in Figure S24, but for the EQU biome.

7.8 Offline analysis applied to the difference in sim-A, sim-E and sim-F

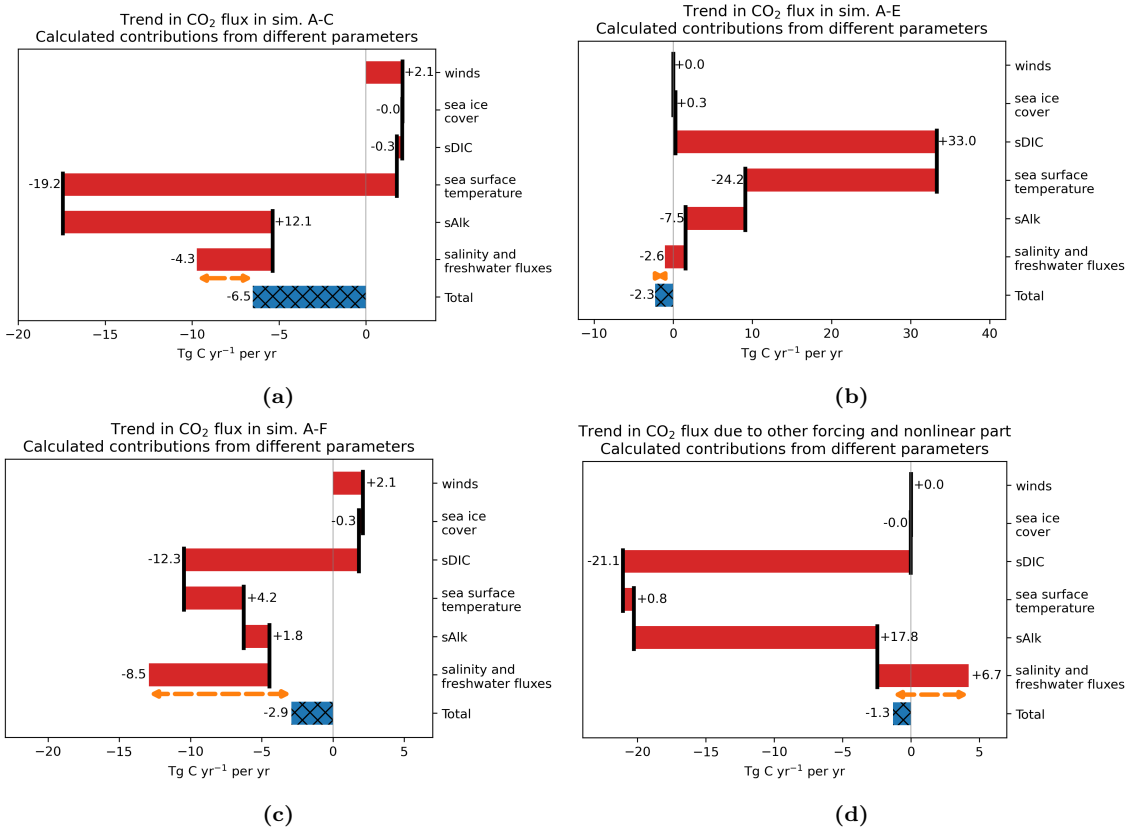

Figure S30: The impact of (a) the full climate variability, (b) the variability in the thermal forcing, (c) the variability in winds and (d) the other climate forcing together with the nonlinear effect is separated into the parameters via which the different types of model forcing affect the trend in the CO_2 flux. The contributions of each climate parameter to the trend in the globally integrated CO_2 flux, as they were calculated using the offline approach outlined in Section 3.2 are shown as red bars. They should ideally sum up to the total trend of CO_2 flux (blue-hashed bar at the bottom). The misfit is indicated by the orange double arrow.

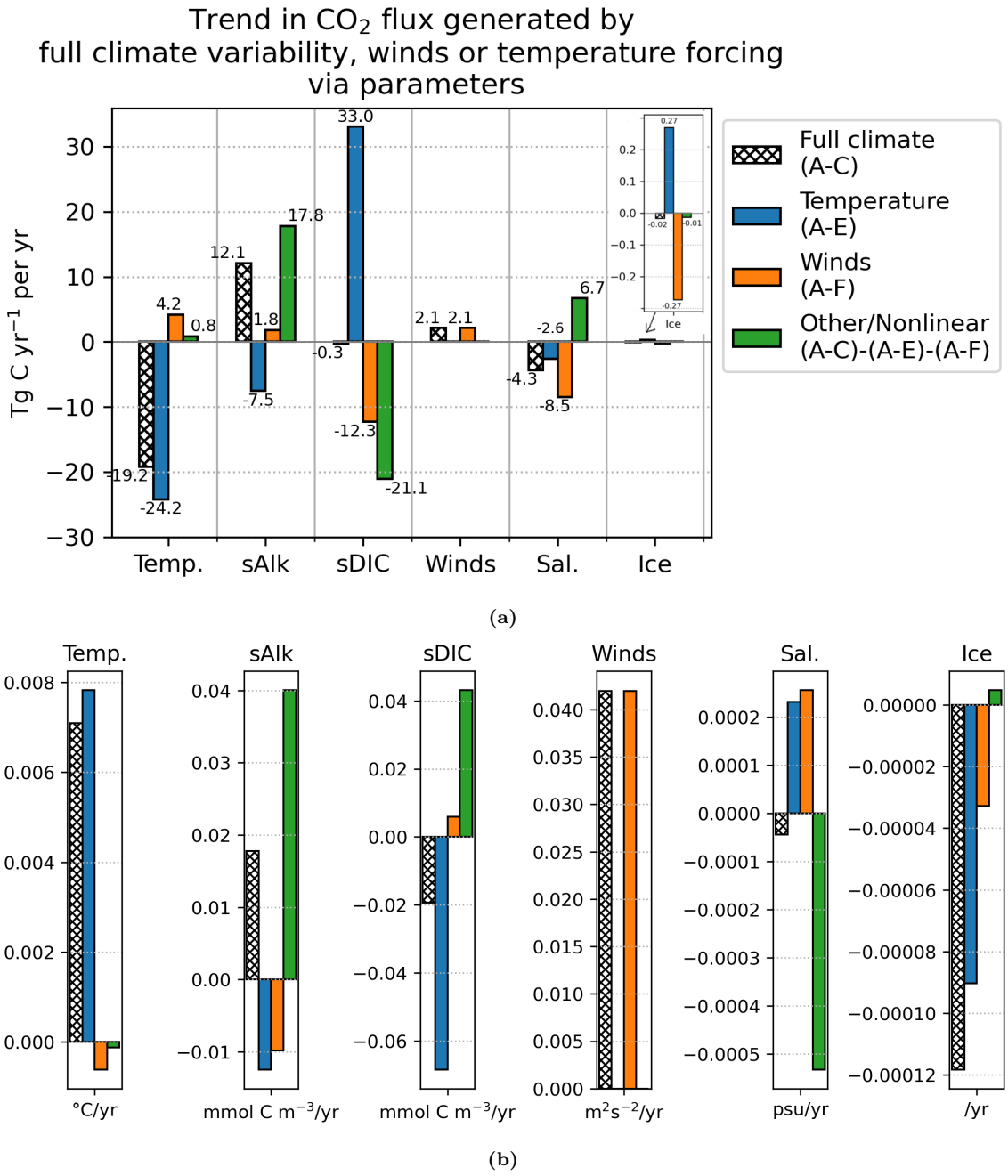

Figure S31: (a) The impact of the different types of model forcing on the trend in CO_2 flux via the variables through which the forcing affects the trend in the CO_2 flux. (b) The impact of the different types of model forcing on the trend in the variables.

Erklärung

Hiermit erkläre ich, dass ich die vorliegende Arbeit selbstständig und ohne fremde Hilfe angefertigt und keine anderen als die angegebenen Quellen und Hilfsmittel verwendet habe. Die eingereichte schriftliche Fassung der Arbeit entspricht der auf dem elektronischen Speichermedium.

Name der Datei: 1-ThesisMain.pdf

Weiterhin versichere ich, dass diese Arbeit noch nicht als Abschlussarbeit an anderer Stelle vorgelegen hat.

Frauke Bunsen, 03. August 2021